

STUDIES OF COLOR CHANGED BERYLS
CAUSED BY X-RAY IRRADIATION



A Thesis Submitted in Partial Fulfillment of the Requirements for the
Degree of Doctor of Philosophy in Chemistry
Suranaree University of Technology
Academic Year 2023

การศึกษาการเปลี่ยนสีของอัญมณีประเภทเบริลจากการฉายรังสีเอ็กซ์



นายวัชรกร เศษวงษ์

วิทยานิพนธ์นี้เป็นส่วนหนึ่งของการศึกษาตามหลักสูตรปริญญาวิทยาศาสตรดุษฎีบัณฑิต

สาขาวิชาเคมี

มหาวิทยาลัยเทคโนโลยีสุรนารี

ปีการศึกษา 2566

STUDIES OF COLOR CHANGED BERYLS CAUSED BY X-RAY IRRADIATION

Suranaree University of Technology has approved this thesis submitted in partial fulfillment of the requirements for the Degree of Doctor of Philosophy.

This Examining Committee

Natthapong Monarumit

(Asst. Prof. Dr. Natthapong Monarumit)

Chairperson

Piyanut Pinyou

(Asst. Prof. Dr. Piyanut Pinyou)

Member (Thesis Advisor)

Chatree Saiyasombat

(Dr. Chatree Saiyasombat)

Member (Thesis Co-Advisor)

Theeranun Siritanon

(Assoc. Prof. Dr. Theeranun Siritanon)

Member

Phimphaka Harding

(Assoc. Prof. Dr. Phimphaka Harding)

Member

Yupaporn Ruksakulpiwat

(Assoc. Prof. Dr. Yupaporn Ruksakulpiwat)

Vice Rector for Academic Affairs
and Quality Assurance

Santi Maensiri

(Prof. Dr. Santi Maensiri)

Dean of Institute of Science

วิทยากร เศษวงษ์ : การศึกษาการเปลี่ยนสีของอัญมณีประเภทเบริลจากการฉายรังสีเอ็กซ์
(STUDIES OF COLOR CHANGED BERYLS CAUSED BY X-RAY IRRADIATION)

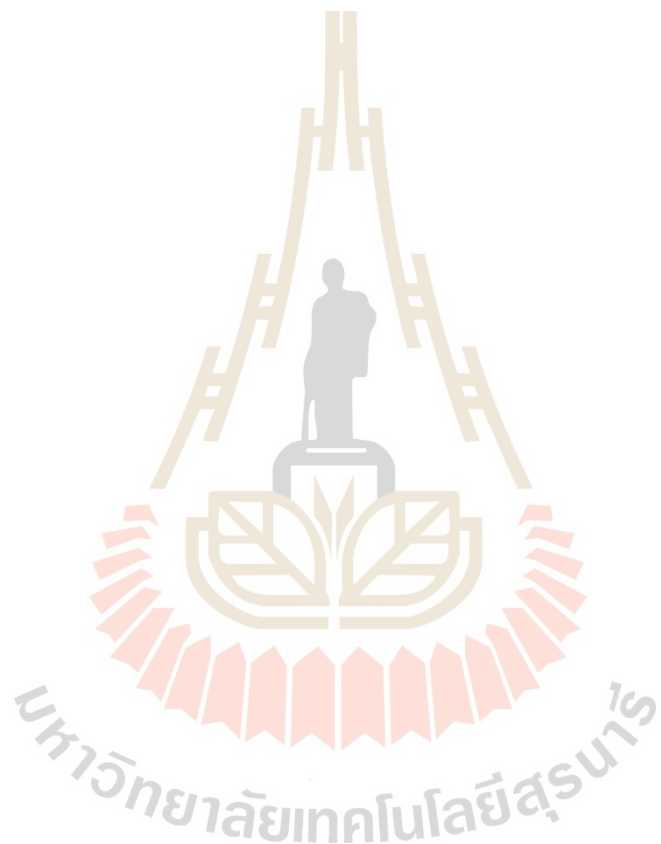
อาจารย์ที่ปรึกษา : ผู้ช่วยศาสตราจารย์ ดร.ปิยะนุช ปิ่นอยู่, 88 หน้า.

คำสำคัญ: เบริลเปลี่ยนสี/พฤติกรรมไอออนเหล็ก/สเปกโทรสโกปีการดูดกลืนรังสีเอ็กซ์

สีของอัญมณีประเภทเบริลเกิดจากหลายปัจจัยซึ่งรวมถึงส่วนประกอบทางธาตุ ความผิดปกติของอะตอม การเรียงตัวของแรมลทิน ความผิดปกติของโครงสร้าง และรูปแบบการเจริญเติบโตของผลึก โดยเฉพาะอย่างยิ่งไอออนของธาตุเหล็ก ซึ่งเป็นธาตุในหมู่โลหะทรานซิชันมีวาเลนซ์อิเล็กตรอนอยู่ในออร์บิทัล d ที่มีช่องว่างแถบพลังงานสูง มีความไวต่อการเกิดออกซิเดชัน และชอบสร้างพันธะกับธาตุออกซิเจน

การศึกษานี้เปรียบเทียบสีเบริลธรรมชาติและเบริลสังเคราะห์ (6 ตัวอย่าง) โดยตัวอย่างเบริลสังเคราะห์มีปริมาณไอออนเหล็กสูงกว่าเบริลธรรมชาติ หลังตัวอย่างผ่านการฉายรังสีเอ็กซ์จากเครื่องกำเนิดแสงซินโครตรอน เบริลส่วนใหญ่เปลี่ยนสีโดยมีสีเหลืองเข้มขึ้น ยกเว้นเบริลไม่มีสีที่ไม่ได้แสดงการเปลี่ยนแปลง การวิเคราะห์สเปกตรัมการดูดกลืนแสงย่านอัลตราไวโอเลตถึงวิสิเบิลและสเปกตรัมการดูดกลืนแสงย่านเอกซเรย์ช่วง XANES แสดงลักษณะเด่นชัดที่เชื่อมโยงกับไอออนเหล็กประจุบวกสองและประจุบวกสาม หลังผ่านการฉายรังสีเอ็กซ์พบว่าสเปกตรัมแสดงการเปลี่ยนแปลงสภาพของไอออนเหล็กเป็นประจุบวกสามเพิ่มขึ้น ซึ่งสามารถยืนยันผลได้ด้วยเทคนิคการดูดกลืนแสงและเทคนิคการสั่นพ้องทางแม่เหล็กของอิเล็กตรอน การวิเคราะห์สเปกตรัมการดูดกลืนแสงย่านเอกซเรย์ช่วง EXAFS พบว่าไอออนเหล็กมีลักษณะเรียงตัวอยู่ในโครงสร้างที่มีหกอะตอมล้อมรอบ และมีโอกาสที่จะแทนที่ที่ตำแหน่งออคติเนียมมากกว่าที่อยู่ในตำแหน่ง 6g หลังผ่านการฉายรังสีเอ็กซ์พบว่าความยาวพันธะของโครงสร้างไม่มีการเปลี่ยนแปลง แต่ปริมาณไอออนเหล็กเป็นประจุบวกสามเพิ่มขึ้นที่ตำแหน่งเดิมภายในโครงสร้าง ซึ่งแสดงให้เห็นถึงปฏิกิริยาการถ่ายโอนประจุระหว่างไอออนเหล็กประจุบวกสองและบวกสาม จากการถ่ายโอนประจุระหว่างไอออนเหล็กที่มีออกซิเดชันต่างกันทำให้เกิดสีน้ำเงินในเบริลที่ระยะห่างที่เป็นไปได้ประมาณ 2.49-2.51 อังสตรอม การเปลี่ยนสีของตัวอย่างเบริลเกิดจากการลดลงของการถ่ายโอนอิเล็กตรอนระหว่างไอออนเหล็กที่มีสถานะการออกซิเดชันที่แตกต่างกันและการเพิ่มขึ้นของการถ่ายโอนอิเล็กตรอนระหว่างไอออนเหล็กที่มีสถานะการออกซิเดชันเดียวกันหรือระหว่างไอออนเหล็กกับออกซิเจน และจากการศึกษาสเปกตรัมการดูดกลืนแสงย่านเนียร์อินฟราเรดไม่พบข้อมูลที่ชี้ชัดในกรณีของสารปนเปื้อนและโมเลกุลน้ำที่แสดงการเปลี่ยนแปลงหรือการแตกตัวของพันธะระหว่างออกซิเจนกับไฮโดรเจนมากพอที่จะส่งผลต่อการเปลี่ยนแปลงค่าออกซิเดชันของไอออนเหล็ก

การปรับปรุงคุณภาพเบรลล์ด้วยการฉายรังสีเอ็กซ์พบได้น้อยกว่าเมื่อเทียบกับวิธีการอื่น ๆ ซึ่ง การศึกษานี้แสดงให้เห็นว่าการฉายรังสีเอ็กซ์จากเครื่องกำเนิดแสงซินโครตรอนสามารถสร้างโทนสี เหลืองที่เสถียรในเบรลล์ได้อย่างปลอดภัยและไม่มีกัมมันตภาพรังสีตกค้าง นอกจากนี้ความยืดหยุ่นใน การปรับขนาดของลำแสงและระยะเวลาการฉายรังสีเอ็กซ์สามารถนำไปสู่การสร้างอัญมณีเบรลล์ที่มี สองหรือสามเฉดสีได้ในอัญมณีหนึ่งชิ้น



สาขาวิชาเคมี
ปีการศึกษา 2566

ลายมือชื่อนักศึกษา Watanasakon setwong
ลายมือชื่ออาจารย์ที่ปรึกษา Piyanut Pinyou
ลายมือชื่ออาจารย์ที่ปรึกษาร่วม [Signature]

WATCHARAKON SETWONG : STUDIES OF COLOR CHANGED BERYLS CAUSED BY X-RAY IRRADIATION. THESIS ADVISOR : ASST. PROF. PIYANUT PINYOU, Ph.D. 88 PP.

Keyword: Beryl coloration/Iron ions behavior/X-ray absorption spectroscopy

Beryl gemstone colors result from several factors, including its elemental composition, atomic imperfections, mineral inclusions, structural irregularities, and crystal growth patterns. Notably, iron ions play a pivotal role due to their behavior as d-orbital transition metals, high energy band gap, vulnerability to oxidation, and affinity for bonding with oxygen.

This study compared various colors of natural and synthetic beryl samples (consisting of 6 beryl samples), with the synthetic variant containing a higher iron content. When subjected to X-ray synchrotron irradiation, the beryl underwent color changes, shifting towards an intense yellow hue, except for colorless beryl, which remained unaffected. The analysis encompassed UV-Vis and XANES spectra, which exhibited distinctive peaks linked to the electron transitions of Fe^{3+} and Fe^{2+} . The X-ray irradiation modified the oxidation state of iron ions, leading to an increase in Fe^{3+} as confirmed by absorption and EPR techniques. The EXAFS analysis revealed that Fe ions mostly had a six-coordinated arrangement and were more likely to replace Al sites than 6g sites. After X-ray irradiation, this substitution caused no change in bond lengths but an increase in Fe^{3+} ions in their original positions, indicating an inter-valence charge transfer (IVCT) reaction between Fe^{2+} and Fe^{3+} . This IVCT caused a blue color in the beryl and suggested a potential Fe-Fe pair distance of 2.49-2.51 Å (Lin *et al.*, 2013). This color shift resulted from reduced electron transfer between ions of different oxidation states and increased transfer between ions of the same oxidation state or between iron ions and oxygen. The NIR data from the study showed no evidence of foreign substances or water molecules, ruling out OH bond breakdown as the cause of observed oxidation effects.

While irradiation treatment has been less common for enhancing beryl compared to other methods, this study demonstrated that X-ray synchrotron irradiation could safely produce color-stable yellow tones in beryl without residual radioactivity.

Moreover, the ability to adjust the incident X-ray beam size and duration could create various two- or three-color shades in beryl gemstones.



School of Chemistry
Academic Year 2023

Student's Signature Watcharakon Setwong.
Advisor's Signature Piyanut Pinyou
Co-Advisor's Signature [Signature]

ACKNOWLEDGEMENTS

To begin, I wish to convey my deepest gratitude to my primary advisor, Assistant Professor Dr. Piyanut Pinyou, and my co-advisor, Dr. Chatree Saiyasombat, for their exceptional patience, motivation, inspiration, wise counsel, expert supervision, and continuous guidance from the early stages of this research, which greatly contributed to the excellence of this work.

I would also like to extend my thanks to Dr. Prael Jirawatkul for the valuable guidance provided throughout this project, as well as Dr. Suttipong Wannapaiboon and his team for providing me with valuable experiences at Beamline 1.1W MXT and their insights into XAS analysis. Dr. Catleya Rojviriyaya's support in gaining experience at Beamline 1.2W MTX is also appreciated, along with Dr. Phakkhananan Pakawanit and Ms. Chalermluck Poovasawat's guidance on utilizing white beam experimentation techniques.

Recognition is also due to the Synchrotron Light Research Institute (SLRI), a public organization in Thailand, and Suranaree University of Technology for their generous scholarships and partial support for this research. I'm also grateful to Dr. Nirawat Thammajak for his invitation and encouragement to pursue studies in the School of Chemistry, which included scholarships for study, research, and salary.

Lastly, I want to express my heartfelt appreciation to my family for their unwavering support and encouragement throughout my academic journey.

Watcharakon Setwong

CONTENTS

	Page
ABSTRACT IN THAI.....	I
ABSTRACT IN ENGLISH.....	III
ACKNOWLEDGEMENT.....	V
CONTENTS.....	VI
LIST OF TABLES.....	VIII
LIST OF FIGURES.....	X
LIST OF ABBREVIATIONS.....	XIV
CHAPTER	
I INTRODUCTION.....	1
II LITERATURE REVIEWS.....	4
2.1 Beryl gemstone.....	4
2.1.1 Beryl structure and origin.....	4
2.1.2 Beryl colors and theory.....	6
2.1.3 Synthetic beryl.....	8
2.2 The color treatment of beryl.....	9
2.2.1 Heat treatment.....	9
2.2.2 Irradiation and implantation treatment.....	11
2.3 Synchrotron X-ray energy.....	17
2.3.1 X-rays produced by Siam Synchrotron Light Research Institute.....	17
2.3.2 X-ray white beam energy radiation of SLRI.....	18
2.3.3 Application of X-ray synchrotron.....	20
III MATERIALS AND METHODS.....	21
3.1 Experimental procedure.....	21
3.2 Sample materials and sample preparation.....	21
3.3 Experimental setup.....	23

CONTENTS (Continued)

	Page
3.4 Characterization techniques.....	24
3.4.1 Electron Probe Micro Analyzer.....	24
3.4.2 Coloration Measurement.....	24
3.4.3 Ultraviolet Visible and Near Infrared Spectroscopy.....	25
3.4.4 X-ray Diffraction	25
3.4.5 X-ray Absorption Spectroscopy.....	27
3.4.6 Electron Paramagnetic Resonance.....	30
IV RESULTS AND DISCUSSION.....	31
4.1 Chemical composition and formular calculation.....	31
4.2 X-ray Diffraction of beryl structure	33
4.3 Beryl coloration and absorbance spectra.....	36
4.3.1 Beryl coloration.....	36
4.3.2 UV-Vis and NIR absorbance spectra.....	39
4.4 Absorption energy, oxidation state, and coordination number.....	46
4.4.1 X-ray Absorption Near Edge Spectrometer.....	46
4.4.2 Pre-edge feature and centroids position.....	48
4.4.3 Electron Paramagnetic Resonance.....	51
4.4.4 Extended X-ray Absorption Fine Structure.....	54
4.5 Polarization of beryl crystal to X-ray and UV-vis absorption.....	62
4.5.1 X-ray Diffraction of crystal plane conformation.....	62
4.5.2 UV-Vis-NIR absorption spectra for beryl crystal comparison.....	63
4.5.3 Comparison of beryl crystal using X-ray Absorption Spectroscopy...	65
V CONCLUSION.....	67
REFERENCES.....	70
APPENDIX.....	81
CURRICULUM VITAE.....	88

LIST OF TABLES

Table	Page
2.1 Theory of beryl colors were reported in “An update on color in gem” (Fritsch & Rossman, 1988).....	7
4.1 The average chemical composition of beryl samples as determined by EPMA.....	32
4.2 Unit-cell parameters of the beryls in this study and their assignment to a substitution series following Aurisicchio <i>et al.</i> (1988) in comparison to beryls from Western Carpathian.....	35
4.3 The CIELab values of beryl samples as determined using a D65 2° illuminant and a reference angle.....	37
4.4 The CIELab values of natural and synthetic beryls as determined using a D65 2° illuminant and a reference angle.....	37
4.5 The electron transition and band energy of iron ions.....	43
4.6 XANES pre-edge fitting results of beryl powder samples.....	49
4.7 Local environments of Fe from R space EXAFS fitting of Fe ₂ O ₃ standard.....	55
4.8 The first scattering path of oxygen nearest to Fe ions in beryl structure was fitted using Model-I of EXAFS R-space.....	58
4.9 Model-I and Model-II R space fits of the Fe K-edge generated local environments of Fe in beryl samples.....	60
A.1 Model-I and Model-II were used to fit the first scattering path of neighboring atoms nearest to Fe ions in the BL1 sample.....	82
A.2 Model-I and Model-II were used to fit the first scattering path of neighboring atoms nearest to Fe ions in the BL2 sample.....	83
A.3 Model-I and Model-II were used to fit the first scattering path of neighboring atoms nearest to Fe ions in the BL3 sample.....	84
A.4 Model-I and Model-II were used to fit the first scattering path of neighboring atoms nearest to Fe ions in the BL4 sample.....	85

LIST OF TABLES (Continued)

Table	Page
A.5 Model-I and Model-II were used to fit the first scattering path of neighboring atoms nearest to Fe ions in the BL5 sample.....	86
A.6 Model-I and Model-II were used to fit the first scattering path of neighboring atoms nearest to Fe ions in the BL6 sample.....	87



LIST OF FIGURES

Figure		Page
2.1	<p>Crystal structure of beryl ($\text{Be}_3\text{Al}_2\text{Si}_6\text{O}_{18}$): (a) projected on the basal plane (0001). The green, light blue, blue, and red colors represent the Be, Al, Si, and O atoms, respectively. The unit cell is denoted by the black line. The dashed line describes the octahedral site which can be occupied by Fe^{3+}, Cr^{3+}, and V^{3+}. Ring channel on channel site, which is shown by the yellow square, can be occupied by water (H_2O), Na^+, K^+, Cs^+ and Fe^{2+}. Solid line represents octahedral site and dotted line represent 6g site (b).....</p>	5
2.2	<p>Greenish blue (A), greenish yellow (B), yellow green (C), and orangish-pink (D) Madagascar samples before and after heat treatment in the electric furnace under reducing atmospheres at 400°C (Chankhantha and Thanasuthipitak., 2012). Aquamarine beryl (E) and yellow beryl (F) samples from Vietnam before and after heat treatment in the muffle-furnace under air atmospheres for 12 hours at heating rates of 300, 500, 700, 900, and $1,100^\circ\text{C}$ (Fridrichová <i>et al.</i>, 2015).....</p>	10
2.3	<p>Three rough aquamarine samples from the same source, before ancement (left), implanted with nitrogen ions (middle), and heated at 400°C under reducing atmosphere (right). (Luangpakdee <i>et al.</i>, 2016).....</p>	14
2.4	<p>Experimental setup for electrodiffusion; (A) sample holder: anode (1), graphite pellet (2), salt with the contaminant ion (3), aquamarine sample (4), graphite sample (5), cathode (6). (B) experimental setup of temperature controlled electrodiffusion: a) nitrogen flow controller, b) cylindrical oven, c) sample holder, d) voltage source, and e) oven controller (B). (Alkmim <i>et al.</i>, 2017).....</p>	15

LIST OF FIGURES (Continued)

Figure	Page
2.5 Alkalis and water representation in the channels of beryl lattice: a) beryl channel with Na ⁺ ion at position 2a interacting with type I H ₂ O molecule, and Na ⁺ ion at position 2b interacting with type II H ₂ O molecule; b) Na ⁺ at position 2a seen from above the plane perpendicular to the c-axis (001). (Anderson, 2006).....	17
2.6 SPS comparison of spectra from different sources. (BM = bending magnet, SWLS = superconducting wavelength shifter, MPW = multipole wiggler, and U60 = SPS Halbach-type planar undulator).....	19
2.7 The sample position of BL 1.2 W with the partial flow measured as a function of the energy present.....	19
3.1 The six groups of beryl samples used in this project, classified based on their hue and origin: BL1, BL2, BL3, BL4, BL5, and BL6 (synthetic).....	22
3.2 Irradiation of samples with white beam X-rays from 2.4 Tesla MPW permanent magnet SLRI sources.....	23
3.3 The CIE 1976 L*a*b* color space is depicted in 3D and 2D diagrams.....	25
3.4 Schematic of the Debye-Scherrer diffractometer.....	26
3.5 XAS Illustration: (a) X-ray absorption in an atom, (b) synchrotron XAS technique setup, (c-d) XAS spectrum and electron transfer energy state after atom absorption.....	28
3.6 Sample orientations with prismatic plane (plane A) and basal plane (plane C) facing incoming X-ray (edit from Bunnag <i>et al.</i> , 2020).....	29
4.1 The initial powder beryl (solid line) and irradiation powder beryl (dote line) X-ray diffractograms reveal the 2θ between 10-60 (a) and magnification 2θ between 27-32 (b).....	34
4.2 a) and (b) show 3D and 2D diagrams of the CIE 1976 L*a*b* color space; (c) The b* value of beryl coloration as a consequence of X-ray irradiation time.....	38
4.3 The absorbance spectrum of beryl crystal sample.....	40

LIST OF FIGURES (Continued)

Figure	Page
4.4 Tauc plot for direct bandgap of beryl crystal sample, with black solid-line representing initial beryls and red solid line representing IRR beryls. The bandgap is defined as the intercept of the dotted line with the horizontal axis.....	44
4.5 XANES spectra of irradiated beryl powder samples (0, 0.5, 1, 4, 10 mins) compared to Fe ²⁺ /Fe ³⁺ mixture ratios of 0, 10, 25, 50, 75, 90, and 100 wt.% Fe ³⁺	46
4.6 Background subtracted pre-edge peaks of the beryl sample (dotted lines) along with the Gaussian component used in the fitting procedures (dash lines and short dotted lines) and Gaussian sums (solid lines).....	48
4.7 Relationship between integrated pre-edge intensity and pre-edge centroid energy locations of beryl samples and oxide standards. The open circles relate to the reference research, which gave typical characteristics for four kinds of Fe species in Wilke <i>et al.</i> (2001) and Giuli <i>et al.</i> (2011). [4] represents a 4-fold coordinated Fe and [6] represents a 6-fold coordinated Fe.....	50
4.8 1 st functional derivative EPR spectra of beryl powder, (a) comparison of signal intensities, (b)-(g) comparison of EPR feature in normalized intensity....	52
4.9 Chemical structure and single scattering path of the Fe ₂ O ₃ model (a), Fourier transforms of k ² ·χ(k) spectra and R-space curve and fits for Fe K-edge EXAFS spectra from the Fe ₂ O ₃ experiment (b).....	55
4.10 Chemical structure and single scattering path of Model-I (a), Model-II (b).....	56
4.11 The Fe K-edge EXAFS spectra of beryl powder samples calculation using theoretical standards from IFEFFIT using the ARTEMIS software and comparison of initial and after X-ray irradiation spectra in Fourier transforms R-spec (a and b) and k ² ·χ(k) of k-space (c).....	57

LIST OF FIGURES (Continued)

Figure	Page
4.12 The IFEFFIT calculation and comparison of beryl experiment spectra and Models I and II simulation spectra in R-space curve and fits for (a), Fourier transforms $k^2 \cdot \chi(k)$ of k-space (b) for determining the local structure of the Fe K-edge EXAFS spectra of beryl powder sample.....	59
4.13 The comparative bond length of beryl sample before and after X-ray irradiation by scattering path fitting (a) bond length of Model-I fitting and (b) bond length of Model-II fitting.....	61
4.14 X-ray diffractogram basal plane (dotted line) and prismatic plane (solid-line) of crystal beryl sample BL2 and BL5.....	63
4.15 UV-Vis-NIR absorbance spectra of beryl crystal sample.....	64
4.16 XANES spectra of crystal sample for each plane polarization direction.....	65
A.1 Models I and II's IFEFFIT calculations are compared to experiment spectra of BL1-Initial (a) and BL1-IRR (b).....	82
A.2 Models I and II's IFEFFIT calculations are compared to experiment spectra of BL2-Initial (a) and BL2-IRR (b).....	83
A.3 Models I and II's IFEFFIT calculations are compared to experiment spectra of BL3-Initial (a) and BL3-IRR (b).....	84
A.4 Models I and II's IFEFFIT calculations are compared to experiment spectra of BL4-Initial (a) and BL4-IRR (b).....	85
A.5 Models I and II's IFEFFIT calculations are compared to experiment spectra of BL5-Initial (a) and BL5-IRR (b).....	86
A.6 Models I and II's IFEFFIT calculations are compared to experiment spectra of BL6-Initial (a) and BL6-IRR (b).....	87

LIST OF ABBREVIATIONS

Å	=	Angstrom
°C	=	Degree Celsius
V	=	Voltage
eV	=	Electron volte
keV	=	Kiloelectron volts
MeV	=	Megaelectron volts
nA	=	Nanoampere
mm	=	Millimeter
µm	=	Micromillimeter
Kα	=	K-alpha X-ray fluorescence
λ	=	Lambda (wavelength)
Gy	=	Gray (ionizing radiation); 1 Gy = 1 Joule/kilogram = 100 rad
kGy	=	kilo gray
ion/cm ²	=	Ion dose density
E ₀	=	Edge absorption energy of element
cm ⁻¹	=	A reciprocal centimeter (or wavenumber)
H x V	=	Horizontal x Vertical (area)
wt. %	=	percent by weight
c/a	=	Lattice parameter ratio
VCT	=	Valence charge transfer
IVCT	=	Intervalence charge transfer
O _h	=	Octahedral symmetry
T _d	=	Tetrahedral symmetry
CN	=	Coordination number
σ ²	=	Mean-square disorder of neighbor distance
R	=	Distance to neighboring atom
R-factor	=	residual factor

LIST OF ABBREVIATIONS (Continued)

V_o	=	oxygen vacancies defects
DFT	=	density functional theory
IFEFFIT	=	Interactive Fitting Interface and Environment for Data Analysis of X-ray Absorption Fine Structure
Est.	=	Estimate
SD	=	Standard derivative
PAE	=	Plane-parallel to <i>c</i> -axis
PEE	=	Plane-perpendicular to <i>c</i> -axis
TL	=	Thermoluminescence
ESR	=	Electron spin resonance
EPR	=	Electron paramagnetic resonance
OA	=	Optical absorption
UV-Vis	=	Ultraviolet to Visible light
FTIR	=	Fourier Transform Infrared Spectrometer
NIR	=	Near infrared region
XRD	=	X-ray Diffraction
XAS	=	X-ray absorption spectroscopy
XANES	=	X-ray absorption near-edge structure
EXAFS	=	X-ray absorption fine structure
EPMA	=	Electron Probe Micro Analyzer
SLRI	=	Synchrotron Light Research Institute
SPS	=	Siam Photon Source
MPW	=	Multipole Wiggler
BM	=	Bending magnet
SWLS	=	Superconducting wavelength shifter
U60	=	SPS Halbach-type planar undulator
BL1.1W MXT	=	Beamline 1.1 Wiggler, Multiple X-ray techniques
BL1.2W XTM.	=	Beamline 1.2 Wiggler, X-ray Imaging & X-ray Tomographic Microscopy

CHAPTER I

INTRODUCTION

Beryl ($\text{Be}_3\text{Al}_2\text{Si}_6\text{O}_{18}$) has a hexagonal crystal structure in the $P6/mcc$ space group. The structure of beryl is composed of layers of cyclic silicates Si_6O_{18} linked to AlO_6 octahedra and BeO_4 tetrahedra. Layers of cyclic silicates form hollow channels parallel to the C axis that are typically filled with water (type I H_2O and type II H_2O), carbon dioxide, or alkali ions (Deer *et al.*, 1997). Cations can also be found in 6-fold (6g) coordinated interstitial sites positioned between two octahedral sites along the C axis. Natural beryl gemstones come in a variety of colors, including goshenite (colorless), emerald (green), aquamarine (blue green), morganite (rose pink), bixbite (dark red), and heliodor (yellow gold). A natural gemstone is available in a variety of colors with distinctive inclusions from its natural origin, and it can influence people who interact with it. Despite being from a high-priced gemstone source, a gemstone with unclear colors and inclusions is considered to be less valuable. Therefore, gemstones are often subjected to color treatment methods to increase their aesthetic value. In comparison to heat treatment, radiation treatment of gemstones is a relatively new technique. Radiation has been used to treat and improve the color of precious and semi-precious stones on the Mohs scale, such as diamonds, beryl, pearls, topaz, yellow sapphire, amethyst, and tourmaline. Yellow beryl was subjected to gamma and electron beam irradiation, which resulted in intense yellow coloration and the formation of Fe ions (Nassau, 1974; Ittipongse *et al.*, 2017).

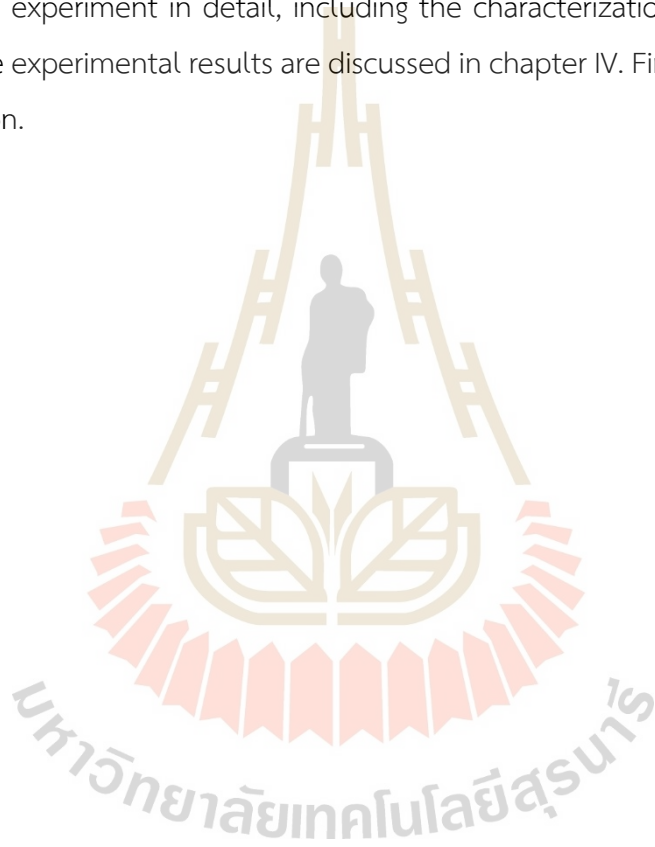
Irradiation is the process of causing electronic interaction within atoms or local material structures by using electromagnetic radiation. Other methods of irradiation include electron beam, neutron, and gamma ray irradiation. Cobalt-60 and Radium-226 are usually used as gamma ray sources. However, the gamma ray and neutron irradiation processes produce residual radioactive materials in the gemstone, which are hazardous to human health (Ibragimova *et al.*, 2009; Zagoritis, 2022).

Synchrotron X-ray radiation is frequently employed in structure-based investigations to analyze the coordination environments and oxidation states of atoms. An intense high-power X-ray beam can cause color changes in gemstones (Pough and Rogers, 1947). Secondary electrons emitted by a sample can potentially damage and change the color of organic and biological species. The duration of exposure to the incident X-ray beam, the X-ray beam flux, and the chemical properties of the gemstone can all have an impact on the phenomenon. White beam X-ray energy from the Synchrotron Light Research Institute (SLRI) was used to investigate the transformation of natural pearl colors to iridescent gold and the imprinting of gold patterns onto pearls. To increase the range of energy and X-ray flux beamline, a 2.4 Tesla Multipole Wiggler (MPW) permanent magnet was installed in the 1.2W X-ray Imaging & X-ray Tomographic Microscopy (XTM). The polychromatic X-ray beam of the MPW was optimized using white-beam slits and a toroidal focusing mirror (FM). Low energy X-rays (4 keV) were filtered by the beryllium window (Be window), which allowed high energy X-rays (5-20 keV) to enter the X-ray imaging and microtomography experiments. These defined the X-ray beam up to 8x4 mm (HxV) at the sample position. A white-beam X-ray responds to detailed material-related questions and can be used to investigate the atomic structure of various elements after the irradiation process, which has a faint residual radioactive aftereffect.

In this project, beryl gemstone was irradiated with an X-ray white beam at BL1.2W (SLRI). Beryl samples from South Africa were chosen based on their natural color classification, which included colorless, light blue, blue, yellowish blue, and yellow, as well as a synthetic deep blue beryl. Before and after X-ray irradiation, each color sample was divided into two types: crystal samples for observing color change and powder samples for investigating the reaction mechanism. To understand the physical and chemical properties of beryl samples before and after irradiation, five experimental techniques were used. The total amount of essential elements was determined using the Electron Probe Micro Analyzer (EPMA). The crystalline structure, which may have been affected by the irradiation, was examined using X-ray Diffraction (XRD). The atomic local structure, oxidation states, symmetry surrounding, and neighboring environments such as coordination numbers and bond distances were investigated

using X-ray absorption spectroscopy (XAS). Electron paramagnetic resonance (EPR) was used to investigate the paramagnetic properties, unpaired electrons, and free radicals. UV-Vis spectroscopy with reflection probe and near infrared (NIR) spectroscopy were used to monitor the color changes of beryl crystals and water molecules, respectively.

This thesis is divided into five chapters. This chapter contains the introduction and significance of the study. Chapter II discusses beryl gemstone and X-ray synchrotron properties, origin of beryl color, and color improvement. Chapter III describes the experiment in detail, including the characterization techniques used in this work. The experimental results are discussed in chapter IV. Finally, chapter V states the conclusion.



CHAPTER II

LITERATURE REVIEWS

This chapter gives a brief review of the properties of beryl, an application and the basic principle and physics of X-ray synchrotron.

2.1 Beryl gemstone

2.1.1 Beryl structure and origin

Natural beryl is a mineral composed of beryllium aluminium cyclosilicate, with the chemical formula $\text{Be}_3\text{Al}_2(\text{SiO}_3)_6$. Beryl crystallizes in a hexagonal space group $P6/mcc$ (Yakubovich *et al.*, 2009). The beryl structure is composed of six-fold Si_6O_{18} rings, which consist of SiO_4 tetrahedra connected to each other by BeO_4 tetrahedra and AlO_6 octahedra. A prominent hollow channel parallel to the optical c-axis runs through the centers of the six-fold silicate rings as shown in Figure 2.1. These can accommodate many molecules like water (type I H_2O and type II H_2O), carbon dioxide, heavy alkali metals such as Cs (Deer *et al.*, 1997) as well as an isomorphic substitution at the Al, Si, and Be sites. Pure beryl is water-clear and colorless, whereas different transition metal ions like Fe, Cr, Mn, and V can cause different colors to be observed when substituting for Al and in some cases, Be (Eeckhout, Neisius, and Castañeda, 2005). The accommodation in the channels, such as the substitution of different metal ions in these sites, has been discussed and is more contentious.

Beryl is a hexagonal crystalline material with conchoidal fracture. The size of the crystal can range from very small to several meters wide. This mineral has a hardness of 7.5-8 and a specific gravity of 2.63-2.80 (density relative to pure water). Beryllium is a very rare metal, and beryl gemstone is a mineral that contains a high concentration of beryllium. Hence, beryl mineral only occurs in a few geological formations where there is enough beryllium element.

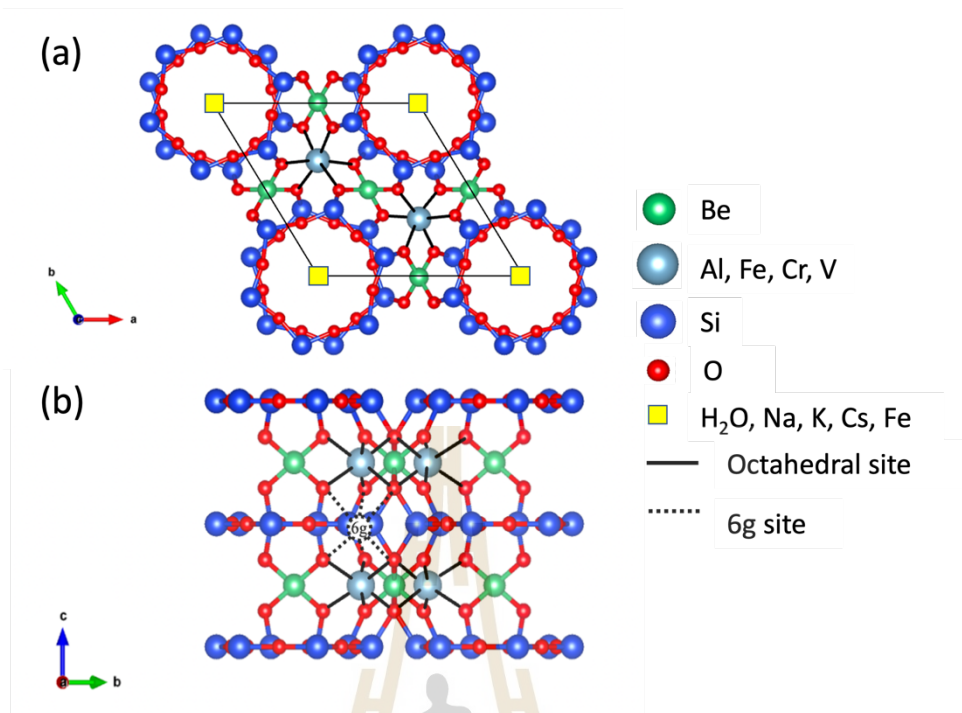


Figure 2.1 Crystal structure of beryl ($\text{Be}_3\text{Al}_2\text{Si}_6\text{O}_{18}$): (a) projected on the basal plane (0001). The green, light blue, blue, and red colors represent the Be, Al, Si, and O atoms, respectively. The unit cell is denoted by the black line. The dashed line describes the octahedral site which can be occupied by Fe^{3+} , Cr^{3+} , and V^{3+} . Ring channel on channel site, which is shown by the yellow square, can be occupied by water (H_2O), Na^+ , K^+ , Cs^+ , and Fe^{2+} . Solid line represents octahedral site and dotted line represent 6g site (b).

Beryl is most usually found in igneous rocks like granite, rhyolite, and granite pegmatite; but, in the Ural Mountains in Russia, it can be found in metamorphic rocks like pegmatite, and in igneous rocks in veins and cavities where hydrothermal activity has altered granitic rocks. In New England, pegmatite has yielded some of the world's largest beryls, including a beryl crystal that measured 18 feet by 4 feet and weighed close to 40,000 pounds. In addition, scientists discovered the world's largest beryl crystal in Madagascar, which weighed 840,000 pounds, and measured 59 feet in length, and 11 feet in diameter. The world's most renowned and remarkable emeralds, or green beryl, are found in Colombia, where they mostly occur in limestone. Asia,

Europe, South Africa, and the United States are other excellent destinations for locating beryl resources (King, 2020). The stunning gemstone has been spotted in a wide variety of nations, including India, Brazil, Canada, China, Italy, Pakistan, Russia, Ethiopia, Madagascar, Mozambique, Namibia, Nigeria, the United Kingdom, the United States, Mexico, and Vietnam (Sultana and Podila, 2018).

Only around one hundred minerals contain the element beryllium, therefore beryl is widely used in jewelry. Furthermore, wires made from beryllium metal are also utilized in space shuttles (Sultana and Podila, 2018). Cat's-eye gemstones are created from chatoyant beryl, which is then carved into a cabochon shape. Among the many types of beryl, emeralds and aquamarines are the most well-known for their exceptional beauty. However, the appeal of morganite from Brazil has skyrocketed since 2010 due to better heat treatment techniques, which improved the color of the material with weak saturation. When the financial value of imported gemstones was compared to that of diamonds, emeralds came in second (King, 2020).

2.1.2 Beryl colors and theory

While there are different varieties of beryl, they are all the same mineral. Colorless to white (goshenite), green (emerald), greenish blue to pure blue (aquamarine), yellow-green to golden-yellow (heliodor), rose to pink (morganite), red variation (bixbite), and deep blue (maxixe) are all well-recognized varieties. Table 2.1 displays the atomic positions of the transition metals that replace Al^{3+} in the octahedral sites of beryl and the channel sites, which create their respective hues. Due to a charge transfer process, a yellow color emerged as a result of Fe^{3+} replacing Al^{3+} (Woods and Nassau, 1968; Deer *et al.*, 1997). The presence of Fe^{2+} at the aquamarine's channel site was the source of the mineral's characteristic blue color (Woods and Nassau, 1968; Adamo *et al.*, 2008). Intervalence charge transfer between Fe^{2+} and Fe^{3+} , on the other hand, caused intense blue color (Samoilovich *et al.*, 1971; Goldman *et al.*, 1978; Taran and Rossman, 2001). The color center was found to be a dark blue (Nassau, Prescott and Wood, 1976; Andersson, 1979). Pink beryl was formed when Mn^{2+} replaced Al^{3+} in the cation exchange complex (Woods and Nassau, 1968; Deer *et al.*, 1997). Red variations were caused by Mn^{3+} replacing Al^{3+} (Shigley and Foord, 1984;

Platonov *et al.*, 1978). V^{3+} replacing Al^{3+} was one cause of the green color (Wood & Nassau, 1968), while Cr^{3+} replacing Al^{3+} was another (Vogel, 1934). The colorless beryl is commonly assumed to be the result of lack of impurities, but Deer *et al.* (1997) reported that the absence of color was caused by Fe^{2+} replacing Al^{3+} .

Table 2.1 Theory of beryl colors were reported in “An update on color in gem” (Fritsch and Rossman, 1988).

Theory	Ions and coordination	Colors
Charge transfer	$O^{2-} \rightarrow Fe^{3+}$ at the octahedral position	Yellow to brown: heliodor (Wood and Nassau, 1968)
Intervalence charge transfer	$Fe^{2+} \rightarrow O^{2-} \rightarrow Fe^{3+}$ at the octahedral position	Blue: aquamarine (Samoilovich <i>et al.</i> , 1971; Goldman <i>et al.</i> , 1978)
Intervalence charge transfer, Change transfer	$Fe^{2+} \rightarrow O^{2-} \rightarrow Fe^{3+}$, $O^{2-} \rightarrow Fe^{3+}$	Greenish blue: aquamarine (Nassau, 1984)
Color center	CO_3 , NO_3 group due to irradiation	Deep blue: mixite (Nassau, Prescott, and Wood, 1976; Andersson, 1979)
Impurities	Fe^{2+} at the channel	Blue: aquamarine (Wood and Nassau, 1968)
Impurities	Mn^{3+} at the octahedral position	Dark red to red: bixbite (Shigley and Foord, 1984)
Impurities	Mn^{2+} at the octahedral position	Rose to pink: morganite (Woods and Nassau, 1968)
Impurities	V^{3+} at the octahedral position	Green: vanadium emerald (Woods and Nassau, 1968)
Impurities	Cr^{3+} at the octahedral position	Green: emerald (Vogel, 1934)

Scientists have been attempting to observe the color origin of beryl gemstones using various techniques for more than 50 years. Mossbauer Spectroscopy (MS), Optical Absorption (OA), and Electron paramagnetic Resonance (EPR) are popular techniques for studying coordination and ion type in beryl. The findings of ion and

coordination studies continue to be incongruent with the above three techniques for explaining the presence of iron ions in aluminum positions. The findings of ion and coordination studies on the presence of iron ions in aluminum positions in beryl with the above three techniques continue to be incongruent (Andersson, 2013). The color treatment of beryl, the detail of ions and coordination are presented in topic 2.2.

2.1.3 Synthetic beryl

Synthetic beryl can be produced using a variety of processes, including flux-fusion, hydrothermal operations, and gas transport reaction (Leone *et al.*, 2015). Hydrothermal growth processes have been used to commercially create synthetic beryl since the mid 1960s (Nassau, Prescott, and Wood, 1976). In 1964, the development of synthetic emerald using the flux technique entered the market with a new commercially viable gemstone (Koivula and Keller, 1985). Nowadays, synthetic gemstones that rival the beauty of natural gems are being developed. The chemical composition and physical properties of synthetic beryl are similar to the characteristics of natural beryl. Synthetic beryl jewelry is extremely popular because it is both beautiful and affordable to the majority of people. Many people prefer synthetic beryls because they have superior color, clarity, durability, and are much less expensive than natural gems. Although similar in appearance, synthetic beryl may contain distinguishing inclusions or have a refractive index that differs from natural beryl (Shigley *et al.*, 2001). With a microscope, synthetic beryl can often be distinguished from natural beryl by looking for signs of the hydrothermal growth process under reflected light and dark-field illumination at magnifications ranging from 10x to 40x. Chevron growth features are the most common and easiest to find evidence of synthetic growth. The hydrothermal crystals of synthetic beryl are grown at a condition of a solution at temperatures above 600°C and pressures above 2000 bars (Bukin *et al.*, 1986; Schmetzer, 1988; Demianets, 1996). Typically, thin (1 mm thick) seed plates of beryl synthetic initiate crystal growth. For the most part, the crystal faces are relatively flat. Surfaces parallel to the seed plate have the fastest growth rate and thus exhibit a variety of growth characteristics (mainly growth hillocks and some hopper formations).

2.2 The color treatment of beryl

Treatment is the process of altering the appearance, durability, value, or supply of a gemstone by means other than cutting and polishing. For centuries, gemstones have been enhanced and treated through different processes. Researchers have improved the appearance of lower-grade gems, and these treatments can sometimes completely transform a gemstone. Treatment methods include heat treatment, radiation, dyeing, and bleaching. The detection of these treatments can range from simple to nearly impossible. A treated gem is frequently encountered in the gem and jewelry trade and is always disclosed to the consumer, which is a standard practice in the trade. However, some sellers may unjustly attempt to misrepresent treated grade gemstones at high prices of natural grade. Heating and irradiation are the two most common methods of gemstone treatment (Zagoritis, 2022).

2.2.1 Heat treatment

Heat treatment is a gemstone enhancement process that is similar to the natural system under which minerals naturally occur. The gemstone is heated to very high temperatures during treatment, but not to the melting point of the gemstone. This alters the chemical mechanism of impurities, such as inclusions or removal due to thermal effects, and may cause an impurity to reform itself, resulting in a change in mineral species. As a result, the color and optical properties of the gemstone are altered. Because of these color changes, each gemstone may be more intense, darker, lighter, or a different color (Zagoritis, 2022). The primary goal of heat treatment is to change the color or the clarity permanently and irreversibly. Blak *et al.* (1982) attempted to compare thermal treatments on green and blue beryl crystals from different regions. The optical absorption spectra of both beryls showed characteristic ferrous ions (Fe^{2+}). Infrared spectra showed that alkali content in green beryl is mostly in structural channels, while it is mostly at substitutional and/or interstitial sites in blue beryl. Thermal treatments above 200°C could convert green beryl to blue beryl by converting ferric ions (Fe^{3+}) to Fe^{2+} . However, heat treatment had no effect on the color of blue beryl. In 2007, heat treatment was used to study aquamarine from Altai, Siukiang, and China. Color, quality, and inclusions were all affected by thermal

treatments at 480-500°C. The appearance of tiny black inclusions was one example of the effect. This was due to carbon, which was formed as a result of the reduction of original fluids in the inclusions (Ruzeng, Hongyi, and Minjie, 2007).

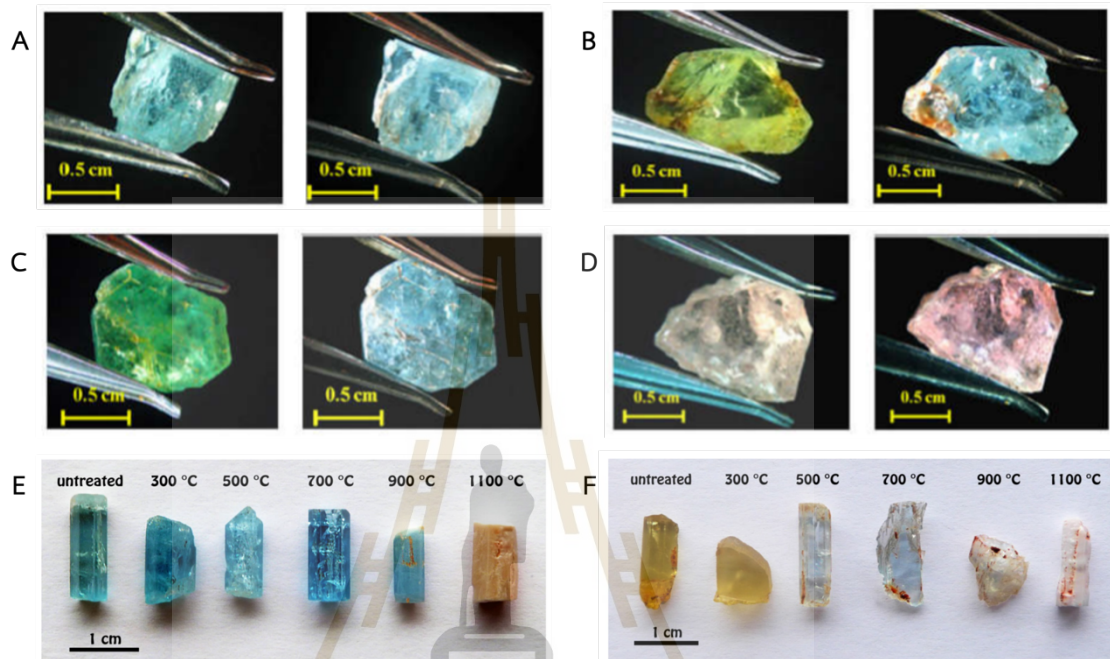


Figure 2.2 Greenish blue (A), greenish yellow (B), yellow green (C), and orangish pink (D) Madagascar samples before and after heat treatment in the electric furnace under reducing atmospheres at 400°C (Chankhantha and Thanasuthipitak, 2012). Aquamarine beryl (E) and yellow beryl (F) samples from Vietnam before and after heat treatment in the muffle furnace under air atmospheres for 12 hours at heating rates of 300, 500, 700, 900, and 1,100°C (Fridrichová *et al.*, 2015).

Greenish blue beryl, greenish yellow beryl, yellowish green beryl, and orangish pink beryl from Madagascar were heat-treated in an electric furnace in 2013 and their colors changed (shown in Figure 2.2: A-D). Thermal treatment in reducing atmospheres at 350°C changed orangish pink to a more intense pink color and at 400°C, the first three groups changed to an intense blue color. After heat treatment, the intensity of the Fe^{2+} characteristic in the octahedral site increased slightly. This was

due to the conversion of Fe^{3+} to Fe^{2+} in the octahedral site. However, heating had no effect on Fe^{2+} in the channel site, despite the fact that it plays an important role in blue coloration (Chankhantha and Thanasuthipitak, 2012). In 2014, 80 aquamarine rough samples from undisclosed sources were heated under two conditions: atmospheric and reducing. Because they could cause the $\text{Fe}^{2+}/\text{Fe}^{3+}$ charge process, both conditions increased the blue intensity of aquamarine. However, because the characteristic Fe^{2+} in the channel site increased, the reducing condition provided a more enhanced blue intensity (Bunnaq and Wanthanachaisaeng, 2014).

Color enhancement in aquamarine and yellow beryl from Vietnam were studied using various heating rates. For 12 hours, the muffle furnace was set to heating rates of 300, 500, 700, 900, and 1,100°C in an air atmosphere. After that, they were cooled to room temperature for 12 hours. Figure 2.2(E and F) depicts the best color and clarity of yellow beryl and aquamarine, which were obtained at 700°C. Heating the yellow beryl at 500°C resulted its original yellow color being replaced by a very pale blue. Heating the aquamarine sample below 700°C resulted in an intense blue with improved clarity while heating it at 700°C resulted in a desirable dark blue color, and a significantly improved clarity without a green tinge. Mössbauer spectroscopy techniques confirmed that the color change was caused by a reduction of Fe^{3+} to Fe^{2+} when heated to 700°C. When heated to 900 and 1,100°C, the crystal structure of both groups showed cracks and fissures (Fridrichová *et al.*, 2015). The gemological properties of green beryls from Madagascar after heat treatment have been studied. The X-ray absorption near edge spectroscopy (XANES) technique was used to investigate the conversion of the iron oxidation state after heating. XANES spectra showed that heat treatment converted Fe^{3+} in the octahedral site to Fe^{2+} . Because the undesirable yellow tinge in the stone was expelled, an appealing blue color developed (Chankhantha *et al.*, 2016).

2.2.2 Irradiation and implantation treatment

Bordas and Crookes (1900) used radium salts as radiation sources to change blue sapphires and diamonds green. Many different types of radiation are used in gemstone treatment innovation. The radiation process for changing the color of

gemstones is simple. The process involves exposing radiation sources to a gemstone, which causes electrons to be knocked-off of some of the atoms, allowing them to be absorbed by others. These have the effect of forming color centers, which alters the gemstone's light-absorbing pattern and color extension. Depending on the nature of the color center produced, the enhanced gemstone may result in stable or unstable colors (Ahmed, 2009). Irradiation may cause gem color to become unstable and revert to the original tone (Nassau *et al.*, 1997). Irradiation is now commonly used in the color treatment of diamonds, beryl, pearls, topaz, sapphire, amethyst, and tourmaline (Zagoritis, 2022). Ion Implantation is a new technique for improving the color of gemstones (Bootkul *et al.*, 2015). In the journal *Atoms for Peace*, Ahmed (2009) stated that neutron irradiation, gamma rays, and electron beams can be used to improve the color and clarity of beryl. The addition of color and clarity to these gems, which would otherwise be devoid of these characteristics, results in significant value addition.

Brazilian researchers investigated the effects of gamma radiation on colorless beryl in 2002. A large slab of natural colorless beryl crystal from Salinas (state of Minas Gerais, Brazil) cut in plane-parallel (PAE) and perpendicular (PEE) to c-axis, was used for the Electron spin resonance (ESR) and Optical absorption (OA) properties measurements. Another section of the crystal was crushed and sieved to reduce grain sizes. The diameter as measured by the Thermoluminescence (TL) measurements was between 0.069 and 0.180 mm. The samples were then annealed at 450°C for 60 minutes in air before being gamma-irradiated prior to all measurements. Gamma radiation experiments were conducted at room temperature using a ^{60}Co source. The radiation process used increased gamma energy in the dose range of 5 Gy to 10^6 Gy. In all radiation doses, they observed a significant and isolated TL growth curve at 165°C, but the curve did not indicate H^0 center. Furthermore, their results indicated that the ESR signal of the sample radiated at 10^6 Gy revealed an EPR signal of Fe^{3+} at $g = 4.257$. The band at 315-326 nm in the OA spectrum was caused by ultraviolet charge transfer (UVCT) from O^{2-} to Fe^{3+} in the tetrahedral Be^{2+} site. They then concluded that there was a correlation between the OA spectra and the ESR signal. The study results of both techniques were related to Fe^{3+} , and the correlation was reasonable as a result (Mittani *et al.*, 2002).

The following year, Khaibullin *et al.* (2003) studied natural beryl colorless crystals from Ural Mountains, Russia. Ion implantation treatment of samples allows the introduction of any chemical element into the near-surface layer of materials, which can change the color of natural minerals. Natural colorless beryl was implanted with iron ions at room temperature with 40 keV in the range of $0.5\text{-}1.5 \times 10^{17}$ ion/cm². After thermal annealing at 600°C for 30 minutes in oxygen, the color of the iron-irradiated beryl changed to pale yellow or yellow-orange with golden metallic luster. Their results indicated that the thermal annealing of the iron-irradiated beryl sample resulted in an inward diffusive redistribution of iron ions. The yellow tone in colored beryl was determined by the appearance of optical absorption bands associated with charge-transfers of O²⁻ to Fe³⁺ and O²⁻ to Fe²⁺, Fe³⁺. The implanted iron ions were in optically active Fe²⁺ and Fe³⁺ states and could replace beryllium and aluminum host ions, respectively, in regular sites. The golden beryl was investigated using optical, Mössbauer, and Rutherford backscattering spectrometry. The nature of the induced coloring, valence state, and depth distribution of implanted iron ions in synthetic golden beryl were determined.

Idris *et al.* (2012) investigated the effects of electron beam irradiation on precious and semi-precious gemstones from various parts of Pakistan, including aquamarine beryl. The goal of this research was to assess gemstone color enhancement. All the gemstones in this study were irradiated with electron beams at doses ranging from 25 kGy to 200 kGy. The samples were sealed in plastic bags and transported on a trolley. Without cooling, the samples were exposed to ionizing irradiation at 2 MeV energy and 10 mA beam current. The results showed that the electron beam irradiation did not only improve the color but also the clarity of some gemstones. The study indicated that many factors, such as impurity, color center, and charge transfer, contributed to color changes in natural gemstones. Considering impurity is the cause of gemstone color, the element of impurity in low concentrations is an essential factor. They also stated that if the oxidation state of the impurity changes, the color could also change. After being radiated, the aquamarine light blue color was clarified. When green or yellow beryl was exposed to ionizing radiation, it lost ferric iron and turned blue. Furthermore, they concluded that 50 kGy was the

optimal dose of gemstone irradiation for visible color changes. Electron beam irradiation below 9 MeV did not result in radioactivity after the gemstones were exposed.

Radiation dosimetry of high doses of beta-rays was studied in blue beryl crystal. The blue beryl crystal was crushed and sieved to retain grains ranging from 0.180 mm to 0.075 mm. Two grains of powder were subsequently combined with silica balls inside a tightly sealed pot and subjected to a rotating mill for 2 days to produce very small grains. The powder was then pressed and sintered at 850°C for five hours to produce small beryl pellets (5 mm in diameter and 3 mm thickness). The small beryl was used to measure high beta ray doses produced by an electron accelerator at the Institute for Energy and Nuclear Research (IPEN). Six pellets were irradiated with doses ranging from 10 kGy to 100 kGy. Thermoluminescence (TL) technique was used to investigate the effect of different doses of beta radiation on beryl pellets. The TL growth curves of all dosimeters had two peaks, one at 230°C and the other at 310°C. The intensity of the TL growth curve at 230°C decreased when doses greater than 30 kGy were applied, but the TL growth curve at 310°C shifted to 340°C as doses increased, and that peak grew linearly for all dosimeters. According to the study, the TL peak grew linearly, which was desirable behavior for radiation dosimetry. Furthermore, the study indicated that blue beryl pellets could be used for high dose dosimetry of beta rays (Carmo, Watanabe, and Bittencourt, 2015).



Figure 2.3 Three rough aquamarine samples from the same source, before enhancement (left), implanted with nitrogen ions (middle), and heated at 400°C under reducing atmosphere (right). (Luangpakdee *et al.*, 2016).

The effect of heat treatment and nitrogen ion implantation on Zambian aquamarine was investigated by Luangpakdee *et al.* (2016). The yellowish-green beryl sample was treated in vacuum for 30 hours with nitrogen ions implantation at 50 keV. The aquamarine sample was implanted, and the yellowish-green color changed into an intense yellow without fracture (Figure 2.3, middle). The other yellowish-green beryl sample was heated in reducing atmosphere at 400°C, with a heating rate of 300°C/hour for 1 hour and then cooled to room temperature for about 2 hours. When the aquamarine sample was heated, the yellowish-green color changed to blue without yellow tinge and revealed more fractures (Figure 2.3, right).

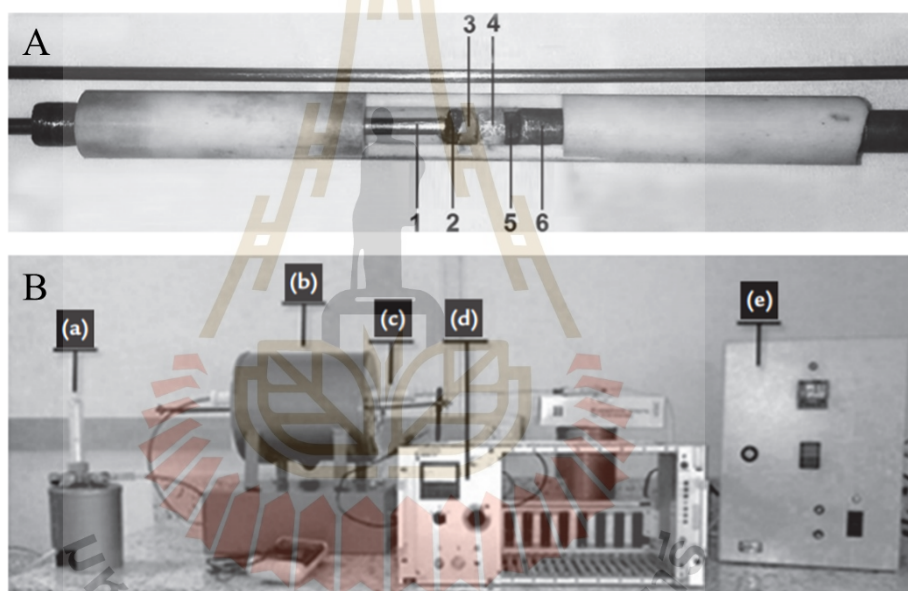


Figure 2.4 Experimental setup for electrodiffusion; (A) sample holder: anode (1), graphite pellet (2), salt with the contaminant ion (3), aquamarine sample (4), graphite sample (5), cathode (6). (B) experimental setup of temperature-controlled electrodiffusion: a) nitrogen flow controller, b) cylindrical oven, c) sample holder, d) voltage source, and e) oven controller (B). (Alkmim *et al.*, 2017).

The optical properties were measured using the UV-Vis-NIR Spectrophotometer. The color of the stone changed to yellow after the nitrogen ion implantation experiment. The decrease in absorption of Fe^{3+} at 370 nm and increase

in absorption of Fe^{3+} at 480 nm might have led to the combination of Fe^{3+} in Al^{3+} site and Fe^{2+} in channel site, which caused the greenish and yellowish color cast in aquamarine. The yellow color in aquamarine sample was removed by heating at 400°C under the reducing condition. The oxidation state of the Fe^{3+} changed to Fe^{2+} in the octahedral site.

In 2017, a researcher from Centro de Desenvolvimento da Tecnologia Nuclear (CDTN), Brazil, investigated a multicolored natural beryl gemstone. They revealed that exposure to ionizing radiation, heating, and possibly electrodiffusion could induce or modify the colors of natural beryl gemstones. Two colors of samples, greenish aquamarine, and blueish aquamarine were chosen for the study. They modified Chen *et al.* (2010)'s electrodiffusion experimental setup, which consisted of a cylindrical oven with a quartz tube containing the sample holder. Stainless steel and tungsten were used for the cathode and anode, respectively. In the experimental setup, the temperature was controlled by an oven controller. Figure 2.4 depicts the assembly of the holder sample and oven controller. They used a temperature of 600°C for six hours in all experiments, with a heating rate of 10°C per minute. The voltage ranged from 1500 V to 3000 V, with nitrogen flow maintaining an inert atmosphere. Furthermore, they conducted two experiments in which samples were cut from the same crystal. In the first experiment, both samples were electrodiffused under the same conditions, but without the ion donor salt pellets. In the second, the voltage was also turned off, and the sample was only heated. In the final experiment, the samples were irradiated to a dose of 4000 kGy in an MDS Nordion IR-214 series, GB-127 panoramic, multipurpose gamma irradiator with a ^{60}Co gamma ray's source.

Infrared spectroscopy (FTIR) technique was subsequently used to investigate the color change in beryl. They concluded that electrodiffusion performed under the conditions of this study did not change the FTIR spectra of both color samples, but color change observed in the FTIR spectra were caused by heating. The FTIR spectra of the greenish sample were significantly altered by gamma irradiation and heating. The evidence was a decrease in the band at 3663 cm^{-1} , which could be attributed to the position of Na^+ ions in the beryl channel along the c-axis (Figure 2.5).

Furthermore, they suggested that green samples contain more type I water molecules, whereas blue samples contain more type II water molecules (Alkmim *et al.*, 2017).

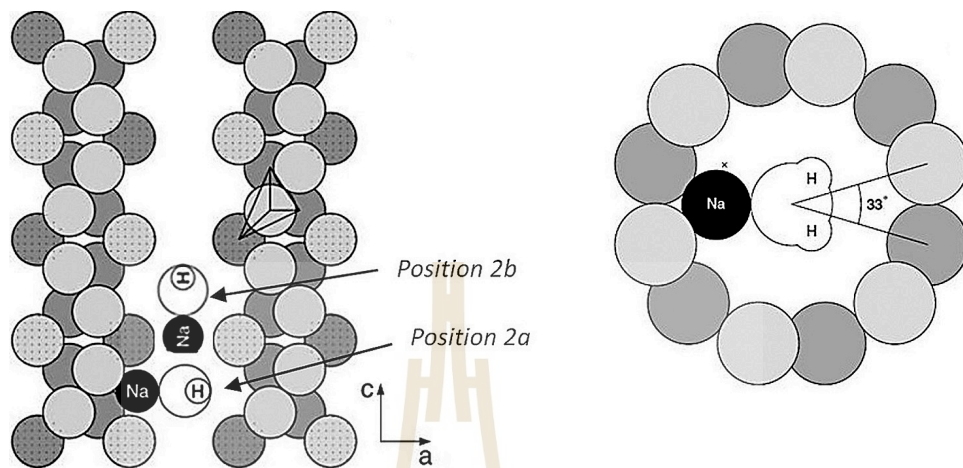


Figure 2.5 Alkalis and water representation in the channels of beryl lattice: a) beryl channel with Na⁺ ion at position 2a interacting with type I H₂O molecule, and Na⁺ ion at position 2b interacting with type II H₂O molecule; b) Na⁺ at position 2a seen from above the plane perpendicular to the c-axis (001). (Anderson, 2006).

2.3 Synchrotron X-ray energy

Synchrotron light is an electromagnetic wave emitted by a charged particle, such as electrons, moving at near-light speeds. When the action of a magnetic field is forced to change direction, electrons lose energy and discharge in the form of electromagnetic waves known as "synchrotron light."

2.3.1 X-rays produced by Siam Synchrotron Light Research Institute (SLRI)

The Siam Light Laboratory generates X-rays from synchrotron light using an electron gun to generate massive amounts of electrons. That is, using electricity to heat the cathode until electrons are released. The electrons are then drawn into a linear accelerator by applying a high positive voltage. The linear accelerator uses microwaves to accelerate electrons to the desired velocity of 40 Mega electron volts (40 MeV). The electrons are then fed into a booster synchrotron, which uses radio

waves to increase electron energy in a circular motion. The circular accelerator forces electrons to move in a circular pattern, accelerating them until they reach a balmy energy level of 1,000 Mega electron volts (1 GeV), or nearly the speed of light. The electrons are then transferred into a storage ring, where their energy is increased to 1,200 Mega electron volts (1.2 GeV). The storage ring is made up of different types of magnets, such as dipole, quadrupole, and sextupole magnets, and is used to force these high energy electrons to move in a vacuum tube. Finally, the electron is forced to move using a magnetic field to change direction and emit light or photons and store the electrons produced. The beamline system for the experiment station is then transferred to the end-stage (SLRI, 2015).

2.3.2 X-ray white beam energy radiation of SLRI

The Siam Photon Source (SPS) has a relatively low electron energy of 1.2 GeV. The light source may be capable of providing users with synchrotron light that is limited to the visible, ultraviolet, and soft X-ray regions. This satisfies user demand for higher energy X-rays. High magnetic fields have been installed to extend the available spectral region and increase photon flux. As a result, a 2.4 T Multipole wiggler (MPW) insertion device has been installed in the storage ring. MPW devices, which consist of three experiment stations, can generate hard X-ray energy in the 5-20 keV range. One is for X-ray scattering experiments (SAXS and WAXS). Another is optimized for X-ray microtomography (XTM), and the last is optimized for X-ray absorption spectroscopy (XAS). Figure 2.6 depicts the spectral flux densities of SPS (Sudmuang, 2014).

X-ray imaging microtomography experimental station (BL1.2) generates X-ray images using high-energy X-rays from the 2.4 Tesla MPW permanent magnet. The MPW's polychromatic X-ray beam is optimized using white-beam slits (WB slit) and a toroidal focusing mirror (FM). The beryllium window (Be window) filters low energy X-rays (4 keV), allowing high energy X-rays to enter the X-ray imaging microtomography experiment (Figure 2.7). At the sample position, these will define the X-ray beam up to 8x3 mm (HxV). It has a sharp beam, high intensity, and excellent penetration. As a result, white-beam responds to detailed material-related questions and can be used to investigate the atomic structure of various elements.

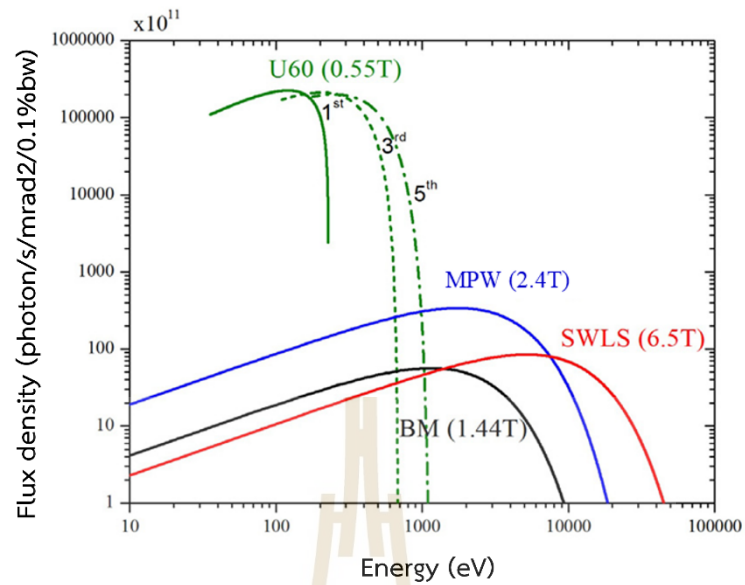


Figure 2.6 SPS comparison of spectra from different sources. (BM = bending magnet, SWLS = superconducting wavelength shifter, MPW = multipole wiggler, and U60 = SPS Halbach-type planar undulator).

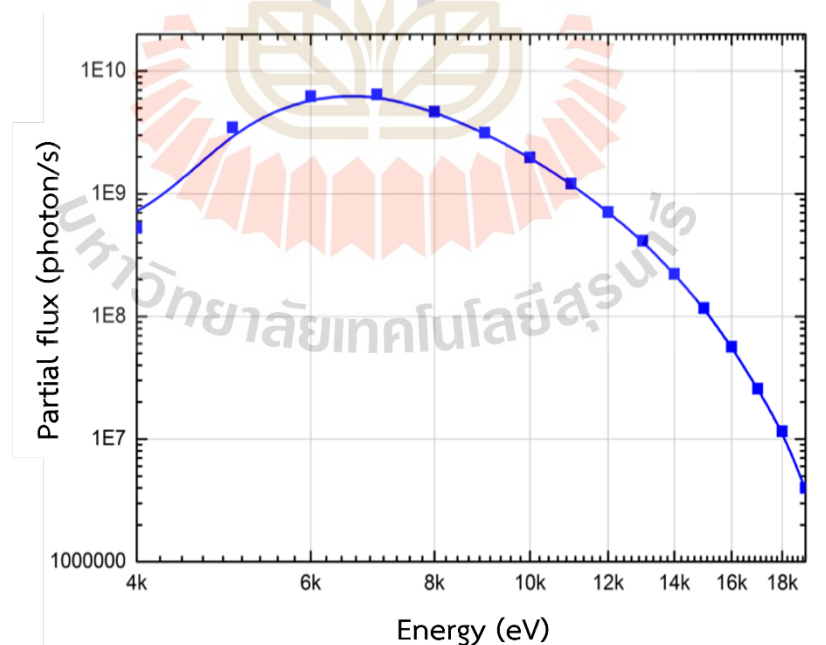


Figure 2.7 The sample position of BL 1.2 W with the partial flow measured as a function of the energy present.

2.3.3 Application of X-ray synchrotron

Many material properties can only be understood by looking at their microscopic structure. Synchrotron X-ray white beam can be used for high-performance material analysis, such as spectroscopy, diffraction, and imaging. The ability of synchrotron light to accurately discover trace elements allows it to be used in a wide variety of basic research applications, including the discovery of atomic and molecular properties and the length of bonds between atoms in molecules of matter, the study of property changes of materials under high pressure and temperature, the study of certain magnetic properties, and the study of the arrangement of atoms on the surface and toxic residues in the environment.

In addition, synchrotron light is crucial to the investigation of bio molecular matters with small and complicated structures, which are typically found in living organisms, such as proteins, nucleic acid, etc. Protein crystallography, which examines the three-dimensional structure of proteins, can be used in the pharmaceutical industry to create active pharmaceutical ingredients, and infrared micro-spectroscopy, which can be used to categorize stem cells, are just two examples. Synchrotron light is also utilized in industrial research, such as developing new goods or improving old ones by leveraging new information to increase their economic value. The ability of synchrotron light to cover nanometers to micrometers is used to investigate micro particle size, especially in cutting-edge industrial materials. Synchrotron light can also be used to investigate gemstone components like atomic structure modification to optimize their appeal and marketability. In 2014, Synchrotron X-rays changed the color of freshwater pearls. Using this discovery, a cheap freshwater pearl was converted into a beautiful golden pearl.

CHAPTER III

MATERIALS AND METHODS

This chapter goes over the experimental procedure, experimental setup, sample materials, and characterization techniques used in this work in detail.

3.1 Experimental procedure

In this study, an X-ray white beam at BL1.2W (SLRI) was used to irradiate a beryl gemstone. Beryl samples from South Africa, including colorless, light blue, blue, yellowish blue, yellow, and deep blue synthetic beryl were chosen. Each color sample was divided into two types: crystal samples were used to observe the color change, whereas powder samples were used to investigate the reaction mechanism. Five different experimental methods were utilized to compare the physical and chemical characteristics of the beryl before and after irradiation. Electron probe microanalyzer (EPMA) data was used to calculate elemental abundances. To determine the effects of radiation, X-ray Diffraction (XRD) was used to investigate the crystal structure. X-ray absorption spectroscopy (XAS) was used to examine the local structure, oxidation states, surrounding symmetry, and neighboring surrounding of the atoms, including coordination numbers and bond distances. The free radicals, unpaired electrons, and paramagnetic characteristics were studied by means of electron paramagnetic resonance (EPR). Beryl crystal coloration was tracked using UV-Vis spectroscopy with reflection probe, and water molecules hue were observed by the near infrared (NIR) spectroscopy.

3.2 Sample materials and sample preparation

The five natural beryl samples used in this thesis were chosen based on their color classification and designated as follows: colorless color as BL1, light blue color as BL2, blue color as BL3, yellowish blue color as BL4, and yellow color as BL5. Normally, natural samples are difficult to identify since they contain different impurities

despite being collected from the same source. BL6 is a synthetic sample with a deep blue color. The crystal fragments, each of which is a different color sample obtained from a bigger crystal, are shown in Figure 3.1.

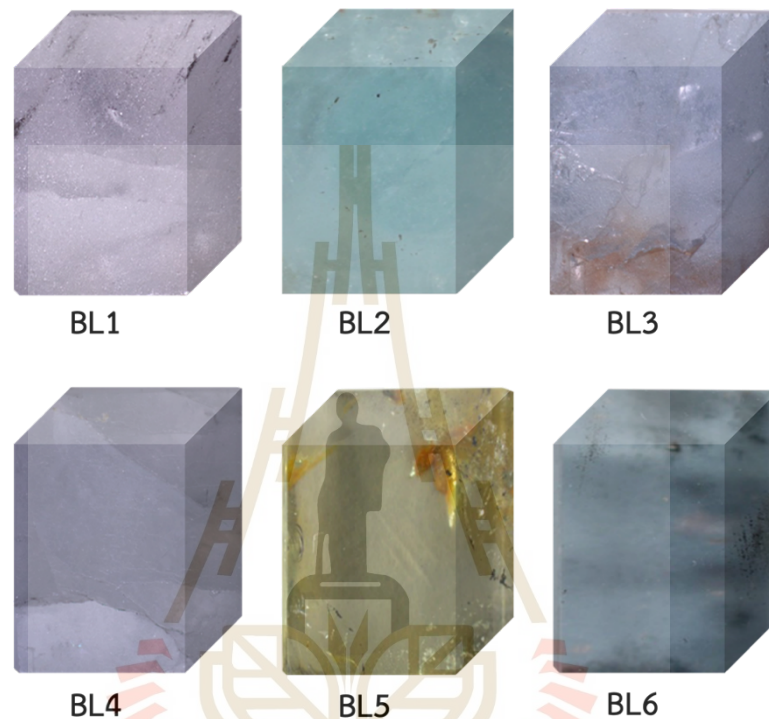


Figure 3.1 The six groups of beryl samples used in this project, classified based on their hue and origin: BL1, BL2, BL3, BL4, BL5, and BL6 (synthetic).

For the purpose of analyzing different characteristics of beryl using various methods, the six samples were separated into crystal and powder forms. Large crystals with more than two inches of beryl in each color were cut by a gemstone cutting machine. The crystals were polished with various sorting papers until an approximate size of 4x4x4 mm (HxVxW) was obtained, which were then used for color change observation. Powder samples were crushed with an agate mortar and pestle before being milled in a mini ball mill to reduce the particle size and homogenize the sample. Furthermore, the powder sample was sieved to a particle size of less than 15 microns in order to investigate the mechanism of beryl before and after X-ray irradiation.

3.3 Experimental setup

The high energy X-rays produced by the 2.4 Tesla MPW permanent magnet were used to produce a polychromatic X-ray beam. Then, white-beam slits (WB slit) and toroidal focusing mirrors (FM) were used to optimize it. The beryllium window (Be window) was used to filter low energy X-rays (4 keV), allowing high energy X-rays to enter the beryl irradiation experiment (Figure 3.2).

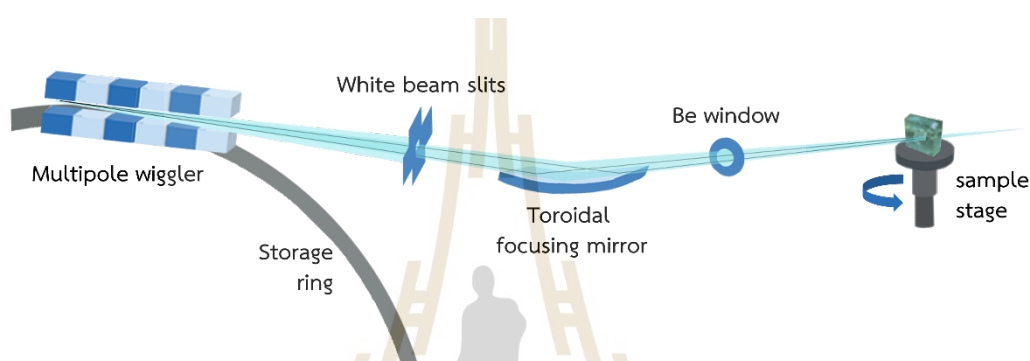


Figure 3.2 Irradiation of samples with white beam X-rays from 2.4 Tesla MPW permanent magnet SLRI sources.

The beryl sample was positioned on a sample stage that could rotate 360 degrees. The beryl crystal samples moved continuously during the X-ray radiating process, as opposed to the powder beryl samples. Radiation was used with an X-ray full beam size of 8x3 mm (HxV). The exposure durations for beryl powder samples were 30 seconds, 1 minute, 4 minutes, and 10 minutes, with an extended duration of 10 minutes specifically for inducing color changes in beryl crystals. Additionally, to discern and compare color alterations in natural and synthetic beryl crystals, exposure periods of 0.5, 1, 4, 10, 20, and 60 minutes were employed.

3.4 Characterization techniques

The characterization techniques used in this thesis included powder and crystal samples, based on the aforementioned objective of the study.

3.4.1 Electron Probe Micro Analyzer (EPMA)

A JEOL model JXA 8100 Electron Probe Micro Analyzer provided by the department of Geology, Chulalongkorn University, was used to determine the chemical components of beryl. Each hue of beryl crystal was cast using silicone gel, and then the surface of the sample was polished in preparation for the EPMA experiment. The experiments were carried out on a high aperture spectrometer that had an accelerating voltage of 15 kV, a beam current of 10 nA, and a beam size of 5 μm . Each color group of beryl underwent measurement at five distinct spots to obtain averaged EPMA results. Empirical equations for beryl were derived by doing calculations with 18 oxygen atoms, with FeO representing the entire quantity of iron present in the beryl sample.

3.4.2 Coloration measurement

The CIE 1976 $L^*a^*b^*$ color space, a widely used color space for expressing colors of objects, was used to explain the observation of the color changes in beryl crystal when exposed to X-ray irradiation (Ly *et al.*, 2020). In the $L^*a^*b^*$ color space, L^* represents the lightness component and ranges from 0 to 100 (from black to white). The chromaticity components, a^* and b^* , a^* ranges from $-a^*$ (green) to $+a^*$ (red), while b^* ranges from $-b^*$ (blue) to $+b^*$ (yellow) (Wang *et al.*, 2022a). Figure 3.3 depicts the CIE 1976 $L^*a^*b^*$ color space. Color was measured using UV-Vis spectrometers (Ocean Optics QE-Pro model). The Ocean Optics DH 2000 model employs Deuterium and Halogen light sources. The WS-1-SL diffuse reflectance standard, Spectralon, from Ocean Optics was used in the spectral range of 250-2500 nm. The color of the beryl crystal was measured with 45-degree reflection probe and calibrated at room temperature using D65 2 degrees standard.

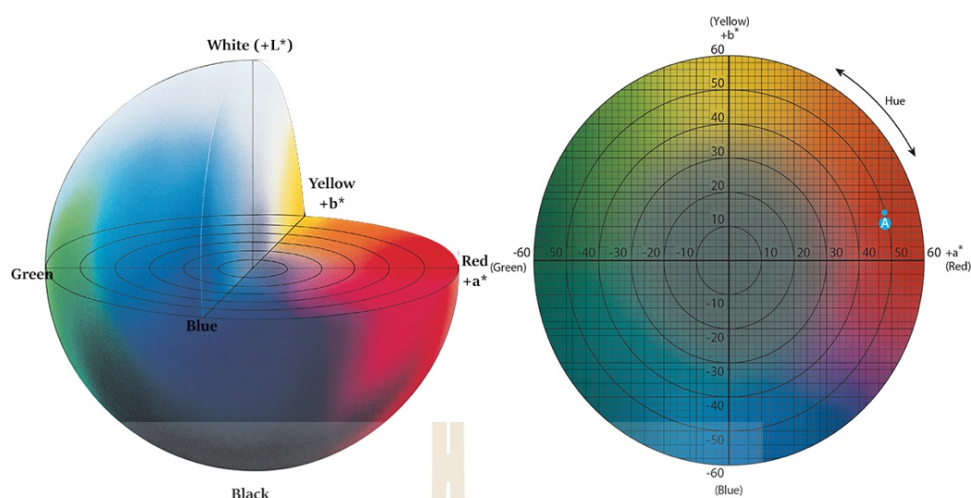


Figure 3.3 The CIE 1976 $L^*a^*b^*$ color space depicted in 3D and 2D diagrams.

3.4.3 Ultraviolet Visible and Near infrared spectroscopy (UV-Vis-NIR)

The absorbance spectra of beryl crystal samples were measured with the PerkinElmer LAMBDA 950, a high-performance UV/Vis/NIR spectrophotometer. The UV-Vis-NIR spectrophotometer measures the intensity of light in the UV, visible, and near-IR regions using integrating spheres ranging from 250 to 2000 nm. The UV/Vis resolution reaches up to 0.05 nm, while the NIR resolution reaches up to 0.20 nm. Deuterium and tungsten halogen were used as light sources, and all measurements were taken at room temperature with unpolarized light sources. Absorbance spectra fingerprinting was used to identify the types and densities of active compounds in the samples. The broad peak features of absorption spectra in the UV-Vis region were used to explain how the absorbance feature changed after X-ray irradiation, while the NIR region was used to track the changes in water and OH molecules.

3.4.4 X-ray Diffraction (XRD)

In this study, the diffraction techniques were divided into two sub-techniques: crystal plane studies and powder diffraction of powdered beryl in capillary. The crystal plane was used to observe the XANES features of different X-ray polarized beryl structures, which were polarized to the basal plane and prismatic plane. An X-ray diffractor was used to confirm the crystal planes obtained from the samples' faces.

A Rigaku SmartLab diffractometer in step scanning mode, with a step size of 0.02, and a count time of 10 seconds per step, was used to collect X-ray data in the range of 10-50 in 2θ . The measurements were carried out at room temperature using Cu-K α radiation ($\lambda = 1.54 \text{ \AA}$) at 40 kV and 40 mA.

The diffractograms of beryl powder in capillary were used to examine the crystalline structure of each beryl color and to observe effect of X-ray irradiation on the beryl structure. The capillary spinning averages each plane of the beryl structure, which could eliminate a preferred crystal orientation. The Debye-Scherrer powder diffraction was carried out in the capillary at BL1.1 W (SLRI). As shown in Figure 3.4, the diffractometer employs near-parallel incident beam X-rays with a large enough cross-section to bathe the entire powder sample. The monochromatic (12 keV) beam from a double crystal monochromator (Si111), and a 0.3x4 mm (VxH) X-ray beam was cut by a 4-blade programmable slit before reaching the capillary sample. During the experiment, the beryl powder was loaded into a 0.3 mm capillary diameter and spun at 600 rpm using a high-speed goniometer head. The diffraction signal was collected using DECTRIS Mythen6K 450 a strip detector with overall 20 minute/sample.

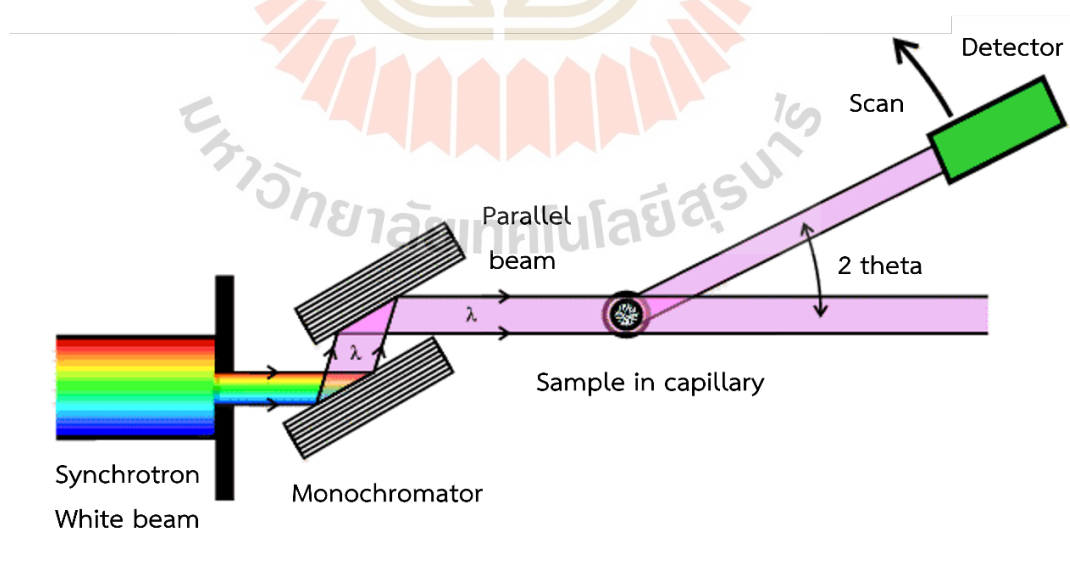


Figure 3.4 Schematic of the Debye-Scherrer diffractometer.

3.4.5 X-ray absorption spectroscopy (XAS)

The photoelectric effect explains how light is absorbed by materials. The phenomenon, depicted in Figure 3.5(a), occurs when an X-ray photon is absorbed by an electron in a tightly bonded core level, such as the $1s$ (K) or $2p$ (L) level of an atom. A core electronic level can absorb X-rays if its binding energy is lower than the incident X-ray energy. If the binding energy is higher than the energy of the X-ray, the bound electron will not be disturbed and will not be able to absorb the X-ray. To be taken out of its quantum state, an electron must have a binding energy lower than that of the X-ray. In this situation, the X-ray is absorbed, and the excess energy is transferred to a photoelectron that is then ejected from the atom at high speed. The absorption coefficient (μ) offers the likelihood that X-rays will be absorbed according to Beer's Law where I_0 is the X-ray intensity incident on a sample, t is the sample thickness, and I is the intensity transmitted through the sample.

$$I = I_0 e^{-\mu t} \quad (3.1)$$

The absorption coefficient is a smooth function of energy whose value is determined by the sample density (ρ), atomic number (Z), atomic mass (A), and X-ray energy (E).

$$\mu E \approx \rho Z^4 / A E^3 \quad (3.2)$$

The main information obtained from XAS spectra is in the form of small changes in the absorption coefficient, which can be measured directly in a transmission mode or indirectly in a fluorescence mode (Figure 3.5(b)). The term XAS refers to both the X-ray absorption fine structure (EXAFS) and the X-ray absorption near-edge structure (XANES). The XANES region is accessible in the XAS signal spectrum from near the atomic absorption edge (pre-edge) to about 50 eV above the absorption edge. The XANES structure is generated by absorbing X-rays from deep energy layers (Core electrons) and transferring their energy states to empty states (empty orbital) within the atom. The EXAFS region appears in the XAS signal spectrum above the absorption

edge, following the XANES structure (500 eV to 1,500 eV). The EXAFS structure is formed by photoelectrons emitted by atoms during absorption, which behave in waves and cross paths with surrounding atoms, scattering, and interfering with oneself. Figure 3.5 displays the XAS spectra as well as the electron energy transfer state after atomic absorption.

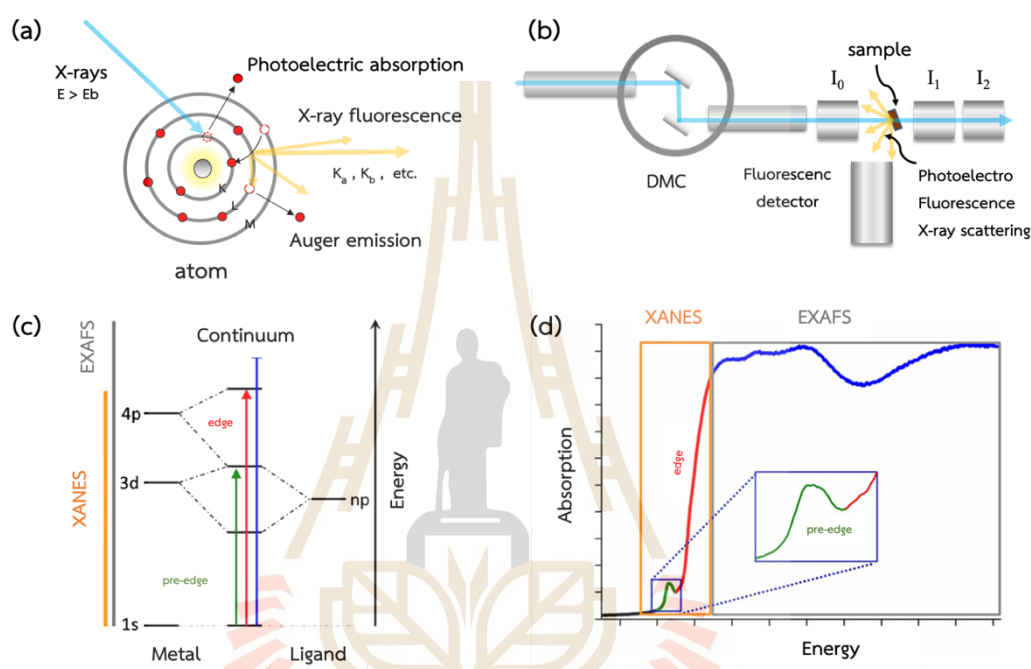


Figure 3.5 XAS illustration: (a) X-ray absorption in an atom, (b) synchrotron XAS technique setup, (c-d) XAS spectra and electron energy transfer state after atomic absorption.

The XANES region contains near neighbor atomic information of probed element with multiple scattering in the continuum. The XANES feature provides an information of pre-bonding and oxidation state of the adsorbing atom (Guda *et al.*, 2021). Fe K-edge XANES spectra of beryl crystal samples were recorded at BL1.1W MXT of the Synchrotron Light Research Institute (SLRI), Thailand. Due to the low concentration of the Fe trace element in beryl, the measurements were carried out in fluorescence mode using a 19 element Ge detector. The X-ray beam size 4x3 mm (HxV) was used to measure the sample. For measurements, the crystal faces were angled at 45 degrees

to both the incident beam and the fluorescence detector. The absorption energy (E_0) of Fe foil was 7112 eV with a scan range from 150 eV below E_0 to 200 eV above E_0 and a collection time of 1 seconds per point. Each beryl crystal face was aligned to the polarization of X-rays yielded different combination of XANES features (Bunnag *et al.*, 2020). The XANES feature of each crystal face was observed before and after irradiation, with the beryl crystal samples aligned with C axis perpendicular to polarization but with both prismatic (plane A) and basal plane (plane C) facing incoming X-rays, as shown in Figure 3.6.

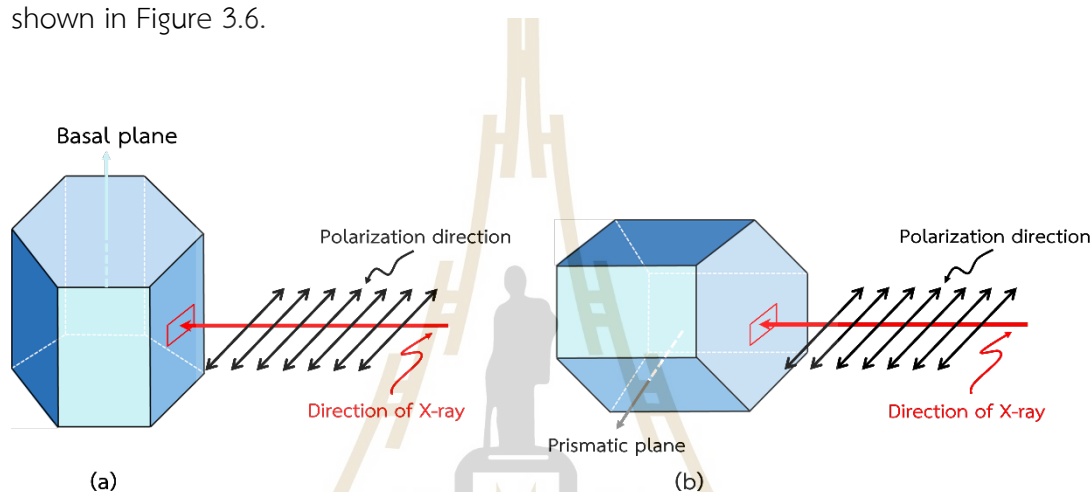


Figure 3.6 Sample orientations with prismatic plane (plane A) and basal plane (plane C) facing incoming X-rays (edit from Bunnag *et al.*, 2020).

The powder sample of each beryl color was analyzed using both XANES and EXAFS regions in XAS technique. The analysis of pre-edge peaks in transition metal oxides to determine oxidation state and molecular configuration is one application of the XANES region. The pre-edge peak is a spectral feature that occurs just before the main absorption edge (typically due to a metal $4p$ electron) of a main K edge and is caused by overlapping of metal d -electrons and oxygen p -electrons (Figure 3.5(c)). It is frequently described in terms of molecular orbital theory (Newville, 2013). For pre-edge base line subtraction, the centroid was calculated using the Larch program. A Linear and Lorentzian function was used to subtract the base line of XANES pre-edge. The pre-edge area was then fitted with a Gaussian function using the Origin program, and the fitting results were analyzed using the MagicPlot program.

The EXAFS feature is the region mainly with single scattering. The EXAFS technique is used to determine a coordination number, the disorder of neighboring atoms, and the distance between neighboring atoms (Hayes and Boyce, 1983). The Fe K-edge EXAFS spectra of beryl powder samples were recorded using a 19 element Ge detector in fluorescence mode at BL1.1W MXT (SLRI). The sample position and X-ray aperture size were comparable with conditions of XANES measurements of crystal samples. The Fe foil absorption energy was 7112 eV, with a scan range of 150 eV below E_0 to 15 keV above E_0 and a collection time of 1 sec per point. Athena and Artemis programs were used to analyze EXAFS data in order to fit the spectrum and generate coordination number and bond range information for iron ions.

3.4.6 Electron Paramagnetic Resonance (EPR)

EPR is a spectroscopic technique that detects unpaired electrons in species. Unpaired electrons are found in an exceptionally wide variety of materials. These include free radicals, numerous transition metal ions, and material defects. EPR spectroscopy is a sensitive method for determining the oxidation state, symmetry, and type of coordination sites in various complex metal ions (Klencsár and Köntös, 2018). EPR measurements on beryl powder samples were performed at room temperature using a Bruker EMX micro spectrometer. The modulation frequency was 100 kHz, the modulation amplitude was 5 G, the microwave power was 152.607 mW, and the microwave frequency was around 9.844 GHz. The spectra were scanned in several ranges, including 500-6500 G (wide range) for 150 secs. The effective g values of the observed EPR signals were used to label them.

The g_{eff} is defined as
$$h\nu = g_{eff}\beta B \quad (3.3)$$

Where B is the external magnetic field in which the EPR signal appears, ν is the microwave frequency used, β is the Bohr magneton, and h is Planck's constant (Rager and Schneider, 1986).

CHAPTER IV

RESULTS AND DISCUSSION

This chapter presents an exhaustive overview and discussion of the experimental analysis and results of the study. The findings have been grouped into the following primary categories: formula computation and chemical composition, coloration and absorbance spectra, and absorption energy, oxidation state, and coordination number of beryls.

4.1 Chemical composition and formula calculation

Element composition, both major and trace element analysis, was investigated using EPMA techniques. The transition elements and alkali element contents (wt.%) of beryl sample are reported in Table 4.1. Consistent with the chemical formula of beryl ($\text{Be}_3\text{Al}_2(\text{SiO}_3)_6$), all the studied samples contained SiO_2 , Al_2O_3 and BeO as major elements. BL2 had the highest amount of Al_2O_3 , with 18.36 wt.% while other samples contained Al_2O_3 between 17.33-17.81 wt.%. Normally, the Al site in beryl structure can be occupied by various transition metal elements because the radius size of Al is similar to those of transition metal ions, such as Fe^{2+} , Fe^{3+} , Cr^{3+} , and V^{3+} (Wang *et al.*, 2022a). Among the alkali elements, Na content varied between 0.019-0.604 wt.%. K was the lowest elemental content in all samples and was not detected in BL6. Ca was found only in BL1, BL2 and BL6. Cs element appeared only in BL6, which might be attributed to other samples having lower Cs concentrations making it harder to detect. Low content of transition metal Mn was found only in BL5. V was found in BL1, BL3 and BL5 samples while Mg appeared in all samples except BL1. Concentrations of Fe in the samples ranged between 0.276-0.681 wt.%, with the synthetic sample having the highest amount of 1.568 wt%.

Table 4.1 The average chemical composition of beryl samples as determined by EPMA.

Chemical com.	Natural					Synthetic
Sample name	BL1	BL2	BL3	BL4	BL5	BL6
Color	colorless	ligh-blue	blue	pale bute	yellow	deep blue
Oxides (wt.%)						
SiO ₂	67.465 (0.031)	66.977 (0.515)	67.517 (0.127)	67.466 (0.081)	67.223 (0.062)	67.710 (0.484)
Al ₂ O ₃	17.326 (0.012)	18.355 (0.146)	17.810 (0.066)	17.623 (0.279)	17.555 (0.151)	17.629 (0.224)
BeO	13.446 (0.172)	13.626 (0.025)	13.880 (0.016)	13.766 (0.172)	13.573 (0.016)	13.758 (0.025)
MgO	bdl	0.005 (0.002)	0.125 (0.023)	0.075 (0.028)	0.137 (0.070)	0.027 (0.009)
MnO	bdl	bdl	bdl	bdl	0.033 (0.015)	bdl
FeO [†]	0.276 (0.031)	0.475 (0.069)	0.681 (0.022)	0.325 (0.047)	0.576 (0.084)	1.568 (0.106)
Sc ₂ O ₃	bdl	0.006 (0.004)	bdl	0.002 (0.001)	bdl	0.011 (0.002)
V ₂ O ₃	0.051 (0.006)	bdl	0.013 (0.001)	bdl	0.006 (0.002)	bdl
CaO	0.027 (0.031)	0.012 (0.004)	bdl	bdl	bdl	0.005 (0.001)
K ₂ O	0.044 (0.004)	0.004 (0.001)	0.029 (0.002)	0.010 (0.002)	0.026 (0.003)	bdl
Cs ₂ O	bdl	bdl	bdl	bdl	bdl	0.005 (0.003)
Na ₂ O	0.604 (0.059)	0.030 (0.016)	0.604 (0.022)	0.249 (0.056)	0.237 (0.046)	0.019 (0.018)
Total	99.239	99.488	100.659	99.514	99.372	100.732
H ₂ O*	1.773	1.285	1.773	1.471	1.461	1.276
Cation (apfu)**						
Si ⁴⁺	6.109	6.040	6.039	6.078	6.079	6.063
Al ³⁺	1.849	1.951	1.878	1.871	1.871	1.860
Be ²⁺	2.925	2.952	2.983	2.980	2.948	2.960
Mg ²⁺	bdl	0.001	0.017	0.010	0.019	0.004
Mn ²⁺	bdl	bdl	bdl	bdl	0.003	bdl
Fe ²⁺	0.021	0.036	0.051	0.025	0.044	0.117
Sc ³⁺	bdl	0.000	bdl	0.000	bdl	0.001
V ³⁺	0.004	bdl	0.001	bdl	0.000	bdl
Ca ²⁺	0.003	0.001	bdl	bdl	bdl	0.000
K ⁺	0.005	0.001	0.003	0.001	0.003	bdl
Cs ⁺	bdl	bdl	bdl	bdl	bdl	0.000
Na ⁺	0.106	0.005	0.105	0.043	0.042	0.003
O ²⁻	18.000	18.000	18.000	18.000	18.000	18.000
∑ cation	11.021	10.987	11.076	11.008	11.008	11.008
CH***	0.114	0.007	0.108	0.045	0.045	0.004
∑ cat. -CH	10.907	10.980	10.968	10.964	10.963	11.005

[†]Total Fe was determined as FeO. *H₂O is estimated from H₂O wt. % = (Na₂O in wt.% + 1.4829)/1.1771 (Guiliani *et al.*, 1997). **Compositions were recalculated on 18 O atoms per formula unit (apfu). ***Channel site (CH) = Na+Cs+K+Ca (Pikry *et al.*, 2014). Abbreviation: bdl=below detection limit.

The significant amounts of H₂O detected in beryl is probably due to the low total oxides typically found in beryl from various localities (Brown and Mills, 1986; Sherriff *et al.*, 1991; Giuliani *et al.*, 1997), however, the electroneutral molecule of H₂O does not influence the formula calculations. The amount of H₂O was calculated by Giuliani and team (1997) in the form of H₂O wt.% = (Na₂O in wt.% + 1.483)/1.177, which yielded a sum of oxides exceeding 100 wt.%.

The cation compositions were recalculated on 18 O atoms per formula unit (apfu) (Přikryl *et al.*, 2014). The calculation results revealed that the Si in beryl composition was close to the stoichiometric value of 6 apfu (6.040-6.109 apfu). Table 4.1 shows the different cation apfu of beryl samples, which indicates that the beryl samples vary from being highly heterogeneous to more homogeneous (Přikryl *et al.*, 2014). The total Al content varied between 1.860-1.951 apfu; Al was substituted by Mg (0.001-0.019 apfu) and mostly by Fe (0.021-0.117 apfu). The decrease in octahedral site charge was balanced by alkali input in the channel (0.004-0.114 apfu), including low K, Ca and predominantly Na. In relation to the ideal occupancy and as a result of the calculation method, the calculated values were comparable. Analytical error and formula calculations are considered to have several causes, including undetermined Be, incorporation of some elements (Fe²⁺, Li) at the CH site (Sherriff *et al.*, 1991; Groat *et al.*, 2010), the presence of OH⁻ in the beryl structure (Ventura *et al.*, 2007).

4.2 X-ray diffraction of beryl structure

Beryl is a hexagonal crystal structure mineral consisting of beryllium aluminum cyclosilicate. The crystallographic properties of beryl, such as lattice constants, unit cell diameters, and the existence of any impurities or structural flaws, can be determined by analyzing the intensity and location of the diffraction peaks in the pattern. In Figure 4.1, the diffractograms of beryl powder showed the 2θ range between 10-60, with XRD patterns of beryl JCPDS-00-009-0430 utilized as a reference pattern (Bunnag *et al.*, 2020). The XRD analysis indicated that the peak shapes and positions of the beryl samples were essentially identical with the exception of sample BL1, which was different at 100% intensity main peak (*). The primary d-spacing values were approximately 7.9744 (100), 4.5985 (002), 3.9872 (200), 3.9836 (102), 3.2536 (112),

3.0125 (202), 2.8641 (211), 2.6581 (300), 2.5208 (212), 2.2992 (004), 2.2117 (310), 2.1504 (311), 2.0570 (114), 1.9918 (204), 1.8294 (320), 1.7936 (313), 1.7390 (304), 1.7098 (411), 1.6268 (224), 1.5949 (500), 1.5710 (323), 1.5328 (006). Additionally, the standard deviation was approximately ± 0.0020 . The diffractograms of beryl powder before (solid line) and after X-ray synchrotron irradiation (dotted line) exhibited the same position pattern, with the intensity and center peak location slightly shifting due to background removal and data processing.

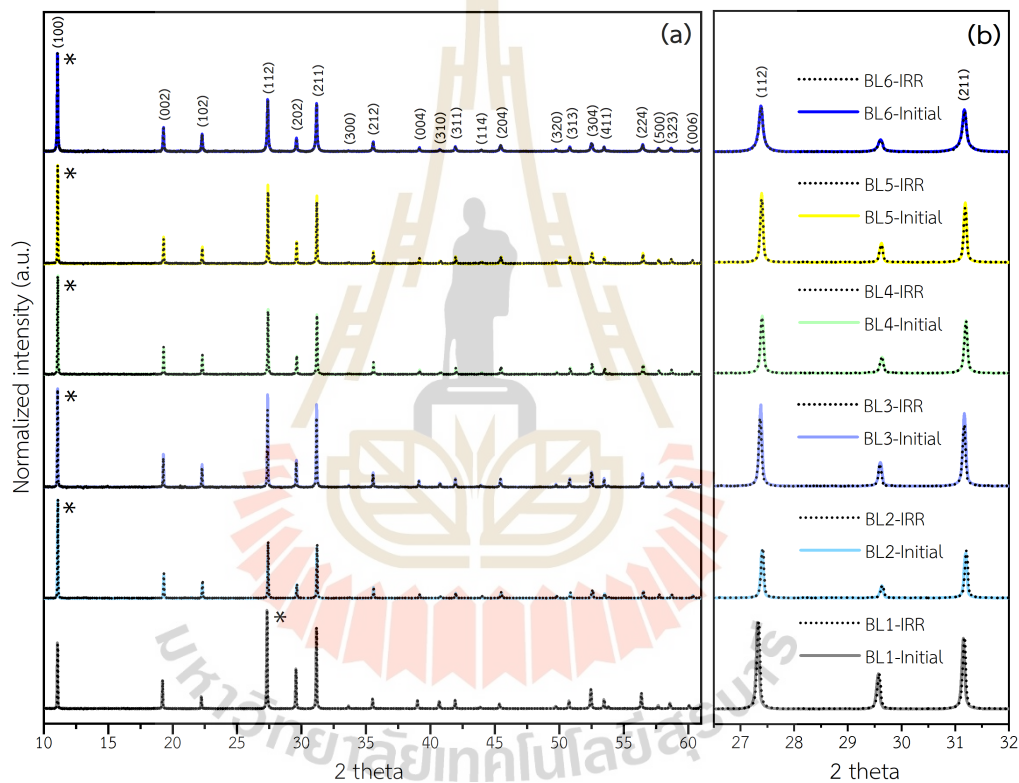


Figure 4.1 The initial powder beryl (solid line) and irradiation powder beryl (dote line) X-ray diffractograms reveal the 2θ between 10-60 (a) and magnification 2θ between 27-32 (b).

The beryl lattice parameters (a and c) were calculated using the d -spacing value of the *hkl* peak, which included (100), (002), (300), (004), (500), and (006). The beryl data summary revealed that a value ranged from 9.2088 to 9.2209 Å, and c values varied from 9.1927 to 9.2325 Å, as listed in Table 4.2.

Table 4.2 Unit-cell parameters of the beryls in this study and their assignment to a substitution series following Aurisicchio *et al.* (1988) in comparison to beryls from Western Carpathian.

	Description	<i>a</i> [Å]	<i>c</i> [Å]	<i>v</i> [Å ³]	<i>c/a</i>		Reference
BL1-Initial	colorless	9.2208 (28)	9.2325 (01)	679.806	1.001	tetrahedral	This work
BL1-IRR	-	9.2209 (29)	9.2325 (26)	679.826	1.001	tetrahedral	This work
BL2-Initial	light blue	9.2119 (61)	9.1928 (92)	675.579	0.998	normal	This work
BL2-IRR	-	9.2117 (10)	9.1933 (10)	675.586	0.998	normal	This work
BL3-Initial	blue	9.2179 (42)	9.2034 (11)	677.250	0.998	normal	This work
BL3-IRR	-	9.2166 (15)	9.2024 (37)	676.981	0.998	normal	This work
BL4-Initial	pale blue	9.2094 (76)	9.1931 (86)	675.249	0.998	normal	This work
BL4-IRR	-	9.2088 (84)	9.1927 (61)	675.121	0.998	normal	This work
BL5-Initial	yellow	9.2138 (42)	9.1958 (76)	676.079	0.998	normal	This work
BL5-IRR	-	9.2139 (40)	9.1962 (71)	676.136	0.998	normal	This work
BL6-Initial	deep blue (syn)	9.2180 (90)	9.2005 (47)	677.039	0.998	normal	This work
BL6-IRR	-	9.2191 (91)	9.2014 (32)	677.278	0.998	normal	This work
PSL	pale blue-green	9.2199 (05)	9.1916 (05)	676.666	0.997	normal	Bačik <i>et al.</i> , 2019
BLS	pale green-yellow	9.2083 (07)	9.1847 (08)	674.457	0.997	normal	Fridrichová <i>et al.</i> , 2016
DUV	pale green-yellow	9.2200 (30)	9.1910 (30)	676.636	0.997	normal	Fridrichová <i>et al.</i> , 2016
SIT	pale green-yellow	9.2619 (04)	9.1837 (07)	682.258	0.992	octahedral	Ozdín, 2010
BN-21a	pale green-yellow	9.2248 (03)	9.2132 (02)	678.977	0.999	tetrahedral	Uher <i>et al.</i> , 2010
PI-15	pale green-yellow	9.2179 (03)	9.2033 (04)	677.233	0.998	normal	Uher <i>et al.</i> , 2010
Sample-3	dark blue	9.2736 (11)	9.1910 (25)	684.526	0.991	octahedral	Aurisicchio <i>et al.</i> , 1988
Sample-12	blue	9.2202 (10)	9.1960 (10)	677.034	0.997	normal	Aurisicchio <i>et al.</i> , 1988
Sample-14	light blue	9.2200 (10)	9.1970 (10)	677.078	0.998	normal	Aurisicchio <i>et al.</i> , 1988
Sample-16	yellow	9.2097 (12)	9.1943 (07)	675.368	0.998	normal	Aurisicchio <i>et al.</i> , 1988
Sample-17	pale blue	9.2150 (10)	9.2000 (10)	676.564	0.998	normal	Aurisicchio <i>et al.</i> , 1988
Sample-21	colorless	9.2180 (10)	9.2300 (10)	679.213	1.001	tetrahedral	Aurisicchio <i>et al.</i> , 1988
S1	colorless (syn)	9.2077 (06)	9.1953 (4)	675.148	0.999	tetrahedral	Aurisicchio <i>et al.</i> , 1988

The unit-cell volume showed a range of 675.121 to 679.826 Å³. When substitutions lead to opposite distortions within the beryl structure, particularly in the octahedron and tetrahedron, two distinct series are formed. The presence of octahedral and tetrahedral substitutes results in contrasting effects. Beryl chemistry is influenced by heterovalent substitutions at octahedral and tetrahedral sites, as observed in previous studies (Wood and Nassau, 1968; Aurisicchio *et al.*, 1988). These substitutions significantly impact the lattice parameters, leading to the categorization of three distinct beryl series based on the *c/a* ratio: (1) The “octahedral” beryls, characterized by the main isomorphous substitutions of Al ↔ Metal ions (*c/a* = 0.991-

0.996); (2) The "tetrahedral" beryls, primarily involving the substitution of Be ↔ Li ($c/a = 0.999-1.003$); (3) The "normal" beryls, where both substitutions occur together, albeit to a limited extent ($c/a = 0.997-0.998$) (Auricchio *et al.*, 1988). The samples consisted of c/a values ranging from 0.998 to 1.001, corresponding to the normal to tetrahedral beryl series. As a result, the beryl samples in this study included both tetrahedral and octahedral substitutions. The colorless (BL1) the only sample belonging to tetrahedral series in this study, while other samples (blue to yellow) belonged to the normal series ranged.

This beryl color and c/a ratio in this study were compared to beryl samples from Auricchio *et al.* (1988) and beryls from Western Carpathian. The color was similar to that of beryls from Western Carpathians, however, the abundance of beryls in various areas had resulted in a variety of series (tetrahedral, normal, and octahedral). The colorless natural and synthetic beryls studied by Auricchio *et al.* (1988) belong to the tetrahedral series, similar to the beryls in this study, which also encompass colors ranging from blue to yellow, characteristic of the normal series. The dark blue beryl belonged to the octahedral series resulting from greater Al ↔ Metal ions substitutions, although it was not found in the beryl samples in this study.

4.3 Beryl coloration and absorbance spectra













4.3.1 Beryl coloration

The color of beryl is determined by the kind and quantity of impurities present within its crystal structure as it forms. Beryl color can be improved through processes like heat treatment or irradiation. In this study, synchrotron X-ray energy was employed to enhance the color and overall appearance of beryl samples.

The CIELab color space values of the initial beryl crystal samples were evaluated using reflection color measurement within the spectral region of 250-2500 nm. After 10 minutes of X-ray irradiation, the natural and synthetic blue color samples changed color to yellow, including yellow beryl, which turned to intense yellow. After X-ray irradiation, the colorless BL1 sample changed to a slightly burnt tone. The CIELab color space values revealed a significant change in b^* value when the color changed to yellow (Table 4.3). The comparison of b^* value showed that colorless beryl only

slightly increased with a little over 3 in value, which was comparable to yellow beryl changing to intense yellow, while blue beryl changed to yellow with a significant increase of around 15-45 in b^* value. The color simulation shown in Table 4.3 and Table 4.4 were calculated using the $L^*a^*b^*$ value of reflection measured at the actual thickness of the sample.

Table 4.3 The CIELab values of beryl samples as determined using a D65 2° illuminant and a reference angle.

Sample	Before irradiation			ζ Color simulation	After irradiation			ζ Color simulation
	L*	a*	b*		L*	a*	b*	
BL1	63.99	-0.28	-0.55		64.83	-3.70	2.58	
BL2	63.93	-3.05	-1.75		67.50	-9.25	13.96	
BL3	56.25	8.36	-31.56		66.57	-12.53	7.80	
BL4	63.88	-5.65	-2.82		68.23	-7.09	41.61	
BL5	68.23	6.20	19.35		68.82	6.25	22.73	
BL6	59.02	2.95	-21.30		64.75	-2.40	2.39	

ζ The color was simulated by website <https://www.nixsensor.com/free-color-converter/>.

Table 4.4 The CIELab values of natural and synthetic beryls as determined using a D65 2° illuminant and a reference angle.













Natural beryl (BL4)	CIELab value			ζ Color simulation	Synthetic beryl (BL6)	CIELab value			ζ Color simulation
	L*	a*	b*			L*	a*	b*	
Initial	63.88	-5.65	-2.82		Initial	59.02	2.95	-21.30	
IRR_1m	65.30	-3.88	4.60		IRR_1m	61.10	-0.10	-13.53	
IRR_4m	69.77	-4.18	29.77		IRR_4m	64.23	-4.69	-0.89	
IRR_10m	68.23	-7.09	41.61		IRR_10m	64.75	-2.40	2.39	
IRR_20m	72.40	-7.38	46.67		IRR_20m	65.94	-2.89	8.18	
IRR_60m	73.90	-0.45	66.73		IRR_60m	66.10	-4.88	8.24	

Table 4.4 depicts the hue of natural and synthetic beryl ranging from blue to yellow. The b^* value of beryl color tended to change depending on the X-ray irradiation duration, with the first stage (1st) being a high b^* value change at 1 to 4 minutes of irradiation and the second stage (2nd) being a lower b^* value change at periods longer than 4 minutes (shown in Figure 4.2(c)).

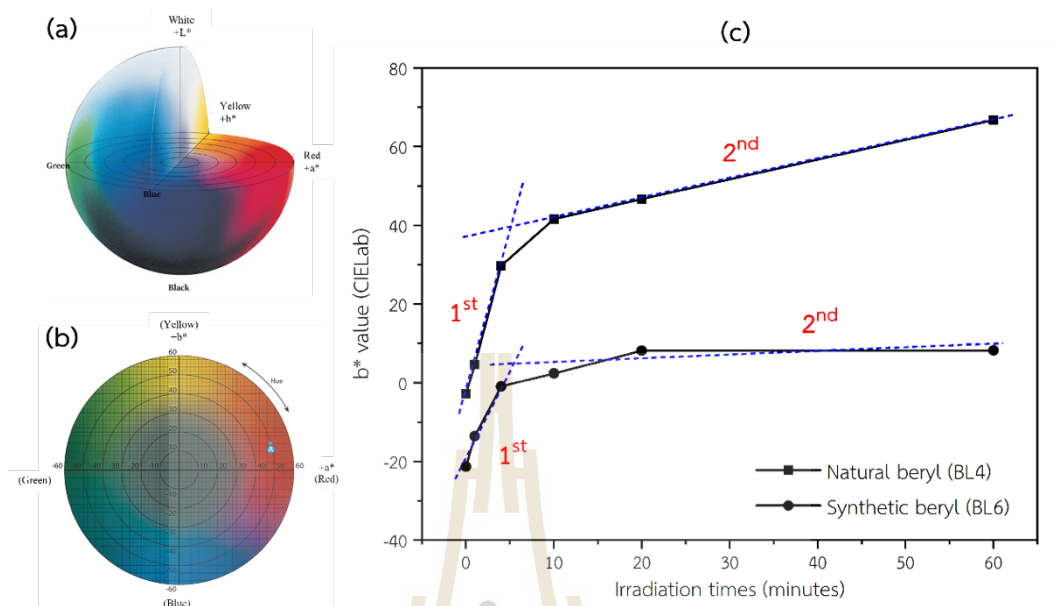


Figure 4.2 (a) and (b) show 3D and 2D diagrams of the CIE 1976 $L^*a^*b^*$ color space; (c) The b^* value of beryl coloration as a consequence of X-ray irradiation time.

The alteration of color of beryl from blue to yellow through exposure to X-ray energy is a captivating phenomenon associated with irradiating the gemstone. When beryl, particularly the blue varieties like aquamarine or blue-green types, encounters X-ray or high-energy radiation, its crystal structure undergoes a transformation, resulting in changes to its color. Numerous theories have been proposed to explain this color-changing process, such as ionization of metal ions, electron trapping, and the formation of color centers. Additionally, the intensity and duration of X-ray irradiation can influence the number and type of color centers that form in the beryl crystal lattice. Longer or more intense irradiation may lead to a deeper and more saturated color change, while shorter or milder irradiation could produce a lighter shift in color.

For instance, in the context of aquamarine beryl, exposure to irradiation can enhance the intensity of its blue color (known as Maxixe type) by generating color centers within its crystal lattice (Nassau, Prescott, and wood, 1976; Mathew *et al.*, 1998; Andersson, 2006; Adamo *et al.*, 2008). These color centers can absorb specific

wavelengths of light, resulting in the gemstone having a more vivid and appealing blue tone. However, the color change induced by X-ray irradiation in beryl is generally not permanent and may fade over time when the gemstone is exposed to heat or light (Nassau *et al.*, 1984; Robert *et al.*, 1990) Therefore, beryl gemstones subjected to X-ray irradiation are typically sold with full disclosure of the treatment to ensure transparency and informed purchasing decisions. In this study, it was observed that the color shift from blue to yellow and from yellow to intense yellow in beryl remained stable after X-ray irradiation (last checked approximately 1 year after irradiation). The stability in the yellow color of beryl might be attributed to the processes other than the formation of color centers.

4.3.2 UV-Vis and NIR absorbance spectra

The absorbance spectra typically show absorption bands at specific wavelengths, which are indicative of the presence of impurities. The pattern of absorption bands and their intensities can be used to identify the type of beryl and potentially the trace elements responsible for its color. The absorbance spectra of the beryl crystal sample were measured in the range of 300 to 2000 nm, which can be divided into UV-Vis and NIR regions.

The UV-Vis-NIR absorption spectra of both the initial beryl and X-ray irradiated beryl are depicted in Figure 4.3. The absorption profile of the initial sample displayed two relatively narrow peaks, labeled as bands **a** and **b**, which occurred at approximately 375 and 427 nm, respectively. Nearly all the beryl samples exhibited the **a** and **b** narrow absorption bands with the exception of BL5, which displayed a broader absorption spectrum. The presence of band **c** within the broader absorption range between 620-750 nm could be attributed to electronic transitions involving iron ions of varying valence, a phenomenon well-documented in previous studies (Andersson, 2019; Wang *et al.*, 2022a). Additionally, the distinct peak at 820 nm, designated as band **d**, was the result of exceptionally strong absorption, as noted in the work of Taran and Rossman (2001) and Fridrichová *et al.* (2014).

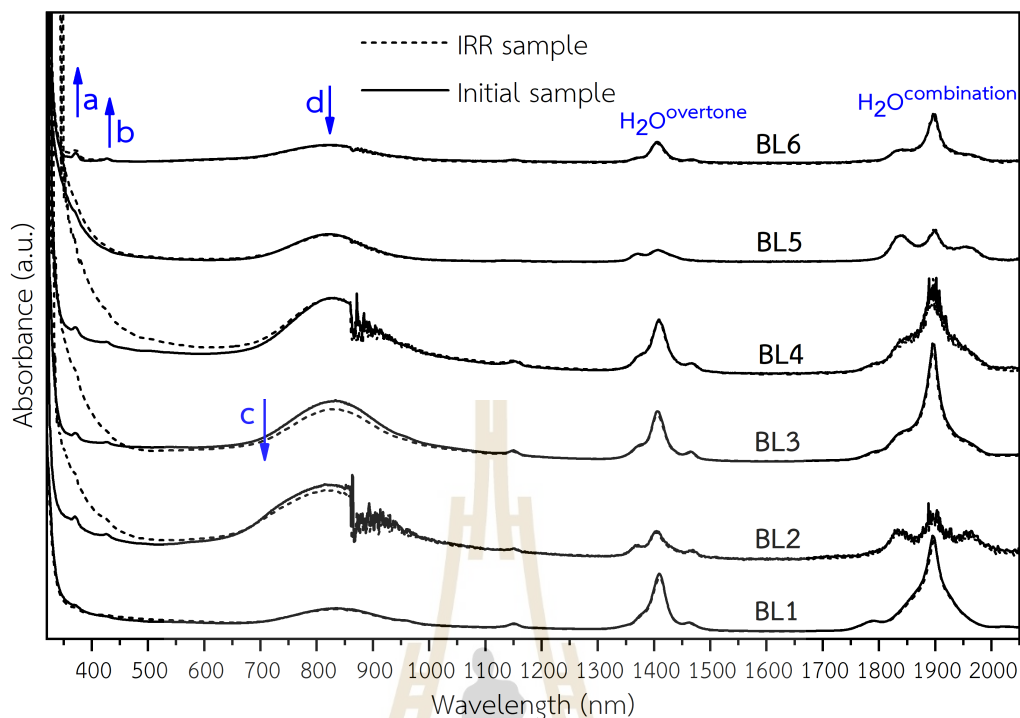


Figure 4.3 The absorbance spectrum of beryl crystal sample.

After X-ray irradiation, blue beryl including, BL2, BL3, BL4 and BL6 changed to yellowish blue. The band *d* intensities of BL2, BL3 and BL6 significantly decreased while that of BL4 slightly decreased. However, there *a* and *b* absorption bands were pronounced. The yellow beryl (BL5) changed color to intense yellow after irradiation, which resulted to the broad absorption range increasing from 300 to 500 nm. The colorless BL1 displayed a modest feature change in the UV-Vis region after X-ray irradiation, which could have been due to the sample changing to a burnt hue. The beryl crystal spectra in the NIR region of 1100 to 2000 nm is shown in Figure 4.3. The band peak range of 1370-1470 nm was due to the first and second overtones (water linked with alkalis) of the H₂O stretching vibration, while the intense band at around 1900 nm was caused by the H₂O combination mode (Taran and Vyshnevskiy, 2019). After irradiation with white beam X-ray, the absorption peak of NIR region did not show any changes in their intensity or feature. Therefore, the X-ray irradiation energy in this study had no influence on water within the beryl structure.

Several distinct electronic transitions must be considered in the analysis of the absorption bands observed in the spectrum of the beryl under investigation, including: (1) Standard electronic $d-d$ transitions occurring between electronic levels within the d -shell of $3d^N$ ions. These transitions are influenced by the Crystal Field (CFT) created by the surrounding ligands, specifically O^{2-} and OH^- . (2) Electronic Intervalence Charge-Transfer (IVCT) transitions, which involve $3d^N$ ions of varying valence located in adjacent cationic sites of the crystal structure. The strong high-energy absorption edge observed in the spectrum is primarily associated with remarkably intense absorption bands related to electronic charge-transfer transitions of the ligand-to-metal type, particularly $O^{2-} \rightarrow Fe^{3+}$ and $O^{2-} \rightarrow Fe^{2+}$ in this context. These transitions, with their peak absorption occurring in the ultraviolet (UV) region, create the lower-energy wing that extends into the visible range.

Among the absorption bands, the ones categorized under (1) have undergone the most comprehensive study, and their characteristics are relatively well-understood (Marfunin, 1979; Burns, 1993). Notable examples of such absorption bands in beryl include the spectra of green emeralds influenced by the Cr-ligand field (Atanasov *et al.*, 2022), the spectra of yellow-green-blue tones associated with iron ions (Wang *et al.*, 2022a), and the pink-purple hues generated by the presence of Mn and Cr ions (Czaja *et al.*, 2018). In iron-bearing beryl varieties, it is noteworthy that the spin-allowed ${}^5T_{2g} \rightarrow {}^5E_g$ $d-d$ transitions of Fe^{2+} ions are observed in octahedral sites, leading to a pair of bands that doubled with components around 820 nm and 950 nm (Taran and Rossman, 2001). The assignment of these bands, with their properties varying according to the polarization direction, indicates that they correspond to spin-allowed $d-d$ transitions of Fe^{2+} ions located in both the channel site (Goldman *et al.*, 1978) and the tetrahedral site (Taran *et al.*, 1989). Additionally, absorbance bands observed near 427 nm and 375 nm could be attributed to Fe^{3+}/Fe^{3+} pairs. These bands arose from electronic spin-forbidden ${}^6A_{1g} \rightarrow {}^4A_{1g}$, 4E_g and ${}^6A_{1g} \rightarrow {}^4E_g$ (4D) $d-d$ transitions of Fe^{3+} , respectively. These findings are consistent with earlier research (Taran and Rossman, 2001; Taran, Dyar, and Khomemko, 2018; Andersson, 2019; Wang *et al.*, 2022a).

The spectra of minerals and compounds containing $3d^N$ ions in varying valence states revealed the presence of IVCT bands of type (2). The striking coloration evident

in compounds and minerals containing both Fe^{2+} and Fe^{3+} ions was attributed to electronic IVCT transitions (Weyl, 1951). Extensive research encompassing a wide array of mixed-valence compounds with iron has substantiated the occurrence of electronic transitions specifically between Fe^{2+} and Fe^{3+} ions. In these transitions, Fe^{2+} functions as the electron donor, while Fe^{3+} serves as the electron acceptor, a phenomenon activated by electromagnetic or thermal excitation. A notable example of such transitions is the blue coloration observed in sapphire gemstones, a characteristic attributed to IVCT. When Fe^{2+} and Fe^{3+} ions are situated in adjacent cationic sites with common edges or faces, meaning that the neighboring coordination polyhedra have at least two ligands in common, a broad and highly intense absorption band arises. This is due to $\text{Fe}^{2+}/\text{Fe}^{3+}$ IVCT transitions, which are discernible in the optical spectra. Mineral specimens exhibit two distinctive types of IVCT bands: $\text{Fe}^{2+}/\text{Fe}^{3+} \rightarrow \text{Fe}^{3+}/\text{Fe}^{2+}$ and $\text{Fe}^{2+}/\text{Ti}^{4+} \rightarrow \text{Fe}^{3+}/\text{Ti}^{3+}$ transitions. These transitions occur when the electric field vector of polarized incident light aligns with the donor-acceptor bonds. In optically anisotropic minerals containing Fe^{2+} , Fe^{3+} , and Fe^{2+} , Ti^{4+} ions, these IVCT bands manifest strong polarization effects, yielding distinct pleochroism (Taran *et al.*, 2015).

The consistent identification of the $\text{Fe}^{2+}/\text{Fe}^{3+}$ IVCT in beryl is attributed to the presence of iron ions sharing sites within the structure. This is because iron ions can occupy various positions within the structure (Mihalynuk and Lett, 2004). Specifically, the Fe^{3+} ions located within the octahedral sites contribute to a yellow coloration, while Fe^{2+} ions in the same sites do not affect the color. The deep blue color, characteristic of aquamarine gemstones, is primarily a result of the presence of Fe^{2+} ions within specific channels. Some researchers have proposed that the variations in blue, green, and yellow hues are influenced by different ratios of Fe^{2+} and Fe^{3+} ions, as suggested by Goldman, Rossman, and Parkin in 1978. Another plausible explanation is that the IVCT process occurs between Fe^{2+} and Fe^{3+} ions located at the aluminum sites and in an interstitial octahedral position (6g), which could contribute to the blue coloration in beryl as proposed in studies, such as Platonov *et al.* (1978), Groat *et al.* (2010), Kati *et al.* (2012), and Lin *et al.* (2013). The broad and strong band in the spectra at about 690 nm was assigned to $\text{Fe}^{2+}/\text{Fe}^{3+}$ IVCT, which was generated by an absorption band in the near-infrared region at 820 nm (Isotani, Blak, and Watanabe, 2010).

The coloration of beryl is a consequence of the presence of iron ions within its structure, a phenomenon influenced by irradiation processes (Mittana *et al.*, 2002). Upon irradiation, the Fe^{2+} ions within the beryl crystal convert into Fe^{3+} ions by donating an electron to an electron trap. This transformation was associated with a noticeable decrease in the absorption peak at 820 nm (Ittipongse *et al.*, 2017). The yellow coloration of beryl is linked to charge transfer mechanisms involving Fe^{3+} ions substituting for Al^{3+} ions within the octahedral sites, which are surrounded by oxygen ions (Andersson, 2013). Furthermore, blue beryl initially exhibited narrow absorption bands at 375 and 427 nm. These bands appeared to transition into broader bands after exposure to X-ray irradiation. This change may be indicative of a process where Fe^{3+} ions aggregate into exchange-coupled pairs, specifically $\text{Fe}^{3+}\text{-Fe}^{3+}$, which becomes more complete and resembles the initial state of natural yellow beryl (Figure 4.3). This concept is in line with the observations made by Taran *et al.* in 2015.

Table 4.5 The electron transition and band energy of Fe ions.

Band	Electronic transition	Energy (nm)	Energy (eV)
a	$\text{Fe}^{3+} ({}^6\text{A}_{1g} \rightarrow {}^4\text{E}_g ({}^4\text{D}))$	375	3.30
b	$\text{Fe}^{3+} ({}^6\text{A}_{1g} \rightarrow {}^4\text{A}_{1g}, {}^4\text{E}_g)$	427	2.90
c	$\text{Fe}^{3+} \leftrightarrow \text{Fe}^{2+}$ IVCT	690	1.80
d	$\text{Fe}^{2+} ({}^5\text{T}_{2g} \rightarrow {}^5\text{E}_g)$	820	1.51

The band gap energy of pure beryl, which crystallizes in the hexagonal P6/mcc space group, was computed and reported at 5.32 eV in Material project mp-6030 (Jain *et al.*, 2013). The different colors of beryl are due to the presence of different trace elements or impurities in the crystal lattice. The blue and yellow colors of beryl are considered to be caused by trace amounts of iron. The specific band gap energy of a beryl gemstone depends on its chemical composition, crystal structure, and the presence of impurities. The presence of Fe ions was found to influence the band energy of beryl structure, which is related to the color observed, as shown in detail in Table 4.5. The introduction of Fe^{3+} ions in the octahedral sites of beryl structure led to the yellow color in beryl, with band energy ranging from 2.90 eV to

3.30 eV. Octahedral Fe^{2+} ions, which caused crystal field effects at 820 nm absorption, did not contribute to visible coloration (Andersson, 2019). The correlation between the intensity of the 690 nm absorption and Fe^{2+} concentration supported the involvement of octahedral Fe^{2+} ions in the blue coloration. The proposed theory suggests that the blue coloration arises due to IVCT between Fe^{2+} and Fe^{3+} ions, substituting for Al^{3+} ions and occupying the 6g crystallographic site along the c-axis direction (Plantonov *et al.*, 1978; Goldman *et al.*, 1978). The IVCT band energy at 690 nm was determined to be 1.80 eV, while the band energy of Fe^{2+} at 820 nm was 1.51 eV.

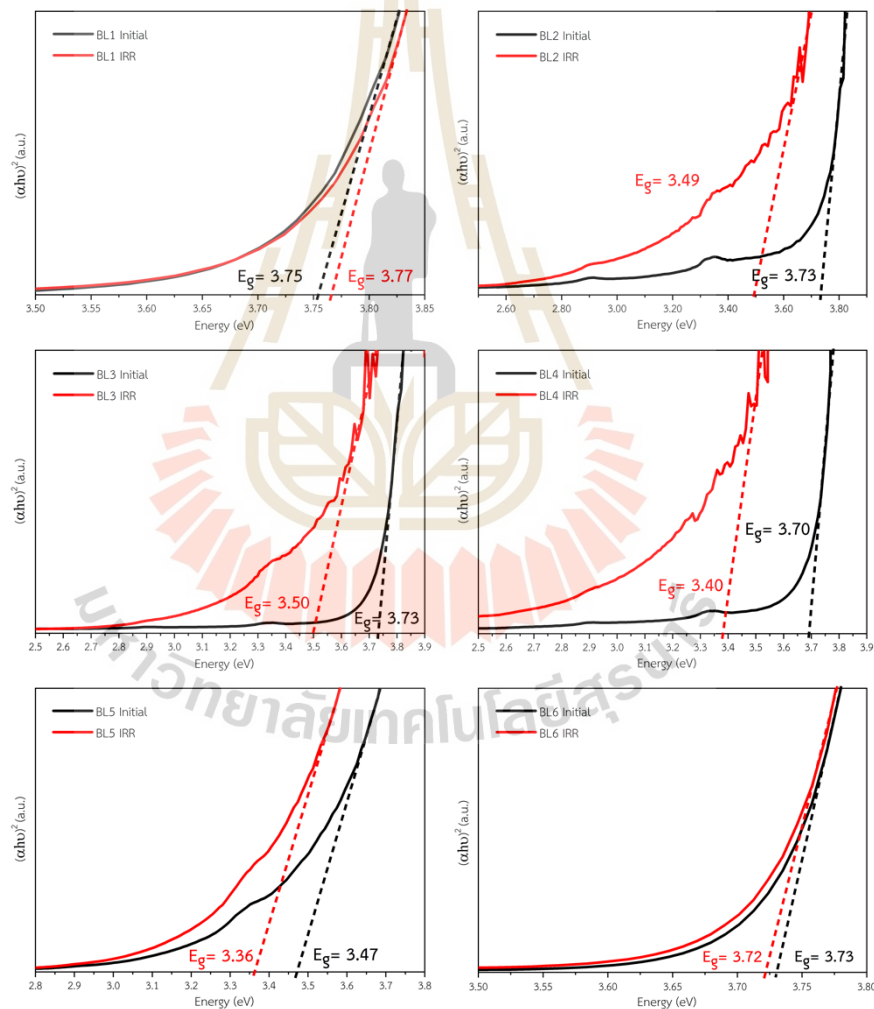


Figure 4.4 Tauc plot for direct bandgap of beryl crystal sample, with black solid line representing initial beryls and red solid line representing IRR beryls. The bandgap is defined as the intercept of the dotted line with the horizontal axis.

Beryl is a mineral composed of beryllium aluminosilicate and is characterized as a direct band gap material. In order to elucidate the relationship between the absorption factor and band gap energy, the Tauc plot method and the Kubelka-Munk equation were employed, as discussed by Chen, Wang, and Shu in 2024. To calculate the band gap energy of beryl samples, Tauc's equation was utilized, expressed as $[(\alpha hv)^{1/n} = A(hv - E_g)]$. In this equation, 'hv' represents the energy of incoming photons, 'A' denotes a constant, and 'n' is the exponent. The specific value of 'n' depends on the nature of the electronic transition governing the absorption, taking on values of 1/2 or 2 depending on whether the transition is direct or indirect. It is worth noting that the absorbance spectra of different colors of beryl samples exhibited variability and manifested distinct changes following X-ray irradiation. The alterations in the absorption spectra corresponded to fluctuations in the band gap energy, as illustrated in Figure 4.4.

In summary, this study identified distinct color zones in beryl, irrespective of plane polarization considerations, which can be categorized as follows: (1) yellow beryl was found to have a band gap energy similar to that of Fe^{3+} at 3.30 eV, (2) blue beryl exhibited a band gap energy ranging from 3.70 to 3.75 eV, (3) colorless beryl demonstrated a conclusive band gap energy exceeding 3.75 eV, resulting in its lack of coloration. According to Chen, Wang, and Shu (2024), the band gap energy of both blue and colorless beryls were comparable to the band gap energy of light blue beryl (3.76) and intense blue beryl (3.64), as determined by the Kubelka-Munk equation.

Upon exposure to X-ray irradiation, the color of beryl shifted towards a hue closely related to that of yellow beryl. This change was likely due to the conversion of Fe^{2+} electrons to Fe^{3+} , which resulted in reduced electronic intensity. It is important to note that although this study provides support for this phenomenon, the findings are based on a limited sample set. Except for colorless beryl (BL1), the exposure of blue beryl to X-ray could induce the reduction of electrons from Fe^{2+} to Fe^{3+} . This led to an increased electronic intensity of Fe^{3+} post-irradiation and a decreased band gap energy comparable to the band energy of Fe^{3+} .

4.4 Absorption energy, oxidation state, and coordination number

4.4.1 X-ray Absorption Near Edge Spectrometer (XANES)

XANES was used to investigate the chemical environments and oxidation states of specific elements in beryl samples. XANES is sensitive to the chemical environment of the element, including its oxidation state and arrangement. Absorption edge shifts are caused by different oxidation states. The shape of the spectrum represents the local atomic structure, and different coordination geometries give distinct properties. Beryl XANES spectra were studied by comparing features, positions, and patterns in XANES spectra to references, revealing electrical and structural properties. In this study, XANES was used to examine Fe ion states and the surroundings in the crystal structure, offering insights into the origins of colors.

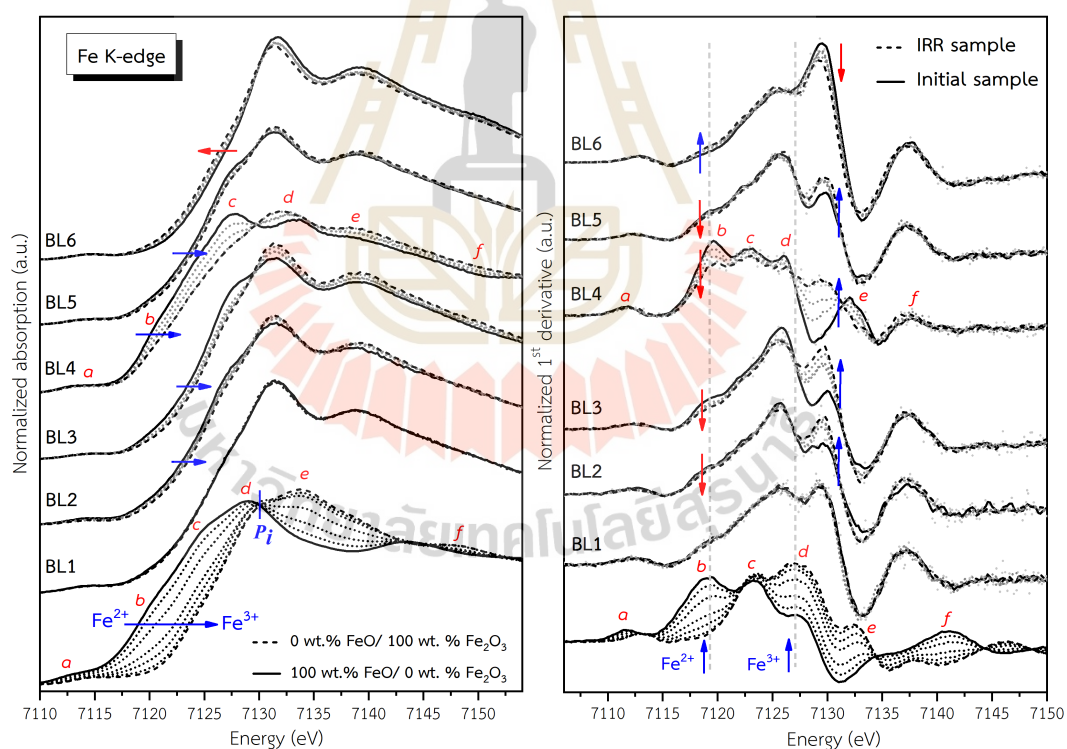


Figure 4.5 XANES spectra of irradiated beryl powder samples (0, 0.5, 1, 4, 10 mins) compared to $\text{Fe}^{2+}/\text{Fe}^{3+}$ mixture ratios of 0, 10, 25, 50, 75, 90, and 100 wt.% Fe^{3+} .

Fe-K-edge XANES were used to investigate the initial beryl powder. The XANES characteristics of initial beryl could be divided into three feature groups. The first group consisted of BL1 and synthetic BL6, which showed flat shoulders **b** and **c**. The second group consisted of BL2, BL3, and BL5, which displayed the shoulder **b** and **c** characteristics. The third group was BL4, which had the highest levels of shoulders **b** and **c** in this research, particularly shoulder **b** position.

Powdered beryl samples underwent X-ray irradiation for durations of 0.5, 1, 4, and 10 minutes. The XANES characteristics of most beryl powder samples altered post-irradiation, with the exception of slight changes in BL1 attributed to electronic data accumulation. Notably, BL6 exhibited a distinctive trend compared to other groups. Following X-ray irradiation, both Groups 2 and 3 beryl samples displayed similar modifications in features, with flattening of shoulders **b** and **c**, and particularly BL4 sample exhibiting significant changes with complex features in **d** and **e**. The altered features observed in BL4 resulted from $\text{Fe}^{2+}/\text{Fe}^{3+}$ wt.% ratio changes. A depiction of the changes in irradiated beryl features are shown in Figure 4.5.

The alteration trend of **b**, **c**, and **d** features in response to the $\text{Fe}^{2+}/\text{Fe}^{3+}$ ratio was indicated by the 1st derivative feature. This trend corresponded to Fe^{2+} , the mixture of $\text{Fe}^{2+}/\text{Fe}^{3+}$, and Fe^{3+} features, respectively. The suggestion that the beryl samples represented a mixture of Fe^{2+} and Fe^{3+} could be explained by comparing the oxidation feature of the $\text{Fe}^{2+}/\text{Fe}^{3+}$ ratio in the samples (Bunnag *et al.*, 2020). Following X-ray irradiation, a decrease in Fe^{2+} and an increase in the complex **d** and **e** feature (associated with Fe^{3+}) were observed. The decrease in Fe^{2+} in the XANES feature implicated the alteration of octahedral Fe^{2+} substitution and IVCT between Fe^{2+} and Fe^{3+} ions within the beryl structure. This phenomenon supported the transformation from a blue to yellow color, including the intense yellow in the yellow beryl. The synthetic sample exhibited a different feature trend due to its higher content of Fe^{3+} ions, possibly as free atoms. After X-ray irradiation, these features were modified to suitably occupy beryl lattice sites, leading to a reduction in the Fe^{3+} feature. The colorless beryl did not show a change in color or XANES features after X-ray irradiation, corresponding to the same trend in UV-vis absorption spectra and band gaps.

4.4.2 Pre-edge feature and centroids position

The pre-edge peak, a feature obtained from the XANES spectra, illustrates a transition resembling the characteristics of an $s-d$ like transition. Despite its inherent dipole-forbidden nature, this transition is somewhat permitted through the combination of the d -states associated with the transition metal and the p -states of the surrounding oxygen atoms. Consequently, the pre-edge peak energy position and its strength are profoundly influenced by the geometric arrangement around the element Fe, as well as the average oxidation state of Fe (Calas and Petiau, 1983a, 1983b; Brown *et al.*, 1995).

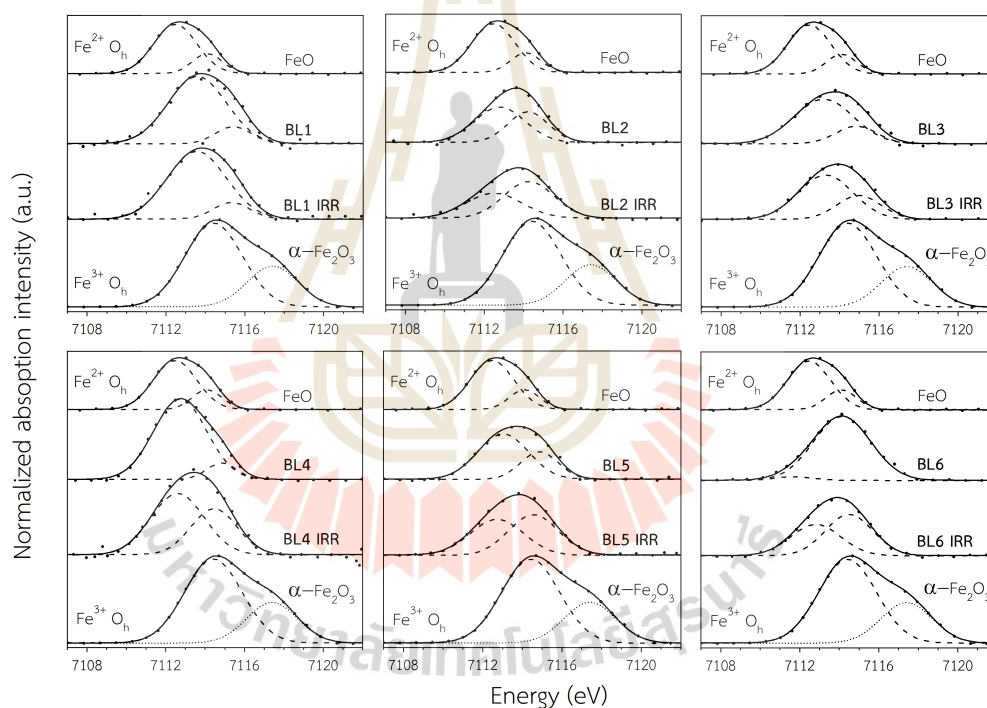


Figure 4.6 Background subtracted pre-edge peaks of the beryl sample (dotted lines) along with the Gaussian component used in the fitting procedures (dash lines and short dotted lines) and Gaussian sums (solid lines).

Notably, a meticulous assessment of the central energy of the pre-edge peak and its integrated intensity, coupled with a comparative analysis against Fe model compounds, can yield quantitative insights into both the oxidation state of Fe and the coordination environment (Wilke *et al.*, 2001; Farges, 2001; Giuli *et al.*, 2002a, 2003).

The intensity of this peak is nearly negligible in case of a regular octahedral symmetry (O_h) around the absorbing element, whereas it attains its maximum magnitude in instances of tetrahedral coordination (T_d). The subtracted pre-edge peaks after accounting for the background are displayed in Figures 4.6, along with the components following a Gaussian profile and their cumulative sums.

Table 4.6 XANES pre-edge fitting resulted of powder beryl samples.

Sample	Position (eV)	Area	HWHM	Total area	Weight area (%)	Centroid (eV)	R ²
FeO	7112.47	0.0580	1.29	0.0743	78.06	7112.83	0.9991
	7114.10	0.0163	0.90		21.94		
Fe ₂ O ₃	7114.42	0.1323	1.73	0.1323	100.00	7114.42	0.9995
	7117.41*	0.0565	1.52				
BL1	7113.59	0.1068	1.74	0.1236	86.41	7113.84	0.9824
	7115.42	0.0168	1.07		13.59		
BL1-IRR	7113.56	0.1087	1.77	0.1253	86.75	7113.81	0.9864
	7115.44	0.0166	1.09		13.25		
BL2	7112.81	0.0503	1.51	0.0824	61.04	7113.37	0.9874
	7114.25	0.0321	1.18		38.96		
BL2-IRR	7112.50	0.0383	1.68	0.0885	43.28	7113.50	0.9936
	7114.27	0.0502	1.50		56.72		
BL3	7113.08	0.0654	1.74	0.0920	71.09	7113.55	0.9913
	7114.72	0.0266	1.31		28.91		
BL3-IRR	7113.06	0.0541	1.56	0.0950	56.95	7113.81	0.9962
	7114.79	0.0409	1.39		43.05		
BL4	7112.73	0.1158	1.58	0.1293	89.56	7112.95	0.9939
	7114.84	0.0135	0.90		10.44		
BL4-IRR	7112.60	0.0894	1.59	0.1472	60.73	7113.33	0.9890
	7114.45	0.0578	1.38		39.27		
BL5	7113.02	0.0619	1.50	0.0903	68.55	7113.60	0.9916
	7114.86	0.0284	1.12		31.45		
BL5-IRR	7112.72	0.0525	1.59	0.1075	48.84	7113.66	0.9954
	7114.56	0.0550	1.48		51.16		
BL6	7111.69	0.0041	1.20	0.1036	3.96	7114.05	0.9967
	7114.15	0.0995	1.70		96.04		
BL6-IRR	7112.81	0.0429	1.49	0.0964	44.50	7113.75	0.9978
	7114.50	0.0535	1.41		55.50		

* Peak centered above 7116.08 eV, being non-local transitions observed in spectrum of Fe³⁺, which are omitted in the analysis of the chemical state of Fe.

The centroid energies and integrated intensity values are detailed in Table 4.6. Each pre-edge peak of beryl can be accurately described by two Gaussian constituent elements, with energies approximately around 7112.51 to 7114.44 eV. These energy values correspond well with those found in Fe model compounds. Two Gaussian components align with contributions from Fe^{2+} and Fe^{3+} mixture, while the energy results from combined Gaussian of both divalent and trivalent Fe.

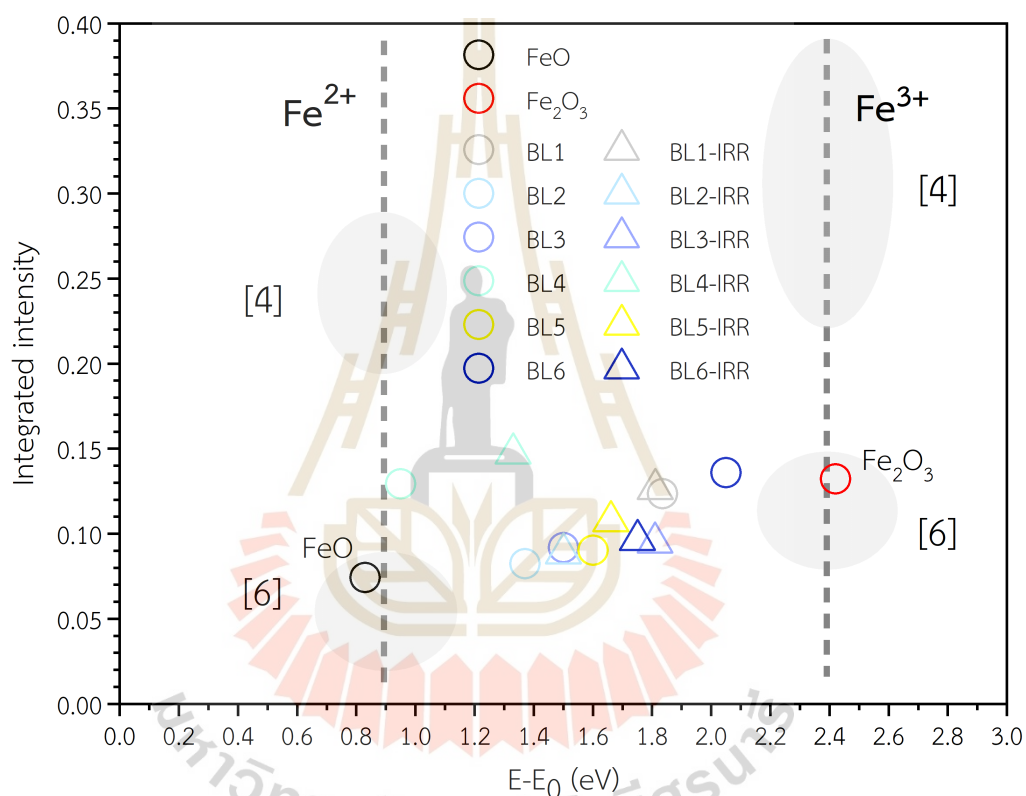


Figure 4.7 Relationship between integrated pre-edge intensity and pre-edge centroid energy locations of beryl samples and oxide standards. The open circles relate to the reference research, which gave typical characteristics for four kinds of Fe species in Wilke *et al.* (2001) and Giuli *et al.* (2011). [4] represents a 4-fold coordinated Fe and [6] represents a 6-fold coordinated Fe.

The proportionate significance of either divalent or trivalent Fe influences the respective components, inducing a shift in the energy center of the pre-edge peak. Figure 4.7 presents a graphical representation of the integrated intensity of the pre-

edge peaks in relation to their centroid energies. This figure also includes the data from analyzed Fe standard (FeO and Fe₂O₃) and Fe model compounds (Wilke *et al.*, 2001; Giuli *et al.*, 2011). The depicted plotted energies begin at 0, which corresponds to the initial peak in the first derivative of the metallic Fe spectrum. All divalent Fe compounds in the standard Fe model were plotted at energies close to 0.9 eV above the metallic Fe edge (0 eV), whereas trivalent Fe compounds were plotted at energies close to 2.4 eV. The intensity of the pre-edge peaks of the model compounds changed with the Fe coordination geometry at constant energy. The shaded circle in Figure 4.7 refers to the range of coordination numbers in Fe compounds.

The fitting results of Fe standards in this study were considered reliable because the results indicated a similar trend to the reference model compound. The centroid calculation of FeO and Fe₂O₃ were 7112.83 and 7114.42 eV, respectively. The iron oxides standard had six coordinated oxygen and octahedral symmetry structure. The data for the beryls in each group plot followed a trend that extended from the region of [6] Fe²⁺ compounds to higher energies and intensities of [6] Fe³⁺ compounds. The centroid results provided by the beryl samples were [6] Fe²⁺ and [6] Fe³⁺ compound mixture. BL4 beryl had a greater intensity between the [6] Fe²⁺ and [4] Fe²⁺ mixture and centroid energy was near to the divalent model compound, however, the centroid energy changed to [6] Fe³⁺ compound after X-ray irradiation. While the BL6 synthetic beryl initial sample had the greatest centroid energy, the centroid intensity shift was comparable with other beryl groups after X-ray irradiation. The difference in the centroid of BL4 could be attributed to the geometry and coordination corresponding to the XANES after X-ray irradiation where BL4 still contained powerful divalent Fe in both fourfold and sixfold coordination. This could imply that the Fe ions can occupy other sites in the beryl structure in addition to the sixfold coordination (Mittani *et al.*, 2002).

4.4.3 Electron Paramagnetic Resonance (EPR)

EPR is a spectroscopic method used for analyzing materials with unpaired electrons, like paramagnetic substances. Beryl, a mineral containing various impurities and transition metal ions, exhibits diverse color variations attributed to trace elements

or impurities within its crystal structure. The introduction of unpaired electrons occurs when iron ions within beryl adopt a particular oxidation state, rendering them paramagnetic. EPR is employed to investigate the electronic characteristics of these paramagnetic iron ions. Iron ions can substitute other metal ions within the beryl lattice, leading to the emergence of unpaired electrons. Applying an external magnetic field to the beryl gemstone hosting paramagnetic iron ions induces energy level shifts in the unpaired electrons, resulting in microwave radiation absorption. The frequency of the absorbed radiation hinges on the strength of the magnetic field and the properties of the paramagnetic species, surrounding the local iron ion environment. The interplay between iron ions and adjacent atoms influences the EPR signal, generating distinct EPR spectra under different coordination conditions. EPR analysis can also uncover defects or impurities within the crystal structure, which can influence the beryl characteristics and coloration.

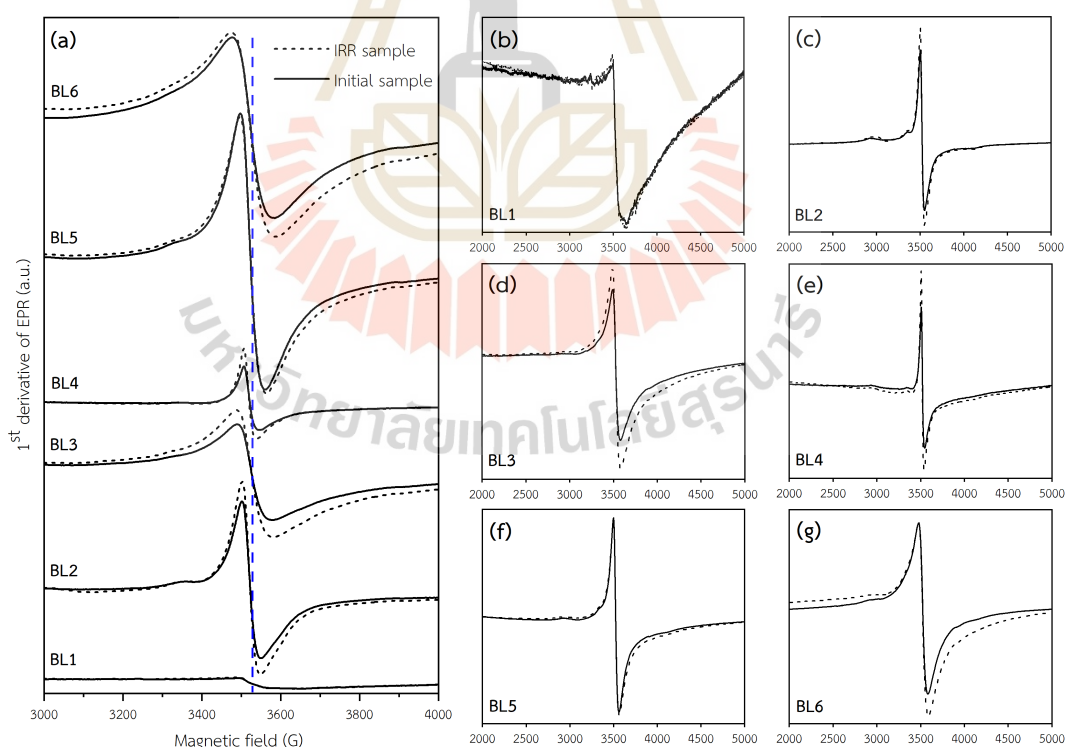


Figure 4.8 1st functional derivative EPR spectra of beryl powder, (a) comparison of signal intensities, (b)-(g) comparison of EPR feature in normalized intensity.

Figure 4.8 depicts the EPR spectra of initial beryl powder and X-ray irradiated beryl. The most significant component of the EPR signal was resonance absorption, which corresponded to the value of $g \approx 2$ (blue dashed line). The EPR signals of different beryl samples exhibited varying intensities, with the difference in intensity levels ranging from lower to higher, designated as BL1, BL4, BL3, BL2, BL6, and BL5, respectively. The intensity of the EPR signal corresponded to the quantity of paramagnetic content within the beryl structure. Typically, the signal intensity was influenced by the presence of Fe content in the beryl structure. For instance, colorless beryl (BL1) displayed the lowest EPR intensity, correlating with its lower Fe content, as indicated in the EPMA Table 4.1. A point of interest pertained to BL3, which exhibited an intense blue hue but demonstrated lower EPR signal intensity compared to BL2. Conversely, the yellow-colored beryl (BL5) displayed higher EPR intensity than the blue beryl BL3 and synthetic BL6, despite having lower Fe ion content. The relatively low signal of blue beryl might be attributed to its elevated Fe^{2+} content, as posited by previous studies (Andersson, 2019; Wang *et al.*, 2022b). Fe^{2+} ions predominantly occupy the same position, often leading to diamagnetic compounds. However, in the presence of certain ligands, Fe^{2+} complexes can become diamagnetic due to a low-spin configuration. Strong-field ligands in an octahedral configuration induce a low-spin situation, where all electrons are paired, resulting in diamagnetism. Conversely, Fe^{3+} ions are paramagnetic due to the necessity of unpaired electrons in their orbitals, leading to a strong EPR signal.

Upon irradiation with X-rays, the EPR signal intensity of nearly all beryl samples increased, with the exception of BL1, which exhibited a slight change in intensity. Previous research by Andersson (2013) elucidated the significance of the $g \approx 2$ value, corresponding to Fe^{3+} in octahedral and center site symmetry (Groat *et al.*, 2010). In contrast, this study identified a weak rhombic Fe^{3+} center at $g \approx 4.28$, with a signal relatively unaffected by the treatment process (Lin *et al.*, 2013).

Distinctive EPR features arise from variations in the absolute value of $|D|$ or the magnitude of zero-field splitting, where $|D|$ characterizes energy level splitting in paramagnetic species due to the interaction between unpaired electron spins and the local environment (Klencsár and Köntös, 2018). Contributions of high- $|D|$ and low- $|D|$

components to the theoretical Fe^{3+} EPR signal delineate energy level splitting caused by strong and weak interactions with the local environment, respectively. EPR characteristics of powder samples BL2, BL3, BL4, BL5, and BL6 revealed an isotropy axis, indicating symmetry in the 1st derivative EPR signal and a tendency toward high- $|D|$ contributions, evident in the pronounced and narrow peaks illustrated in Figure 4.9 (c)-(g). However, BL1 diverged from other beryl samples, showcasing an anisotropy axis feature with $g_x = g_y > g_z$ (Petasis and Hendrich, 2015). The anisotropy axis observed in Fe^{3+} within the BL1 structure might be attributed to the XRD pattern, where the c lattice is longer than the a lattice, as presented in Table 4.2. Notably, this study did not investigate the EPR signal of beryl crystal samples; future exploration of beryl crystal may enhance comprehension of the structural and electronic attributes of Fe^{3+} ions in beryl coloration induced by X-ray irradiation.

4.4.4 Extended X-ray Absorption Fine Structure (EXAFS)

The EXAFS technique holds considerable efficacy in X-ray spectroscopy, functioning as a means to investigate the intricate atomic milieu in proximity to a designated element within a material. The present study employed Fe K-edge EXAFS to concentrate on the meticulous scrutiny of the local structural characteristics encompassing iron (Fe) atoms within a beryl sample. The magnitude and patterns of oscillations in the intensity of X-rays absorbed within the EXAFS spectral region are subject to meticulous analysis, yielding insights into the interatomic distances, bond lengths connecting iron with adjacent atoms, and the coordination numbers prevalent in the system. Interpretation of the EXAFS spectra typically entail subjecting data to Fourier transformation, facilitating the segregation of distinct contributions. Subsequently, a theoretical model is harnessed to effectively conform the experimental data, thereby eliciting quantifiable insights pertaining to the indigenous atomic configuration. This methodological approach proves instrumental in comprehending the precise geometrical arrangement of neighboring atoms proximate to iron ions embedded within the crystal lattice of the beryl sample.

The EXAFS computation of the beryl Fe-k edge began with an examination of the Fe_2O_3 standard, which has a known chemical structure and had simultaneous

measurement circumstances on the same parameters. The Fe_2O_3 standard EXAFS spectra was simulated using the $\text{Fe}_2\text{O}_3_{\text{mp-19770}}$ model, which crystallizes in the trigonal $\bar{R}3c$ space group. Fe^{3+} is bonded to six equivalent O^{2-} atoms to form a mixture of distorted face, corner, and edge-sharing FeO_6 octahedra. The corner-sharing octahedral tilt angles range from 48-61°. There are three shorter (1.97 Å) and three longer (2.12 Å) Fe-O bond lengths. O^{2-} is bonded to four equivalent Fe^{3+} atoms to form a mixture of distorted corner and edge-sharing OFe_4 trigonal pyramids (Jain *et al.*, 2013). Figure 4.9(a) displays the chemical structure and single scattering path of the Fe_2O_3 model.

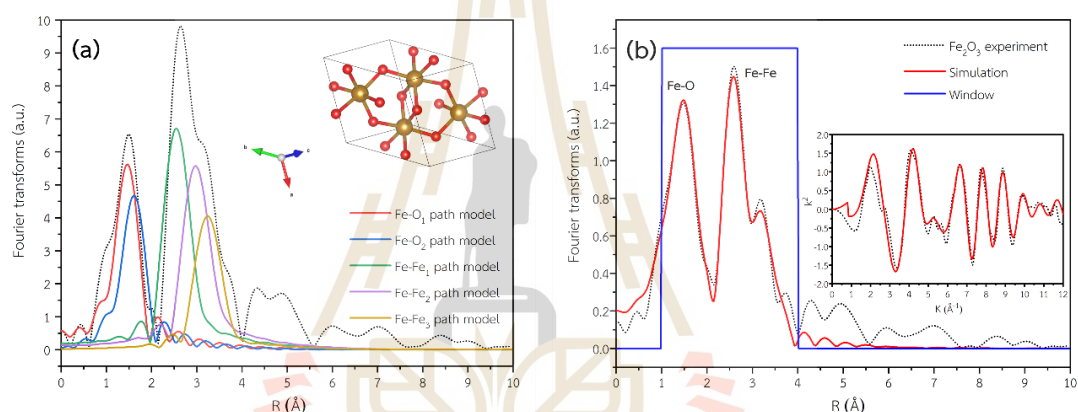


Figure 4.9 Chemical structure and single scattering path of the Fe_2O_3 model (a), Fourier transforms of $k^2 \cdot \chi(k)$ spectra and R-space curve and fits for Fe K-edge EXAFS spectra from the Fe_2O_3 experiment (b).

Table 4.7 Local environments of Fe from R space EXAFS fitting of Fe_2O_3 standard.

Path no.	Path	CN	S^2	σ^2 (Å ²)	R (Å)	E0 shift	R-factor
1	Fe-O ₁	3	0.9480	0.00662	1.91 (0.02)		
2	Fe-O ₂	3	0.9480	0.00662	2.06 (0.02)		
3	Fe-Fe ₁	3	0.9600	0.00460	2.93 (0.01)	2.495	0.00976
4	Fe-Fe ₂	3	0.9500	0.00300	3.37 (0.02)		
5	Fe-Fe ₃	6	0.9500	0.00990	3.66 (0.02)		

The Fourier transforms of $k^2 \cdot \chi(k)$ spectra were performed over the k ranges of 3.0-10.0 \AA^{-1} and R-space fitting windows of 1.0-4.0 \AA (Figure 4.9(b)). Table 4.7 shows an excellent EXAFS fitting result for Fe_2O_3 experiment when compared to the mp-19770 structure model including outer Fe-O and Fe-Fe paths. The SO^2 levels containing Fe_2O_3 varied between 0.9480 and 0.9500 (average was $0.9512 \approx 0.95$). This SO^2 value was utilized as the constant value for the beryl sample EXAFS analysis.

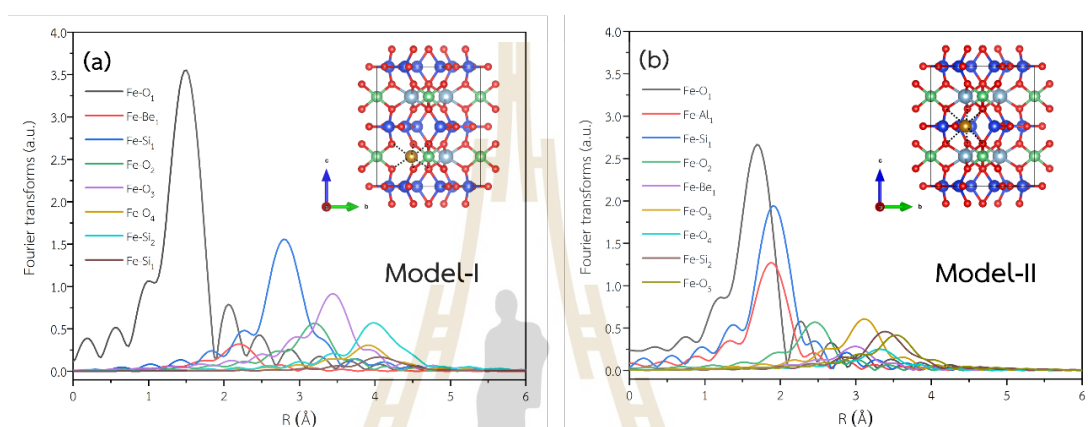


Figure 4.10 Chemical structure and simulated single scattering path of Model-I (a), Model-II (b).

The Fe K -edge EXAFS data of beryl powder sample was fitted with two models, using theoretical standards from IFEFFIT by ARTEMIS program (Ravel and Newville, 2005). The beryl crystallography data, mp-6030, identification in $P6/mcc$ space group was used for EXAFS model fitting. The hexagonal crystal system of beryl model is a lattice parameter including, $a=9.303 \text{ \AA}$, $b=9.303 \text{ \AA}$ and $c= 9.278 \text{ \AA}$ (Jain *et al.*, 2013 project, 2022). Two models were associated with the Fe ions in the beryl structure. For Model-I, the Fe ion was substituted at the Al site, which assumed the local symmetry of the octahedral from the six nearest oxygen atoms. The Fe ion was positioned at a 6g interstitial position from the six adjacent oxygen atoms in Model-II (Lin *et al.*, 2013). Figure 4.10 demonstrates the simulated single scattering path of Models I and II using the IFEFFIT computation by the ARTEMIS software.

The EXAFS spectra of the beryl sample in R-space underwent noticeable changes following exposure to X-ray irradiation. The characteristics of the first peak, BL2 to BL5 showed increased intensity, whereas BL6 exhibited a decrease in intensity.

However, the colorless beryl (BL1) exhibited only slight changes. Following X-ray irradiation, the R-space of the EXAFS spectra displayed changing trends. The first magnitude peak showed increased intensity for BL4 and decreased intensity for BL6 in the initial peak, particularly when compared to other beryl samples (refer to Figure 4.11(b)).

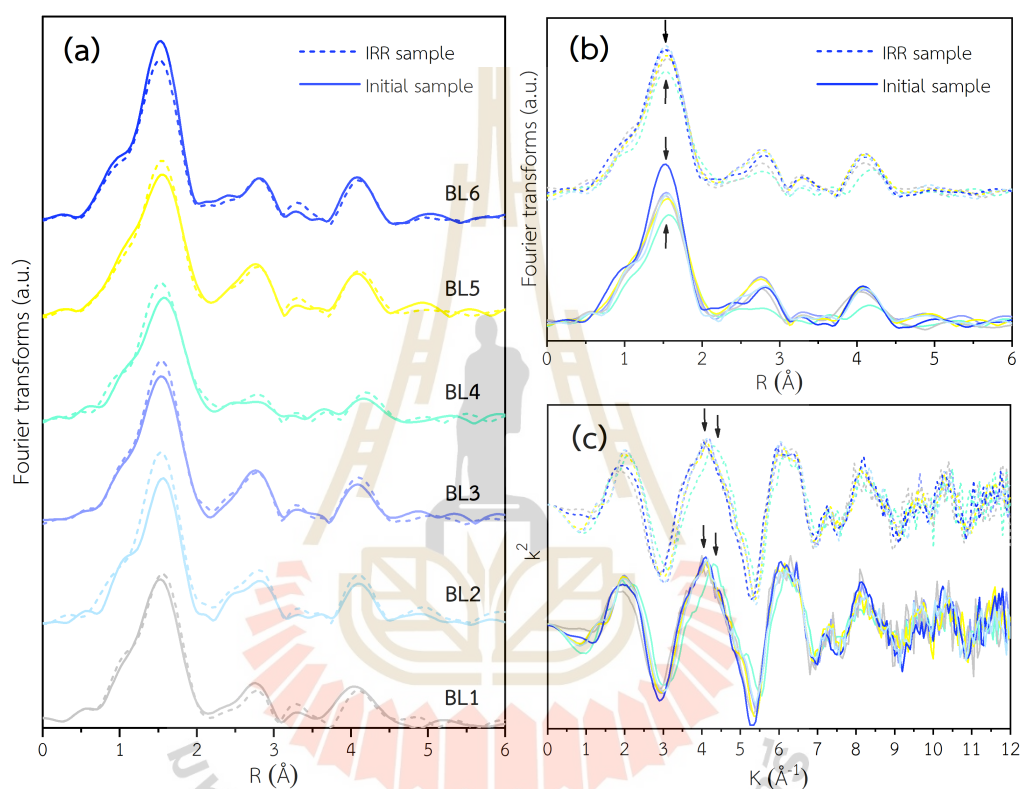


Figure 4.11 The Fe K-edge EXAFS spectra of powder beryl samples were calculated using theoretical standards from IFEFFIT using the ARTEMIS software to compare initial and after X-ray irradiation spectra in Fourier transforms R-spec (a and b) and $k^2 \cdot \chi(k)$ of k-space (c).

The Fourier transforms of k-space in Figure 4.11(c) revealed a shift in the characteristics of BL4, which differed from other beryl samples before and after X-ray irradiation, corresponding to the lower intensity of the first peak in R-space. This first peak in R-space is associated with the positioning and coordination of Fe ions in the beryl structure. The investigation of the first path scattering focused on the initial Fe-

O scattering path of Model-I. EXAFS analysis were conducted within the k-range of 3.0-11.0 \AA^{-1} and R-space of 1.0-2.0 \AA . Table 4.8 summarizes the calculation results of the coordination of Fe ion sites in beryl structures.

Table 4.8 The first scattering path of oxygen nearest to Fe ions in beryl structure was fitted using Model-I of EXAFS R-space.

Sample	σ^2 (\AA^2)	E0 shift	R (\AA)	R-factor	CN
BL1	0.004	-4.36	1.99 (0.03)	0.0322	4.96 (1.95)
BL1-IRR	0.003	-2.38	2.00 (0.03)	0.0296	4.96 (1.85)
BL2	0.004	-0.65	2.00 (0.02)	0.0128	4.50 (1.03)
BL2-IRR	0.004	-1.16	1.99 (0.02)	0.0089	5.13 (1.02)
BL3	0.004	-1.86	2.00 (0.03)	0.0170	4.89 (1.30)
BL3-IRR	0.004	-0.50	2.00 (0.02)	0.0096	5.12 (1.06)
BL4	0.005	4.23	2.01 (0.03)	0.0215	3.92 (1.14)
BL4-IRR	0.004	2.74	2.00 (0.03)	0.0186	4.22 (1.11)
BL5	0.004	0.56	2.01 (0.05)	0.0290	4.56 (1.55)
BL5-IRR	0.004	-0.69	2.00 (0.02)	0.0141	4.77 (1.20)
BL6	0.002	-3.59	1.99 (0.02)	0.0120	5.14 (1.27)
BL6-IRR	0.003	-4.48	1.99 (0.02)	0.0119	5.07 (1.26)

The oxygen atoms nearest to the iron ions exhibited coordination with varying coordination numbers and a significant standard deviation, theoretically allowing for an inaccuracy of approximately 20-30% or about 1 CN. The predominant trend in Fe-O coordination was observed to be between 4 and 5 CN, with BL4 displaying the lowest CN, while other beryl samples exhibited higher values around 4.5 CN, estimated to be approximately 5 CN. Following irradiation, there was an overall trend toward higher CN in the coordination of oxygen around iron ions, except for the synthetic BL6 sample, which showed a slight decrease in CN. The coordination numbers were influenced by the magnitudes of intensities, such as the peak intensity (I) in the R-space beryl EXAFS spectra. BL4 consistently displayed the lowest CN of Fe coordination, leading to pre-edge fitting. Even after X-ray irradiation, BL4 continued to exhibit coordination numbers ranging from 4 to 6 CN, possibly due to the average Fe

ions occupying both tetrahedral and octahedral sites in the beryl structure. The diverse coordination of iron ions in the beryl structure may contribute to asymmetry, as observed in BL1, and is linked to the results obtained from EPR and XRD analyses. Notably, BL6, which had the highest iron content of 1.568 wt.% (determined by EPMA), displayed an opposite trend in CN changes following X-ray irradiation, possibly attributable to Fe ions occupying unstable sites.

The EXAFS simulation spectra were generated with k ranges of 3.0-11.0 \AA^{-1} , R -space of 1.0-5.5 \AA for Model-I and around 1.0-2.9 \AA for Model-II. The Fe ion substituting Al site assumed the local symmetry of the octahedral from the six nearest oxygen atoms for Model-I fitting. The identical Fe-O₁ was the first shell scattering paths from the six nearest neighboring oxygen atoms and the second nearest neighboring paths from three Fe-Be₁. Other scattering paths included six silicon atoms (Fe-Si₁), six oxygen atoms (Fe-O₂), twelve oxygen atoms, (Fe-O₃), six oxygen atoms (Fe-O₄), six silicon atoms (Fe-Si₂), two aluminum atoms (Fe-Al) distances.

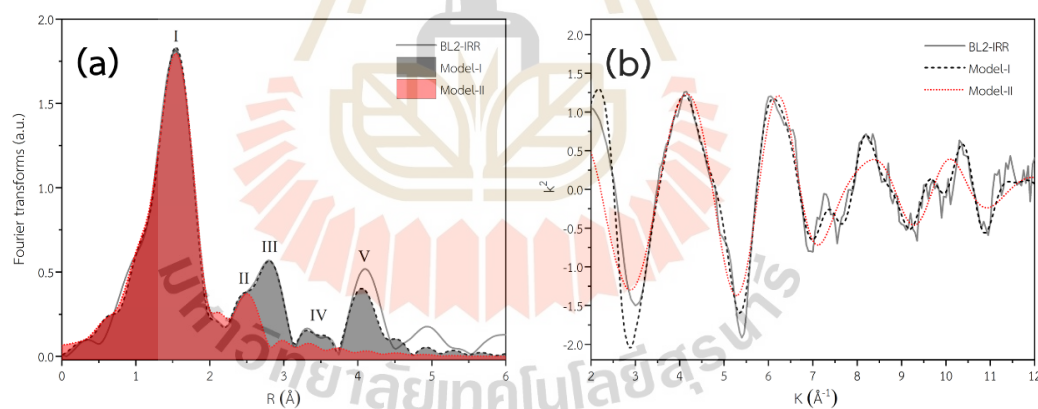


Figure 4.12 The IFEFFIT calculation and comparison of beryl experiment spectra and Models I and II simulation spectra in R -space curve and fits for (a), Fourier transforms $k^2 \cdot \chi(k)$ of k -pace (b) for determining the local structure of the Fe K-edge EXAFS spectra of beryl powder sample.

Figure 4.12 shows that Model-I reproduced Peaks I, II, III, IV and V in the experimental spectrum well, resulting in a low fitting residual (see Appendix). Fe substitution in Al site has been frequently reported by gemologists because their

compatibility. The interatomic distances (R) for these outer paths were taken directly from the ideal beryl structure, but the σ^2 values and coordination numbers were adjusted to best reproduce the experimental spectrum. The detail of the EXAFS fitting result is presented in the Appendix section. The Fe ion was introduced at a 6g interstitial site with a single scattering path in Figure 4.10(b). Figure 4.12 indicates that Model-II exclusively reproduced Peaks I and II in the experimental spectrum, with Peak I containing six oxygen, two aluminum, and three silicon atoms and Peak II containing three oxygen atoms. Fitting by another single scattering path provided a substantial fitting residual value.

Table 4.9 Model-I and Model-II R space fits of the Fe K-edge generated local environments of Fe in beryl samples.

Path	Model-I								Model-II				
	Fe-O ₁	Fe-Be ₁	Fe-Si ₁	Fe-O ₂	Fe-O ₃	Fe-O ₄	Fe-Si ₂	Fe-Al ₁	Fe-O ₁	Fe-Al ₁	Fe-Si ₁	Fe-O ₂	
BL1	Initial	2.00	2.65	3.32	3.71	3.88	4.54	4.52	4.59	1.98	2.38	2.68	2.99
	+/-	(0.01)	(0.04)	(0.02)	(0.04)	(0.06)	(0.08)	(0.04)	(0.20)	(0.08)	(0.28)	(0.25)	(0.43)
	IRR	2.01	2.67	3.35	3.73	3.93	4.53	4.55	4.62	2.00	2.39	2.70	3.02
	+/-	(0.01)	(0.03)	(0.02)	(0.03)	(0.05)	(0.10)	(0.04)	(0.14)	(0.09)	(0.39)	(0.31)	(0.56)
BL2	Initial	2.01	2.68	3.33	3.73	3.98	4.47	4.53	4.49	2.01	2.07	2.80	3.07
	+/-	(0.01)	(0.04)	(0.02)	(0.04)	(0.04)	(0.11)	(0.04)	(0.07)	(0.07)	(0.15)	(0.14)	(0.13)
	IRR	2.00	2.70	3.34	3.71	3.96	4.43	4.51	4.52	1.98	2.20	2.36	2.92
	+/-	(0.01)	(0.03)	(0.02)	(0.03)	(0.04)	(0.08)	(0.08)	(0.27)	(0.14)	(0.16)	(0.17)	(0.14)
BL3	Initial	2.01	2.68	3.33	3.71	3.96	4.45	4.50	4.56	2.01	2.44	2.72	3.03
	+/-	(0.01)	(0.04)	(0.02)	(0.03)	(0.05)	(0.12)	(0.06)	(0.11)	(0.05)	(0.27)	(0.20)	(0.42)
	IRR	2.00	2.70	3.34	3.72	3.96	4.42	4.51	4.53	2.00	2.53	2.76	3.05
	+/-	(0.01)	(0.03)	(0.02)	(0.03)	(0.04)	(0.05)	(0.15)	(0.47)	(0.04)	(0.12)	(0.16)	(0.31)
BL4	Initial	2.02	2.69	3.39	3.81	4.05	4.43	4.51	5.02	2.01	2.37	2.77	3.00
	+/-	(0.01)	(0.03)	(0.04)	(0.05)	(0.04)	(0.08)	(0.04)	(0.07)	(0.06)	(0.34)	(0.33)	(0.27)
	IRR	2.00	2.70	3.38	3.77	4.01	4.42	4.49	4.65	1.98	2.06	2.28	3.00
	+/-	(0.02)	(0.04)	(0.04)	(0.04)	(0.05)	(0.11)	(0.05)	(0.08)	(0.07)	(0.15)	(0.07)	(0.16)
BL5	Initial	2.01	2.69	3.34	3.70	3.95	4.43	4.51	4.53	2.00	2.38	2.69	3.00
	+/-	(0.01)	(0.03)	(0.02)	(0.03)	(0.04)	(0.08)	(0.11)	(0.37)	(0.10)	(0.42)	(0.35)	(0.44)
	IRR	2.00	2.69	3.34	3.72	3.97	4.56	4.55	4.98	2.00	2.56	2.77	3.06
	+/-	(0.01)	(0.03)	(0.01)	(0.02)	(0.04)	(0.04)	(0.02)	(0.06)	(0.04)	(0.12)	(0.15)	(0.03)
BL6	Initial	2.00	2.69	3.34	3.70	3.91	4.50	4.53	4.54	1.97	2.19	2.33	2.93
	+/-	(0.01)	(0.03)	(0.01)	(0.03)	(0.03)	(0.17)	(0.19)	(0.37)	(0.09)	(0.34)	(0.20)	(0.32)
	IRR	1.99	2.69	3.34	3.74	3.99	4.40	4.49	4.97	1.99	2.54	2.76	3.03
	+/-	(0.01)	(0.03)	(0.01)	(0.02)	(0.04)	(0.04)	(0.02)	(0.05)	(0.03)	(0.12)	(0.15)	(0.33)

Table 4.9 displays the local environments of Fe in beryl samples. After irradiation, the bond distance of the six oxygen first shell nearest to the Fe ion substitution at Al site slightly decreased. The bond length of Fe-Si₁ paths were higher than 3.39 Å, which might be attributed to multiple changes in bond distances that might have been caused by atoms moving radially and changed bonds for Fe ion occupancy in the Al site. Figure 4.13 depicts a comparison of the bond lengths of Fe neighbor atoms in beryl structure.

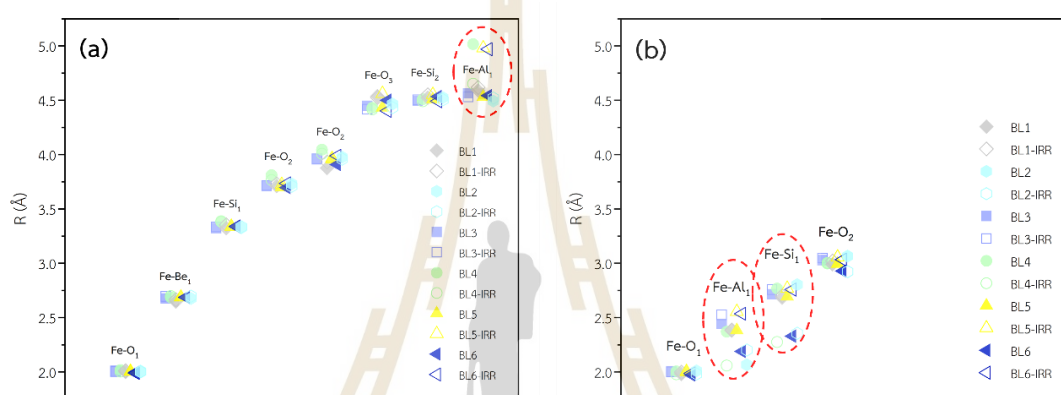


Figure 4.13 The comparative bond length of beryl sample before and after X-ray irradiation by scattering path fitting (a) bond length of Model-I fitting and (b) bond length of Model-II fitting.

Figure 4.13(a) demonstrates the bond length of Fe neighbor atoms for Model-I: the three paths of all samples had slightly distinct bond lengths, and the bond length of neighbor atoms had a moderate difference and a high distribution when faraway from Fe core atoms. The last path fitting was higher for Fe-Al, with different bond lengths for BL2, BL4, and BL6, which indicated that X-ray modified the bond length or the electronic noise signal of the EXAFS spectra. Peak I of Model-II included three scattering paths that added to the number of numerous parameters owing to computation processing limitations. The bond lengths of Fe-Al₁ and Fe-Si₁ were notably different when the 6g site was compared to the Al site, whereas the Fe-O₂ bond length was comparable.

The analysis of the EXAFS results obtained from Model-I and II fitting provided insights into the potential positions of iron (Fe) within the beryl structure. Peak I suggest that Fe tended to occupy a central position with 6 coordinated neighbors (referred to as 6 CN). However, in certain beryl samples, Fe appeared to exhibit different coordination patterns, leading to the description of Fe as occupying a tetrahedral site. The EXAFS data averaged the scattering of Fe within the beryl structure, suggesting that Fe could potentially occupy sites through substitution, such as replacing aluminum (Al), or interstitial sites like the 6g site. The first scattering path in both models yielded similar bond lengths, approximately ranging from 1.97 to 2.02 Å. Consequently, it was challenging to distinguish or confirm the exact bond length of Fe-O₁ or the quantity of Fe-occupied sites within the beryl structure. The substitution of Fe for Al sites appeared to be more common than for 6g sites, as all the samples could be fitted with five peaks using Model-I. The combination of Model-I and Model-II assumed the occupancies of isolated Fe ions at both the octahedral Al site and the 6g interstitial site, which has been reported to be feasible during heat treatment of beryl (Lin *et al.*, 2013), but could not fit the beryl EXAFS spectra in this investigation.

4.5 Polarization of crystal beryl to X-ray and UV-vis absorption.

4.5.1 X-ray Diffraction of crystal plane conformation

Out of the six beryl samples, two had a hexagonal crystal structure. The beryl crystal samples were carefully polished to investigate their physical and chemical characteristics of before and after exposure to radiation. The crystal faces of the samples were identified using X-ray diffraction. X-ray data were collected in the 2θ range of 10-50 using a Rigaku SmartLab diffractometer, with precise step-by-step measurements at 0.02 intervals and a 10 second count time for each step. This analysis was carried out at room temperature, utilizing Cu-K α radiation ($\lambda = 1.54$ Å) at 40 kV and 40 mA. The XRD results are displayed in Figure 4.14, with the beryl JCPDS- 00-009-0430 pattern as a reference. When the prismatic faces of BL2 and BL5 were exposed to X-rays, the XRD patterns exhibited peaks at 11.10° and 11.18°, respectively, corresponding to the (100) plane. Meanwhile, for measurements on the basal plane, BL2 and BL5

patterns showed peaks at 19.34° and 19.28° , respectively, indicating the (001) plane. These XRD findings confirmed that the beryl faces of BL2 and BL5 had been accurately polished to the prismatic and basal planes, denoted as plane A and plane C, respectively.

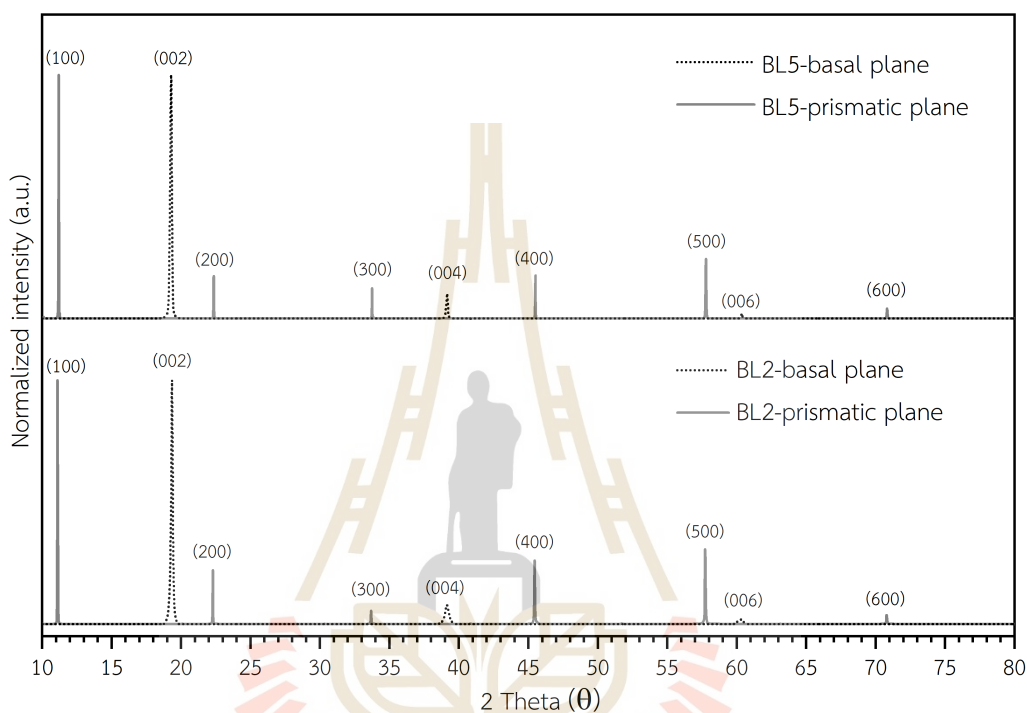


Figure 4.14 X-ray diffractogram basal plane (dote line) and prismatic plane (solid line) of crystal beryl sample BL2 and BL5.

4.5.2 UV-Vis-NIR absorption spectra for beryl crystal comparison

Figure 4.15 shows the UV-Vis-NIR absorption spectra of natural beryl and beryl exposed to X-ray irradiation, each plane-polarized. Both samples exhibited two relatively narrow absorption peaks at 375 and 427 nm, corresponding to electron transitions involving Fe^{3+} . Plane A exhibited a higher peak intensity than Plane C in these narrow peaks. The absorption in the 670-750 nm range is attributed to the charge transfer from Fe^{2+} to Fe^{3+} in octahedral positions. Interestingly, the absorbance features between Plane A and Plane C were different in BL2 (blue beryl) but were quite similar in BL5 (yellow beryl). Notably, there was a distinctive peak at 820 nm resulting from

Fe²⁺ absorption. There were also differences in the absorbance features between Plane A and Plane C, with Plane C showing higher peak intensities in BL2 but similar features in BL5. Following irradiation, the blue beryl changed to a yellowish color, and the yellow beryl had its color intensified. The absorption peak intensities at 820 nm decreased, while the absorption peaks at 375 and 427 nm were more pronounced in both color samples. The discussion of the previous UV-vis absorbance results indicates a transformation of Fe²⁺ ions into Fe³⁺ ions due to X-ray irradiation. The most significant change in the absorbance spectra was the distinct deformation feature in Plane A, which exhibited higher intensity than Plane C, particularly in the increased intensity of the broad feature around the narrow peaks at 375 and 427 nm.

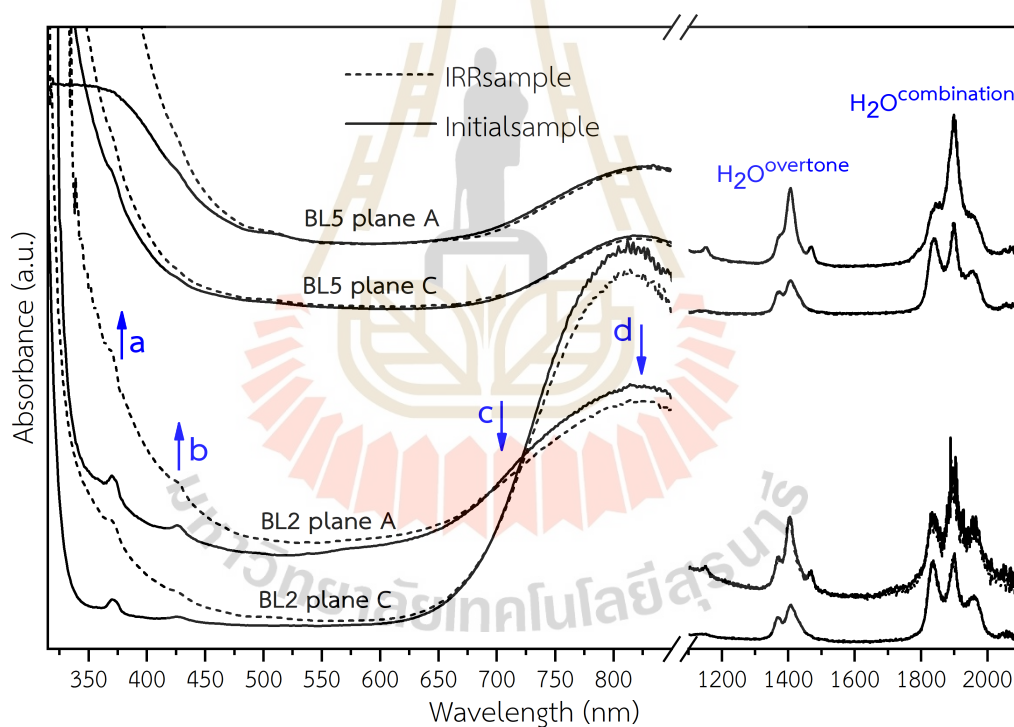


Figure 4.15 UV-Vis-NIR absorbance spectrum of beryl crystal sample.

In the NIR region, both beryl colors exhibited band peaks corresponding to the first overtone, second overtone, and combination mode of H₂O stretching vibrations. Interestingly, these NIR features remained unchanged after X-ray irradiation. However, it is important to note that the water-related features vary in terms of the

number of peaks and their intensities, depending on the plane of polarization. The crystal plane and polarization measurements yielded diverse results and left some aspects of the study unexplained. Consequently, the behavior of Fe ions and the color changes in beryl due to X-ray irradiation may be linked to alterations in both polarized planes, as these features appear to undergo changes that correlate with the crystal plane and polarization.

4.5.3 Comparison of beryl crystal using X-ray Absorption Spectroscopy

XANES spectra of powdered beryl samples revealed distinct differences before and after exposure to X-ray irradiation, as depicted in Figure 3.6. To facilitate comparison, crystal samples with different plane polarizations are illustrated in Figure 4.16.

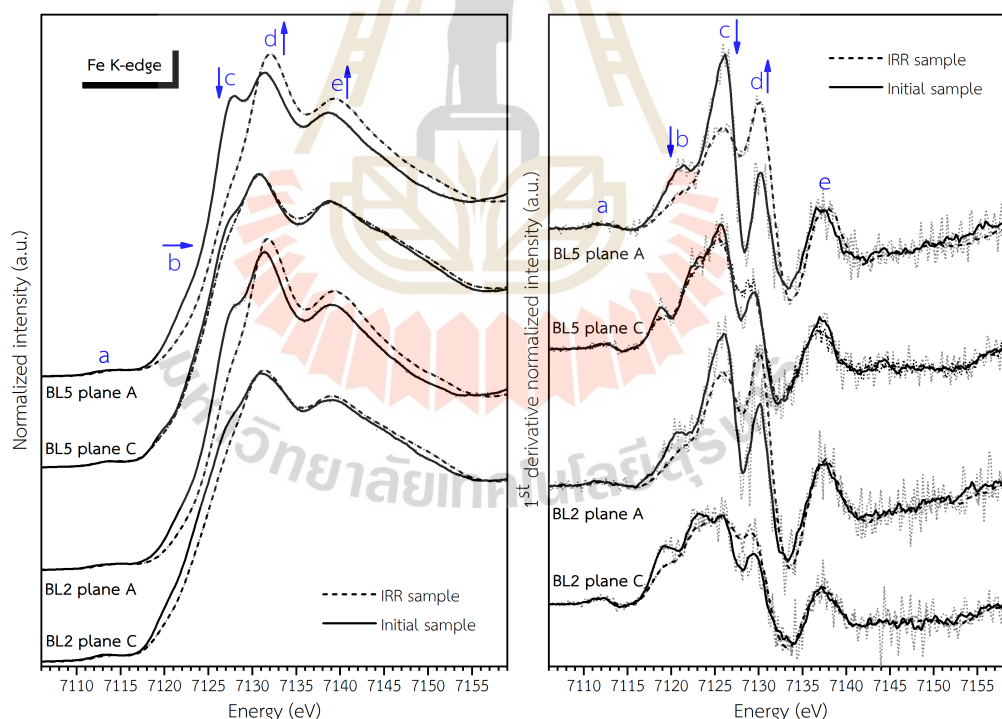


Figure 4.16. XANES spectra of crystal sample for each plane polarization direction.

The pre-edge XANES features (labeled as **a**) in both samples exhibited slight changes. Notably, in plane A, the XANES feature displayed a prominent peak difference when compared to plane C. Positions **b**, **c**, **d**, **e**, and **f** in plane A exhibited noticeable

feature alterations following beryl irradiation, with **b** and **c** being the most significantly altered positions in plane C. Particularly, **b** caused an absorption edge shift towards higher energy. The changes in absorption features are linked to the 1st derivative. Positions **b**, **c**, and **d** experienced changes in both plane polarizations after X-ray irradiation, particularly in plane A. The differing orientations of elements, bond lengths, and the distribution of Fe ions in the beryl structure between the basal plane (plane C) and the prism plane (plane A) likely contributed to the distinct XANES features in each crystal plane. This is because multiple scattering properties averaged the X-ray incident area of Fe ions across all substituted and occupied sites.

Previous research on single crystals of 3d transition metals in the R3 group reported that different linearly polarized X-ray directions produced varied features in the Ni L_3 -edge due to the $3de_g$ orbital shifting from an in-plane ($3d_x^2-y^2$) to an out-of-plane ($3d_{3z^2-r^2}$) orientation (Ghosh *et al.*, 2018). Additionally, considering oxygen vacancies (V_O) defects through density functional theory (DFT) calculations can lead to crystal distortions, cation displacement, and distortion of oxygen octahedra. These factors affect cation electronegativity and valence states, inducing effective electric polarization (Cortés Estay *et al.*, 2022). It is important to note that studying the XANES features of beryl crystal samples from only one plane polarization direction may not provide a comprehensive representation of the Fe ions within the beryl structure. Therefore, investigating the behavior of Fe ions in both powdered and crystal forms is essential. Powdered samples provide an average representation across all planes, while crystal planes offer clear insights into feature changes. Furthermore, plane A displayed significant feature changes, potentially due to the presence of Fe ions located at crystallographic sites along the *c*-axis, such as the Al site and 6g site (Andersson, 2019).

CHAPTER V

CONCLUSION

The various colors of beryl gemstone depend on primary factors such as, ratio of element composition, atomic defection and dislocation, mineral inclusion, distortion of the structure, and crystal pattern grown. Researchers have frequently observed the behavior of iron ions due to their electron activity on d-orbital transition metals, high band gap energy, ease of oxidation, and affinity for forming bonds with oxygen. Although the beryl samples in this study were low in alkali, irons were particularly vulnerable to radiation-induced oxidation. The synthetic sample contained 1.57 wt.% total iron, which was about three times higher than the natural sample, whereas colorless beryl contained just 0.28 wt.% total iron.

The color of irradiated crystal samples changed into intensive yellow (positive b^* value), except for the colorless beryl, which displayed no color change. The UV-Vis spectra of beryl presented the absorbance peak at 375 and 427 nm implied a $d-d$ electron transition of Fe^{3+} , the broad peak at 820 nm indicated the presence of Fe^{2+} , and the shoulder peak at 670-750 nm was interactions of IVCT between Fe^{2+} and Fe^{3+} in octahedral position. Iron oxidation state changed after irradiation by X-ray white beam because the absorption peak position ratio of Fe^{3+} increased and that of Fe^{2+} decreased. The Fe ion oxidation state results of UV-Vis corresponded to X-ray absorption results of pre-edge and multiple scattering regions, especially plane A of crystal sample investigation. The EPR spectra of powdered beryl revealed only a single axial Fe^{3+} center of site symmetry ($g \approx 2$) increased intensity after X-ray irradiation, which is supported by UV-Vis and XANES data.

The EXAFS calculation indicated that Fe ions were situated within a six-coordinated symmetry, consistent with the presence of Fe^{3+} centers in aluminum (Al) sites as confirmed by EPR and the pre-edge fitting of XANES data of powder samples. The simulation of the six-coordinate EXAFS path model suggested that Fe could potentially occupy positions through substitution, such as replacing aluminum (Al), or

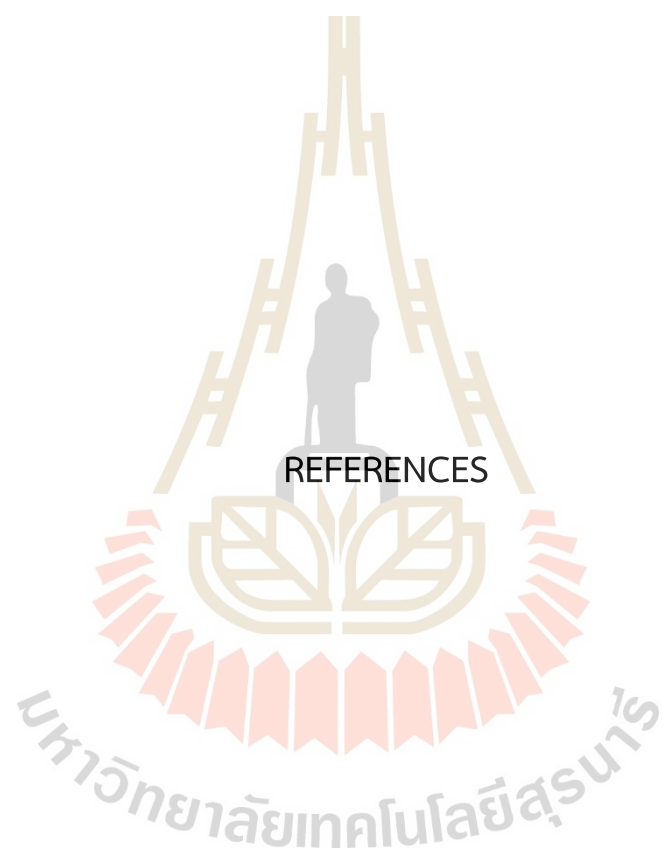
interstitial locations like the 6g site. This was supported by the observation of similar bond lengths, approximately ranging from 1.97 to 2.02 Å, in both models. As a result, it was challenging to precisely determine the bond length of the first single scattering (Fe-O₁) or the quantity of Fe-occupied sites within the beryl structure. It appeared that the substitution of Fe for Al sites was more prevalent than for 6g sites, as all the samples could be adequately described using Model-I, which comprised five peaks.

The results of the EXAFS simulation and spectral fitting before and after exposure to X-ray irradiation exhibited remarkably similar characteristics, with only a slight change in the bond length of the first single scattering. However, other analytical techniques such as UV-Vis, XANES, and EPR indicated an increase in the presence of Fe³⁺ ions or a conversion of Fe²⁺ to Fe³⁺. The primary Fe ions were found to be situated within a six-coordinated symmetry according to the EXAFS calculations. Changes in the plane polarization of Fe were observed in the UV-Vis and XANES spectra, particularly in plane A along the c-axis. Additional support for these observations comes from the appearance of a blue color, which was generated by the IVCT between Fe²⁺ and Fe³⁺ ions located at both Al and 6g sites in the beryl structure, suggesting a possible Fe-Fe pair distance of 2.49-2.51 Å. In contrast, in the antiferromagnetic configuration, the nearest Fe-Fe pair distance along the c-axis, considering the nearest Al site, was approximately 4.64 Å (Lin *et al.*, 2013). The shift in beryl coloration towards a more intense yellow hue implied an IVCT Fe²⁺-Fe³⁺ reaction phenomenon induced by X-ray exposure, leading to the conversion of Fe²⁺ ions to Fe³⁺ at both Al and 6g sites. This phenomenon resulted in a decrease in the transfer of electrons between ions with different oxidation states within the crystal lattice and an increase in the transfer of electrons between ions with the same oxidation state (Fe³⁺-Fe³⁺) or between metal ions and oxygen (Fe³⁺-O).

Furthermore, the NIR data revealed a general absence of foreign and water molecules, implying that the impinging X-ray beam could not cause any OH bond breakdown in H₂O. Furthermore, cryogenic cooling of the sample, which is commonly used to reduce free radical mobility, would most likely not help to prevent the observed oxidation effects in beryl induced by synchrotron radiation. The oxidation

process could be attributed to bond cracking and electron release (Eeckhout *et al.*, 2005).

The irradiation treatment requires special care because some irradiated gems, like beryl and spodumene gemstones, tends to have short-lived colors that fade upon exposure to bright light (Weldon, 2023). Irradiation is a less common method for enhancing beryl color. Colorless or light pink beryl gems subjected to neutron and gamma radiation take on a new shade of blue, a "maxixe-type" color (Nassau, Prescott, and Wood, 1976). This color is thought to form due to radiation-induced chemical changes involving carbonate ions in the channels (Edgar and Vance, 1977). However, unlike heat treatment results, the color gradually fades when exposed to light because the maxixe-type color is unstable. As a result, the gem and jewelry industry does not consider radiation treatments as acceptable beryl enhancements. If this color could be stabilized and produced sufficiently, the stone would have great potential as a gem material. Both beryl color samples in this study were treated to an increased yellow shade (*b) by X-ray synchrotron, which tended to be a stable color. In addition, irradiation of beryl by an X-ray synchrotron source did not result in any residual radioactivity being released into the environment. The irradiated beryls are safe to handle and wear, are not brittle as usual. However, care must be taken not to damage pointed faceted corners and edges, like avoiding exposure to high temperatures. The incident X-ray beam size and incident time in a synchrotron source can be adjusted to create two- or three-color shade in one beryl gemstone.



REFERENCES

REFERENCES

- Adamo, I., Gatta, G. D., Rotiroti, N., Diella, V., and Pavese, A. (2008). Gemmological investigation of a synthetic blue beryl: a multi-methodological study. *Mineralogical Magazine*, 72(3), 799-808.
- Ahmed, S. (2009). Value addition in diamonds and other gemstones by nuclear radiation: the phobias and safety considerations. *Journal Atoms for Peace*, 2(4), 109-418.
- Alkmim, D. G., Almeida, F. O. T., and Lameiras, F. S. (2017). FTIR study of aquamarines after gamma irradiation, heat treatment and electrodiffusion. *REM-International Engineering Journal*, 70(3), 289-292.
- Andersson, L. O. (1979). The difference between Maxixe beryl and Maxixe-type beryl: An electron paramagnetic resonance investigation. *Journal of Gemmology*, 16(5), 313-317.
- Andersson, L. O. (2006). The positions of H⁺, Li⁺ and Na⁺ impurities in beryl. *Physics and Chemistry of Minerals*, 33, 403-416.
- Andersson, L. O. (2013). The yellow color center and trapped electrons in beryl. *The Canadian Mineralogist*, 51(1), 15-25.
- Andersson, L. O. (2019). Comments on beryl colors and on other observations regarding iron-containing beryls. *The Canadian Mineralogist*, 57(4), 551-566.
- Atanasov, M., Andreici, E. E. L., Avram, N. M., Brik, M. G., and Neese, F. (2022). First-Principles Study of Optical Absorption Energies, Ligand Field, and Spin-Hamiltonian Parameters of Cr³⁺ Ions in Emeralds. *Inorganic Chemistry*, 61(1), 178-192. doi: 10.1021/acs.inorgchem.1c02650.
- Aurischio, C., Fioravanti, G., Grubessi, O., and Zanazz, P. F. (1988). Reappraisal of the crystal chemistry of beryl. *American Mineralogist*, 73, 826-83.

- Bačík, P., Fridrichová, J., Uher, P., Rybár, S., Bizovská, V., Luptáková, J., Vrablíková, D., Pukančík, L., and Vaculovič, T. (2019). Octahedral substitution in beryl from weakly fractionated intragranitic pegmatite Predné Solisko, Tatry Mountains (Slovakia): the indicator of genetic conditions. *Journal of Geosciences*, *64*, 1-14. doi: 10.3190/jgeosci.272.
- Blak, A., Isotani, S., and Watanabe, S. (1982). Optical absorption and electron spin resonance in blue and green natural beryl. *January Physics and Chemistry of Minerals*, *8*(4), 161-166.
- Bootkul, D., Chaiwai, C., Tippawan, U., Wanthanachaisaeng, B., and Intarasiri, S. (2015). Analysis and modification of blue sapphires from Rwanda by ion beam techniques. *Nuclear Instruments and Methods in Physics Research Section B: Beam Interactions with Materials and Atoms*, *365*, 288-293.
- Brown, G. E. and Mills, B. A. (1986). High-temperature structure and crystal chemistry of hydrous alkali-rich beryl from the Harding pegmatite, Taos County, New Mexico. *American Mineralogist*, *71*, 547-556.
- Brown, G. E., Farges, F., and Calas, G. (1995). X-ray scattering and X-ray spectroscopy studies of silicate melts. In J.F. Stebbins, P.F. McMillan, and D. Dingwell, Eds., *Structure, Dynamics, and Properties of Silicate Melts*, *32*, 317-410. Reviews in Mineralogy, Mineralogical Society of America, Chantilly, Virginia.
- Bunnag, N. and Wanthanachaisaeng, B. (2014). Heat Treatment of Aquamarine, *The 4th International Gem and Jewelry Conference*, 97-100.
- Bunnag, N., Kasri, B., Setwong, W., Sirisurawong, E., Chotsawat, M., Chirawatkul, P., and Saiyasombat, C. (2020). Study of Fe ions in aquamarine and the effect of dichroism as seen using UV-Vis, NIR and X-ray. *Radiation Physics and Chemistry*, *177*, 1-7.
- Burns R. G. (1993). *Mineralogical applications of crystal field theory*. (2nd ed.). Cambridge University Press, Cambridge.
- Calas, G. and Petiau, J. (1983a). Coordination of iron in oxide glasses through high-resolution K-edge spectra: information from the pre-edge. *Solid State Communications*, *48*, 625-629.

- Calas, G. and Petiau, J. (1983b). Structure of oxide glasses: Spectroscopic studies of local order and crystallochemistry. Geochemical implications. *Bulletin de Mineralogies*, 106, 33-55.
- Carmo, L. S., Watanabe, S., and Bittencourt, J. F. (2015). High-dose dosimetry of beta rays using blue beryl dosimeters. *Seventh International Nuclear Atlantic Conference*. São Paulo, Brazil: ABEN.
- Chankhantha, C. and Thanasuthipitak, P. (2012). Heat treatment of Aquamarine and morganite from Madagascar. *The 38th Congress on Science and Technology of Thailand*. Bangkok, Thailand.
- Chankhantha, C., Thanasuthipitak, P., and Kidkhunthod, P. (2016). Iron K-edge XANES study of heated green beryl from Madagascar. *Walailak Journal of Science and Technology*, 13(12), 977-983.
- Chen, W., Gu, H., Liu, J., Wang, F., Ma, D., and Zhu, R. (2010). Electrolytic coloration and spectral properties of natural beryl crystals. *Physica B - Condensed Matter*, 405, 331-334.
- Chen, Y., Wang, Y., and Shu, J. (2024). The effect of oxygen vacancies on the color formation of aquamarine, *Journal of Solid-State Chemistry*, 329. doi.org/10.1016/j.jssc.2023.124400.
- Cortés Estay, E. A., Ong, S. P., Ross, C. A., and Florez, J. M. (2022). Oxygen Deficiency and Migration-Mediated Electric Polarization in Magnetic Fe,Co-Substituted SrTiO₃- δ . *Magnetochemistry*, 8, 144. doi.org/10.3390/magnetochemistry8110144.
- Czaja, M., Lisiecki, R., Chrobak, A., Sitko, R., and Mazurak, Z. (2018). The absorption and luminescence spectra of Mn³⁺ in beryl and vesuvianite. *Physics and Chemistry of Minerals*, 45(5), 475-488. doi:10.1007/s00269-017-0934-x.
- Deer, W. A., Howie, R. A., and Zussman, J. (1997). *Rock-forming minerals (Vols 2A): single-chain silicates*. (2nd ed.). London: GSL.
- Edgar, A. and Vance, E. R. (1977). Electron paramagnetic resonance, optical absorption, and magnetic circular dichroism studies of the CO₃-molecular-ion in irradiated natural beryl. *Physics and Chemistry of Minerals*, 1(2), 165-178.

- Eeckhout, S. G., Neisius, T., and Castañeda, C. (2005). Oxidation effects in beryl induced by synchrotron radiation. *Nuclear Instruments and Methods in Physics Research Section B: Beam Interactions with Materials and Atoms*, 229(1), 73-77.
- Farges, F. (2001). Crystal-chemistry of Fe in natural grandidierites: A XAFS spectroscopy study at the Fe K-edge. *Physics and Chemistry of Minerals*, 28, 619-629.
- Fridrichová, J., Bačík, P., Bizovská, V., Libowitzky, E., Škoda, R., Uher, P., Ozdín, D., and Števkó, M. (2016). Spectroscopic and bond-topological investigation of interstitial volatiles in beryl from Slovakia. *Physics and Chemistry of Minerals*, 43(6), 419-437. doi:10.1007/s00269-016-0806-9.
- Fridrichová, J., Bačík, P., Rusinová, P., and Antal, P. (2015). Optical and crystal-chemical changes in aquamarines and yellow beryls from Thanh Hoa province, Vietnam induced by heat treatment. *Physics and Chemistry of Minerals*, 42, 287-302.
- Fridrichová, J., Bačík, P., Rusinová, P., Antal, P., Škoda, R., Bizovská, V., and Miglierini, M. (2014). Optical and crystal-chemical changes in aquamarines and yellow beryls from Thanh Hoa province, Vietnam induced by heat treatment. *Physics and Chemistry of Minerals*, 42(4), 287-302.
- Fritsch, E. and Rossman G. R. (1988). An update on color in gems. Part 2: Colors involving multiple atoms and color centers. *Gems and Gemology*, 24(1), 3-15.
- Ghosh, A., Chen, K. H., Qiu, X. S., Hsieh, S. H., Shao, Y. C., Du, C. H., Wang, H. T., Chin, Y. Y., Chiou, J. W., Ray, S. C., Tsai, H. M., Pao, C. W., Lin, H. J., Lee, J. F., Sankar, R., Chou, F. C., and Pong, W. F. (2018). Anisotropy in the magnetic interaction and lattice-orbital coupling of single crystal Ni_3TeO_6 . *Scientific Reports*, 8(1), 15779. doi:10.1038/s41598-018-33976-w.
- Giuli, G., Paris, E., Hess, K.-U., Dingwell, D. B., Cicconi, M. R., Eeckhout, S. G., Fehr, K. T., and Valenti, P. (2011). XAS determination of the Fe local environment and oxidation state in phonolite glasses, *American Mineralogist*, 96(4), 631-636. doi:10.2138/am.2011.3464.
- Giuli, G., Paris, E., Pratesi, G., Koeberl, C., and Cipriani, C. (2003). Iron oxidation state in the Fe-rich layer and silica matrix of Libyan Desert Glass: a high resolution XANES study. *Meteoritics & Planetary Science*, 38, 1181-1186.

- Giuli, G., Pratesi, G., Cipriani, C., and Paris, E., (2002). Iron local structure in tektites and impact glasses by extended X-ray absorption fine structure and high-resolution X-ray absorption near-edge structure spectroscopy. *Geochimica et Cosmochimica Acta*, 66(24), 4347-4353.
- Giuliani, G., France-Lanord, C., Zimmermann, J. L., Cheilletz, A., Arboleda, C., Charoy, B., Coget, P., Fontan F., and Giard, D. (1997). Fluid Composition, δD of Channel H_2O , and $\delta^{18}O$ of Lattice Oxygen in Beryls: Genetic Implications for Brazilian, Colombian, and Afghanistani Emerald Deposits. *International Geology Review*, 39(5), 400-424.
- Goldman, S. D., Rossman, G. R., and Parkin, K. M. (1978). Channel constituents in beryl. *Physics and Chemistry of Minerals*, 3(3), 225-235.
- Groat, L. A., Rossman, G. R., Dyar, M. D., Turner, D., Pic-Coli, P. M. B., Schultz, A. J., and Ottolini, L. (2010). Crystal chemistry of dark blue aquamarine from The True-Blue Showing Yukon Territory Canada. *The Canadian Mineralogist*, 48, 597-613.
- Guda, A. A., Guda, S.A., Martini, A., Kravtsova, A. N., Algasov, A., Bugaev, A., Kubrin, S. P., Guda, L. V., Šot, P., van Bokhoven, J.A., Copéret, C., and Soldatov, A. V. (2021). Understanding X-ray absorption spectra by means of descriptors and machine learning algorithms. *npj Computational Materials*, 7, 203.
- Hayes, T. M. and Boyce, J. B. (1983). Extended X-ray absorption fine structure spectroscopy. *Solid State Physics*, 37, 173-351.
- Ibragimova, E. M., Mukhamedshina, N. M., and Islamov, A. Kh. (2009). Correlations between admixtures and color centers created upon irradiation of natural beryl crystals. *Neorganicheskie Materialy*, 45(2), 199-204.
- Idris, S., Ghazali, Z., Hashim, S. A., Ahmad, S., and Jusoh, M. S. (2012). Electron beam irradiation of gemstone for color enhancement. *American Institute of Physics Conference Proceedings*, 1482, 197-199.
- Isotani, S., Blak, A. R., and Watanabe, S., (2010). UV optical absorption spectra analysis of beryl crystals from Brazil, *Physica B: Condensed Matter*, 405(6), 1501-1508. doi:10.1016/j.physb.2009.12.029.

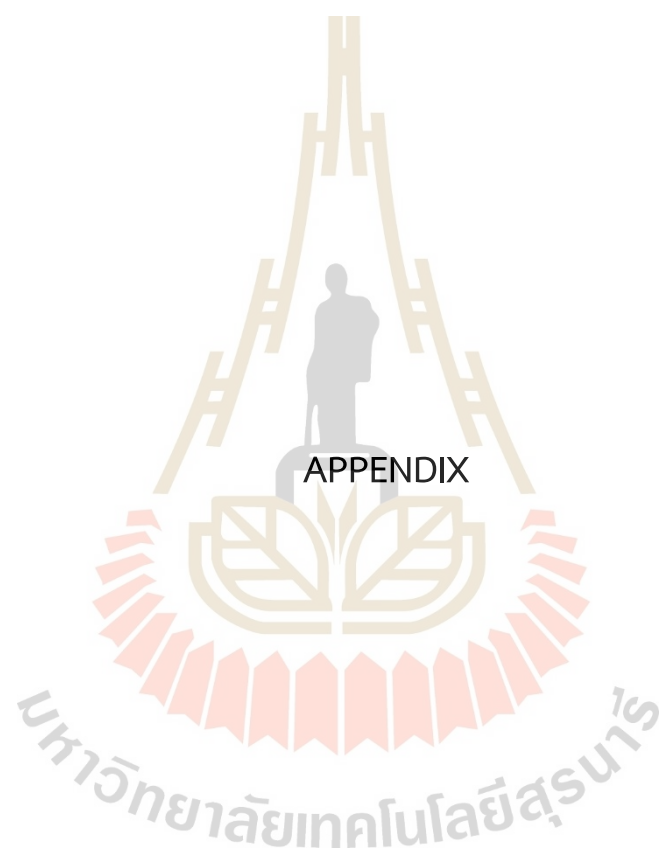
- Ittipongse, A., Maneewong, A., Pangza, K., and Charoennam, T. (2017). The optical characteristic of electron irradiated beryl by UV-Visible and mid-IR spectroscopic analyses. *SNRU Journal of Science and Technology*, 9(3), 568-573.
- Jain, A., Ong, S. P., Hautier, G., Chen, W., Richards, W. D., Dacek, S., Cholia, S., Gunter, D., Skinner, D., Ceder, G., and Persson, K. A. (2013). Commentary: The Materials Project: A materials genome approach to accelerating materials innovation. *APL Materials*, 1(1), 011002. doi:10.1063/1.4812323.
- Kati, M. I., Türemis, M., Keskin, I. C., Tastekin, B., Kibar, R., Çetin, A., and Can, N. (2012). Luminescence behaviour of beryl (aquamarine variety) from Turkey, *Journal of Luminescence*, 132(10), 2599-2602. doi:10.1016/j.jlumin.2012.03.058.
- Khaibullin, R. I., Lopatin, O. N., Vagizov, F. G., Bazarov, V. V., Bakhtin, A. I., Khaibullin, I. B., and Aktas, B. (2003). Coloration of natural beryl by iron ion implantation. *Nuclear Instruments and Methods in Physics Research Section B: Beam Interactions with Materials and Atoms*, 206, 277-281.
- King, H. M. (2020). *Beryl a minor ore of beryllium, and one of the most important gem minerals*. Retrieved from <https://geology.com/minerals/beryl.shtml>
- Klencsár, Z. and Köntös, Z. (2018). EPR analysis of Fe³⁺ and Mn²⁺ complexation sites in fulvic acid extracted from Lignite. *The Journal of Physical Chemistry A*, 122(12), 3190-3203.
- Koivula J. I. and Keller P. C. (1985). Russian flux-grown synthetic emeralds. *Gems and Gemology*, 21, 79-85.
- Leone, A., Caucia, F., Leone, A., and Marinoni, L. (2015). AVASPEC 2048: An innovative spectroscopic methodology to differentiate the natural emeralds from the synthetic ones. *Periodico di Mineralogia*, 84(2), 247-261.
- Lin, J., Chen, N., Huang, D., and Pan, Y. (2013). Iron pairs in beryl: New insights from electron paramagnetic resonance, synchrotron X-ray absorption spectroscopy, and ab initio calculations. *American Mineralogist*, 98(10), 1745-1753.
- Luangpakdee, M., Lomthong, P., Seneekatima, K., Bootkul, D., and Wanthanachaisaeng, B. (2016). Effect of Heat Treatment and Ion Implantation on Zambian aquamarine. *The 5th GIT International Gem and Jewelry Conference, Chonburi, Thailand (pp. 260-264)*. Thailand: GIT.

- Marfunin, A. S. (1979). *Physics of Minerals and Inorganic Materials: an Introduction*. Berlin: Springer.
- Mathew, G., Karanthy, R. V., Gundu Rao T. K., and Deshpande, R.S. (1998). Maxixe-type colour centre in natural colourless beryl from Orissa, India: An ESR and OA investigation. *Journal of Gemmology*, 26(4), 238-251.
- Mihalynuk, G. M. and Lett, R. (2004). Composition of Logtung Beryl (Aquamarine) by ICPES/MS: A Comparison with Beryl Worldwide. In: *Geological Fieldwork 2003, British Columbia Ministry of Energy and Mines, British Columbia Geological Survey*, 1, 141-146.
- Mittani, J. C. R., Watanabe, S., Chubaci, J. F. D., Matsuoka, M., Baptista D. L., and Zawislak, F. C. (2002). γ -Radiation effects on colourless silicates of beryl. *Nuclear Instruments and Methods in Physics Research Section B: Beam Interactions with Materials and Atoms*, 191(1), 281-284.
- Nassau, K. (1974). The effect of Gamma rays on the color of beryl, smoky quartz, amethyst, and topaz, *Lapidary Journal*, 28, 20-40.
- Nassau, K. (1984). *Gemstone enhancement: Heat, irradiation, impregnation, dyeing, and other treatments which alter the appearance of gemstones, and the detection of such treatments*. Boston: Butterworths.
- Nassau, K., McClure, S. F., Elen, S., and Shigley, J. E. (1997). Synthetic moissanite: A new diamond substitute. *Gems and Gemology*, 33, 260-275.
- Nassau, K., Prescott B. E., and Wood, D. L. (1976). The deep blue Maxixe-type color center in beryl. *American Mineralogist*, 61(1), 100-107.
- Newville, M. (2013). Larch: An analysis package for XAFS and related spectroscopies. *Journal of Physics: Conference Series*, 430(1), 012007. doi:10.1088/1742-6596/430/1/012007.
- Ozdín, D. (2010). Beryl and phenakite from granitic pegmatites of the Sitina tunnel in Bratislava (Slovak Republic). *Bull mineral-petrol Odd Nár Muz (Praha)*, 18, 78-84.
- Petasis, D. T. and Hendrich, M. P. (2015). [Methods in Enzymology] || Quantitative Interpretation of Multifrequency Multimode EPR Spectra of Metal Containing Proteins, Enzymes, and Biomimetic Complexes. *Methods in Enzymology*, 563, 171-208. doi:10.1016/bs.mie.2015.06.025.

- Platonov A. N, Taran, M. N., Minko, O. E., and Polshyn, E. V. (1978). Optical absorption spectra and nature of color of iron-containing beryls. *Physics and Chemistry of Minerals*, 3, 87-88.
- Pough, F. H. and Rogers, T. H. (1947). Experiments in X-ray irradiation of gemstones. *American Mineralogist*, 32, 31-43.
- Příkryl, J., Novák, M., Filip, J., Gadas, P., and Galiová, M. V. (2014). Iron+magnesium-bearing beryl from granitic pegmatites: An EPMA, LA-ICP-MS, Mössbauer spectroscopy, and powder XRD study. *The Canadian Mineralogist*, 52(2), 271-284.
- Rager, H. and Schneider, H. (1986). EPR study of Fe³⁺ centers in crystobalite and tridymite. *American Mineralogist*, 71, 105-110.
- Ravel, B. and Newville, M. (2005). ATHENA, ARTEMIS, HEPHAESTUS: data analysis for X-ray absorption spectroscopy using IFEFFIT. *Journal of Synchrotron Radiation*, 12, 537-541.
- Robert D., Fritsch E., and Koivula J. I. (1990). "Emeraldolite": A new synthetic emerald overgrowth on natural beryl. *Gems & Gemology*, 26(4), 288-293.
- Ruzeng, Y., Hongyi, X., and Minjie, L. (2007). The effect of heat treatment on colour, quality and inclusions of aquamarine from China. *The Journal of gemology*, 30(5), 297-301.
- Saha, N., Sarkar, A., Ghosh, A. B., Dutta, A. K., Bhadu, G. R., Paul, P., and Adhikary, B. (2015). Highly active spherical amorphous MoS₂: facile synthesis and application in photocatalytic degradation of rose bengal dye and hydrogenation of nitroarenes. *Royal Society of Chemistry Advances*, 5, 88848-88856. doi:10.1039/c5ra19442c.
- Samoilovich, M. I., Tsinober, L. I., and Dunin-Barkovskii, R. L. (1971). Nature of the coloring in iron-containing beryl. *Soviet physics, crystallography*, 16, 147-150.
- Sherriff, b., Grundy, H. D., haRtMan, J. S., hawthORne, F. C., and ČěRný, P. (1991). The incorporation of alkalis in beryl: multi-nuclear MAS NMR and crystal-structure study. *The Canadian Mineralogist*, 29, 271-285.
- Shigley, J. E. and Foord, E. E. (1984). Gem-quality red beryl from the Wah-Wah Mountains, Utah. *Gems and Gemology*, 20, 208-221.

- Shigley, J. M., McClure, S. F., Cole, J. E., Koivula, J. I., Lu, T., Elen, S., and Demianets, L. N. (2001). Hydrothermal Synthetic Red Beryl from the Institute of Crystallography, Moscow. *Gems and Gemology*, 37, 42-55.
- Sudmuang, P., Krainara, S., Kongtawong, S., Tong-orn, A., Suradet, N., Klinkhieo, S., and Klysubun, P. (2014). Commissioning of the 2.4T multipole wiggler and the 6.5T superconducting wavelength shifter at Siam Photon Source. *Proceedings of the 5th International Particle Accelerator Conference, Dresden, Germany* (pp. 1192-1194). Geneva, Switzerland: JACoW. doi:10.18429/JACoW-IPAC2014-TUPRO068.
- Sultana, N. and Podila, S. P. (2018). Aquamarine Gemstone. *International Journal of Scientific Research in Science and Technology*, 4(11), 342-356.
- Synchrotron Light Research Institute. (2015). *Synchrotron Radiation*. Retrieved from <https://www.slri.or.th/en/machine/synchrotron-radiation.html>
- Taran, M. N., Dyar, M. Da., Naumenko, I. V., and Vyshnevsky, O. A., (2015). Spectroscopy of red dravite from northern Tanzania. *Physics and Chemistry of Minerals*, 42(7), 559-568. doi:10.1007/s00269-015-0743-z.
- Taran, M. N., Dyar, M. D., and Khomenko, V. M. (2018). Spectroscopic study of synthetic hydrothermal Fe³⁺-bearing beryl. *Physics and Chemistry of Minerals*, 45, 489-496. doi:10.1007/s00269-017-0936-8.
- Taran, M. N., Klyakhin, V. A., Platonov, A. N., Pol'shin, E. V., and Indutny, V. V. (1989). Optical spectra of natural and artificial iron-containing beryls at 77-297 K. *Soviet Physics. Crystallography*, 34, 882-884.
- Taran, M. N. and Rossman, G. R. (2001). Optical spectroscopic study of tuzovite and a re-examination of the beryl, cordierite, and osumilite spectra. *American Mineralogist*, 86(9), 973-980.
- Taran, M. N. and Vyshnevskiy, O. A. (2019). Be, Fe²⁺-substitution in natural beryl: an optical absorption spectroscopy study. *Physics and Chemistry of Minerals*, 46, 795-806.
- Uher, P., Chudík, P., Bacík, P., Vaculovic, T., and Galiová, M. (2010). Beryl composition and evolution trends: an example from granitic pegmatites of the beryl-columbite subtype, Western Carpathians, Slovakia. *Journal of Geosciences*, 55, 69-80.

- Ventura, D. G., Bellatreccia, F., and Rossi, P. (2007). The single-crystal, polarized-light, FTIR spectrum of stoppaniite, the Fe analogue of beryl. *Physics and Chemistry of Minerals*, 34, 727-731.
- Vogel, P. (1934). Optische Untersuchungen am Smaragd und einigen anderen durch Chrom gefärbten Mineralien. Neues Jahrbuch für Mineralogie, *Geologic und Paleontologie*, A68, 401-438.
- Wang, H., Guan, Q., Liu, Y., and Guo, Y. (2022a). Effects of transition metal ions on the colour of blue-green beryl. *Minerals*, 12(1), 86.
- Wang, H., Shu, T., Chen, J., and Guo, Y. (2022b). Characteristics of channel-water in blue-green beryl and its influence on colour. *Crystals*, 12(3), 435.
- Weldon, R. (2023). An introduction to gem treatments. *Gemological Institute of America*. Retrieved from <https://www.gia.edu/gem-treatment>
- Weyl, W. A. (1951) Light absorption as a result of an interaction of two states of valency of the same element. *The Journal of Physical Chemistry A*, 55, 507-512.
- Wilke, M., Farges, F., Petit, P. E., Brown Jr., G. E., and Martin, F. (2001). Oxidation state and coordination of Fe in minerals: an Fe K-XANES spectroscopic study. *American Mineralogist*, 86(5), 714-730.
- Wood, D. L. and Nassau, K. (1968). The characterization of beryl and emerald by visible and infrared absorption spectroscopy. *American Mineralogist: Journal of Earth and Planetary Materials*, 53, 777-800.
- Yakubovich, O. V., Pekov, I. V., Steele, I. M., Massa, W., and Chukanov, N. V. (2009). Alkali metals in beryl and their role in the formation of derivative structural motifs: Comparative crystal chemistry of vorobyevite and pezzottaite. *Crystallography Reports*, 54(3), 399-412.
- Zagoritis, A. (2022). Gemstone treatments-heating and irradiation. *GIA Gemologist Article*. Retrieved from <https://www.theraregemstonecompany.com/gemology-articles/gemstone-treatments-heating-and-irradiation>



APPENDIX

มหาวิทยาลัยเทคโนโลยีสุรนารี

APPENDIX

As a consequence of the EXAFS computation and sample spectra fitting

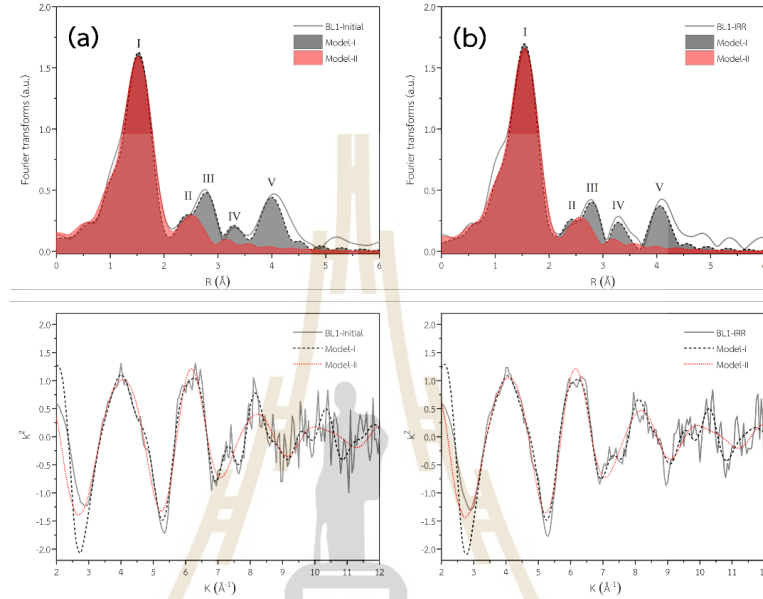


Figure A.1 Models I and II's IFEFFIT calculations are compared to experiment spectra of BL1-Initial (a) and BL1-IRR (b).

Table A.1 Model-I and Model-II were used to fit the first scattering path of neighboring atoms nearest to Fe ions in the BL1 sample.

Model	Path	BL1-Initial				R-factor	BL1-IRR				R-factor
		CN	σ^2 (Å ²)	R (Å)	SD		CN	σ^2 (Å ²)	R (Å)	SD	
I	Fe-O ₁	6	0.005	2.00	0.01		6	0.005	2.01	0.01	
	Fe-Be ₁	3	0.003	2.65	0.04	0.0276	3	0.003	2.67	0.03	0.0293
	Fe-Si ₁	6	0.008	3.32	0.02	E0 shift	6	0.009	3.35	0.02	E0 shift
	Fe-O ₂	6	0.008	3.71	0.04	-3.0	6	0.003	3.73	0.03	-1.3
	Fe-O ₃	12	0.020	3.88	0.06		12	0.018	3.93	0.05	
	Fe-O ₄	6	0.003	4.52	0.08		6	0.003	4.53	0.10	
	Fe-Si ₂	6	0.003	4.54	0.04		6	0.003	4.55	0.04	
	Fe-Al ₁	2	0.003	4.59	0.20		2	0.003	4.62	0.14	
II	Fe-O ₁	6	0.006	1.98	0.08	R-factor	6	0.006	2.00	0.09	R-factor
	Fe-Al ₁	2	0.013	2.38	0.28	0.0050	2	0.014	2.39	0.39	0.0082
	Fe-Si ₁	3	0.012	2.68	0.25	E0 shift	3	0.014	2.70	0.31	E0 shift
	Fe-O ₂	3	0.003	2.99	0.43	-6.3	3	0.003	3.02	0.56	-4.2

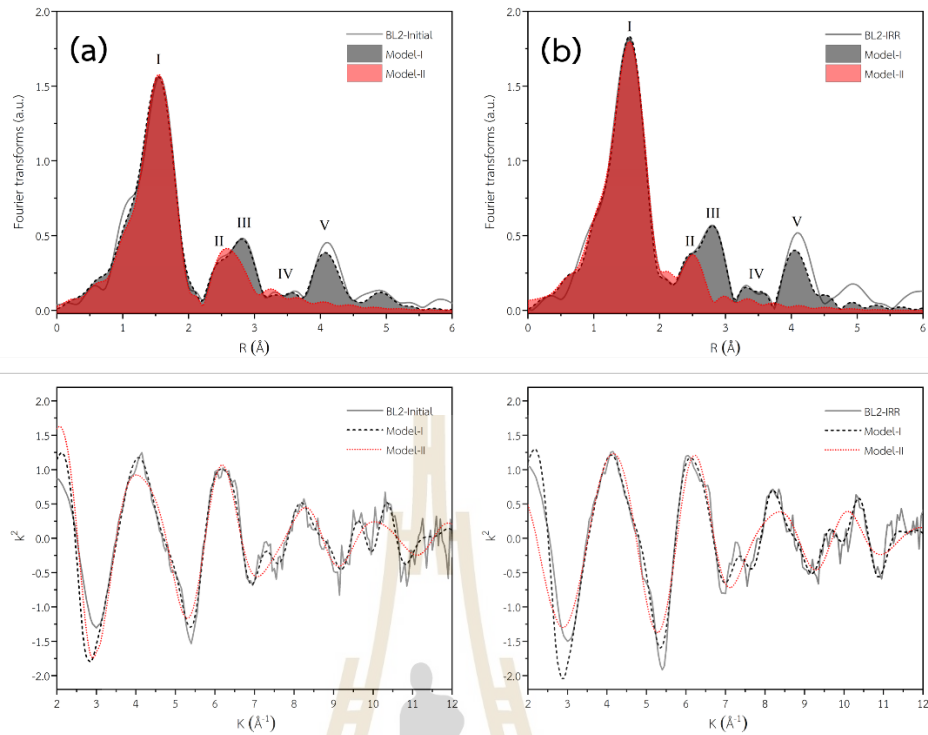


Figure A.2 Models I and II's IFEFFIT calculations are compared to experiment spectra of BL2-Initial (a) and BL2-IRR (b).

Table A.2 Model-I and Model-II were used to fit the first scattering path of neighboring atoms nearest to Fe ions in the BL2 sample.

Model	Path	BL2-Initial					BL2-IRR				
		CN	σ^2 (\AA^2)	R (\AA)	SD		CN	σ^2 (\AA^2)	R (\AA)	SD	
I	Fe-O ₁	6	0.007	2.01	0.01	R-factor	6	0.005	2.00	0.01	R-factor
	Fe-Be ₁	3	0.004	2.68	0.04	0.0175	3	0.001	2.70	0.03	0.0170
	Fe-Si ₁	6	0.009	3.33	0.02	E0 shift	6	0.007	3.34	0.02	E0 shift
	Fe-O ₂	6	0.004	3.73	0.04	-0.3	6	0.003	3.71	0.03	0.0
	Fe-O ₃	12	0.012	3.98	0.04		12	0.016	3.96	0.04	
	Fe-O ₄	6	0.006	4.47	0.11		6	0.003	4.43	0.08	
	Fe-Si ₂	6	0.002	4.53	0.04		6	0.003	4.51	0.08	
	Fe-Al ₁	2	0.000	5.49	0.07		2	0.003	4.52	0.27	
II	Fe-O ₁	6	0.005	2.01	0.07	R-factor	6	0.008	1.98	0.14	R-factor
	Fe-Al ₁	2	0.010	2.07	0.15	0.0156	2	0.003	2.20	0.16	0.0091
	Fe-Si ₁	3	0.018	2.80	0.14	E0 shift	3	0.008	2.36	0.17	E0 shift
	Fe-O ₂	3	0.004	3.07	0.13	4.6	3	0.004	2.92	0.14	-7.5

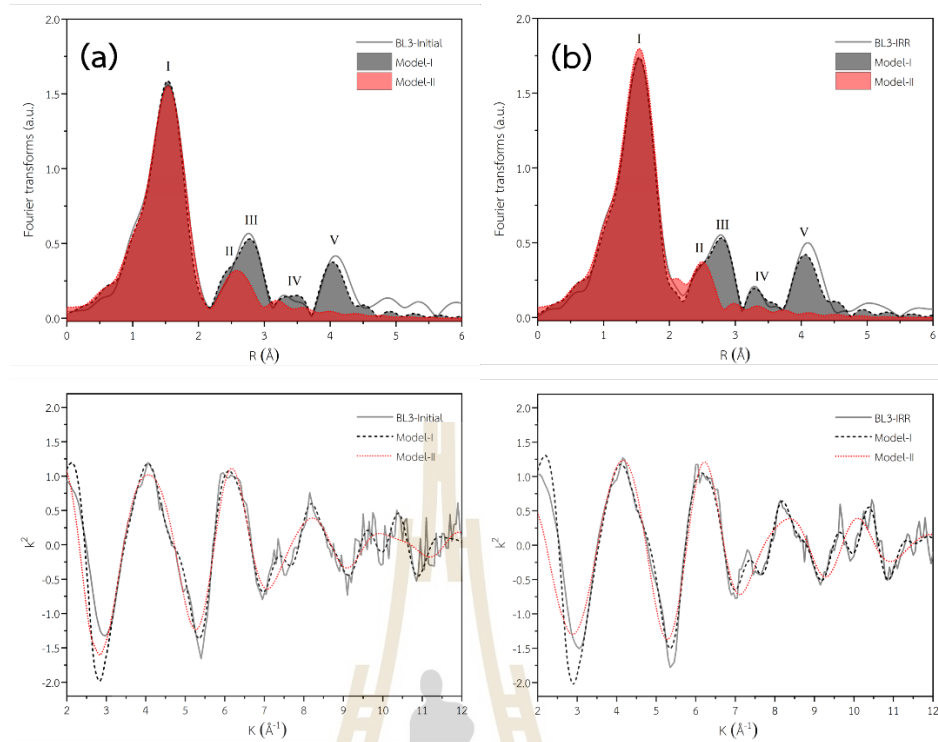


Figure A.3 Models I and II's IFEFFIT calculations are compared to experiment spectra of BL3-Initial (a) and BL3-IRR (b).

Table A.3 Model-I and Model-II were used to fit the first scattering path of neighboring atoms nearest to Fe ions in the BL3 sample.

Model	Path	BL3-Initial					BL3-IRR				
		CN	σ^2 (\AA^2)	R (\AA)	SD		CN	σ^2 (\AA^2)	R (\AA)	SD	
I	Fe-O ₁	6	0.006	2.01	0.01	R-factor	6	0.006	2.00	0.01	R-factor
	Fe-Be ₁	3	0.004	2.68	0.04	0.0188	3	0.003	2.70	0.03	0.0125
	Fe-Si ₁	6	0.007	3.33	0.02	E0 shift	6	0.008	3.34	0.02	E0 shift
	Fe-O ₂	6	0.003	3.71	0.03	-0.8	6	0.003	3.72	0.03	0.5
	Fe-O ₃	12	0.014	3.96	0.05		12	0.016	3.96	0.04	
	Fe-O ₄	6	0.003	4.45	0.12		6	0.003	4.42	0.05	
	Fe-Si ₂	6	0.003	4.50	0.06		6	0.003	4.51	0.15	
	Fe-Al ₁	2	0.003	4.56	0.11		2	0.003	4.53	0.47	
II	Fe-O ₁	6	0.007	2.01	0.05	R-factor	6	0.006	2.00	0.04	R-factor
	Fe-Al ₁	2	0.017	2.44	0.27	0.0023	2	0.016	2.53	0.12	0.0018
	Fe-Si ₁	3	0.012	2.72	0.20	E0 shift	3	0.009	2.76	0.16	E0 shift
	Fe-O ₂	3	0.003	3.03	0.52	-1.6	3	0.003	3.05	0.31	0.4

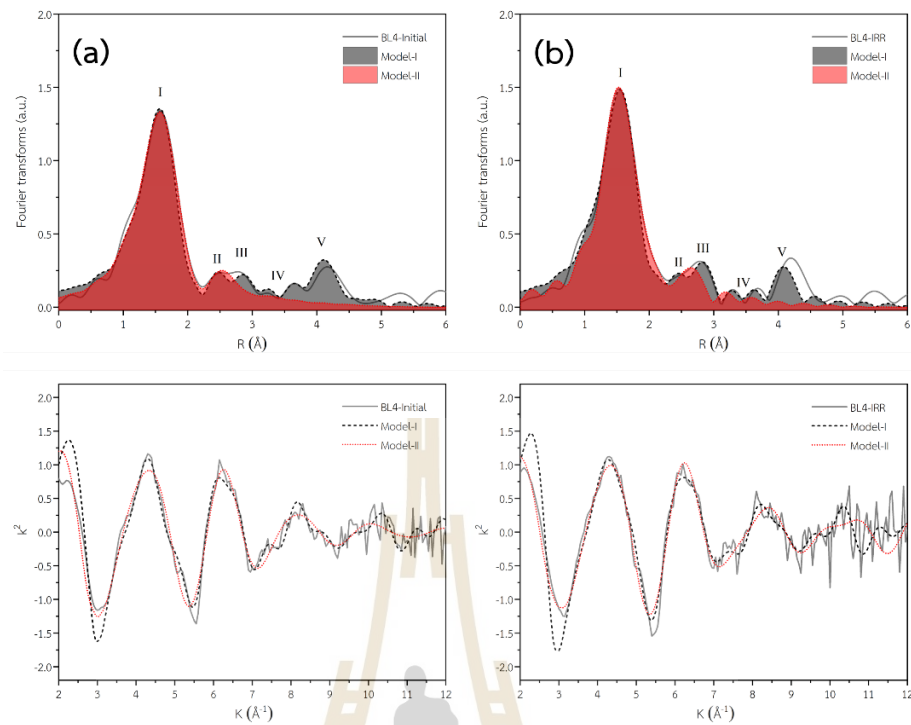


Figure A.4 Models I and II's IFEFFIT calculations are compared to experiment spectra of BL4-Initial (a) and BL4-IRR (b).

Table A.4 Model-I and Model-II were used to fit the first scattering path of neighboring atoms nearest to Fe ions in the BL4 sample.

Model	Path	BL4-Initial				R-factor	BL4-IRR				R-factor
		CN	σ^2 (\AA^2)	R (\AA)	SD		CN	σ^2 (\AA^2)	R (\AA)	SD	
I	Fe-O ₁	5	0.007	2.02	0.01		5.5	0.007	2.00	0.02	
	Fe-Be ₁	3	0.003	2.69	0.03	0.0215	3	0.003	2.70	0.04	0.0296
	Fe-Si ₁	6	0.016	3.39	0.04	E0 shift	6	0.013	3.38	0.04	E0 shift
	Fe-O ₂	6	0.007	3.81	0.05	4.9	6	0.004	3.77	0.04	3.3
	Fe-O ₃	12	0.014	4.05	0.04		12	0.014	4.01	0.05	
	Fe-O ₄	6	0.003	4.43	0.08		6	0.003	4.42	0.11	
	Fe-Si ₂	6	0.003	4.51	0.04		6	0.003	4.49	0.05	
	Fe-Al ₁	2	0.003	5.02	0.07		2	0.003	4.65	0.08	
II	Fe-O ₁	5	0.008	2.01	0.06	R-factor	5.5	0.002	1.98	0.07	R-factor
	Fe-Al ₁	2	0.015	2.37	0.34	0.0034	2	0.002	2.06	0.15	0.0109
	Fe-Si ₁	3	0.026	2.77	0.33	E0 shift	3	0.011	2.28	0.07	E0 shift
	Fe-O ₂	3	0.011	3.00	0.27	1.9	3	0.003	3.00	0.16	0.7

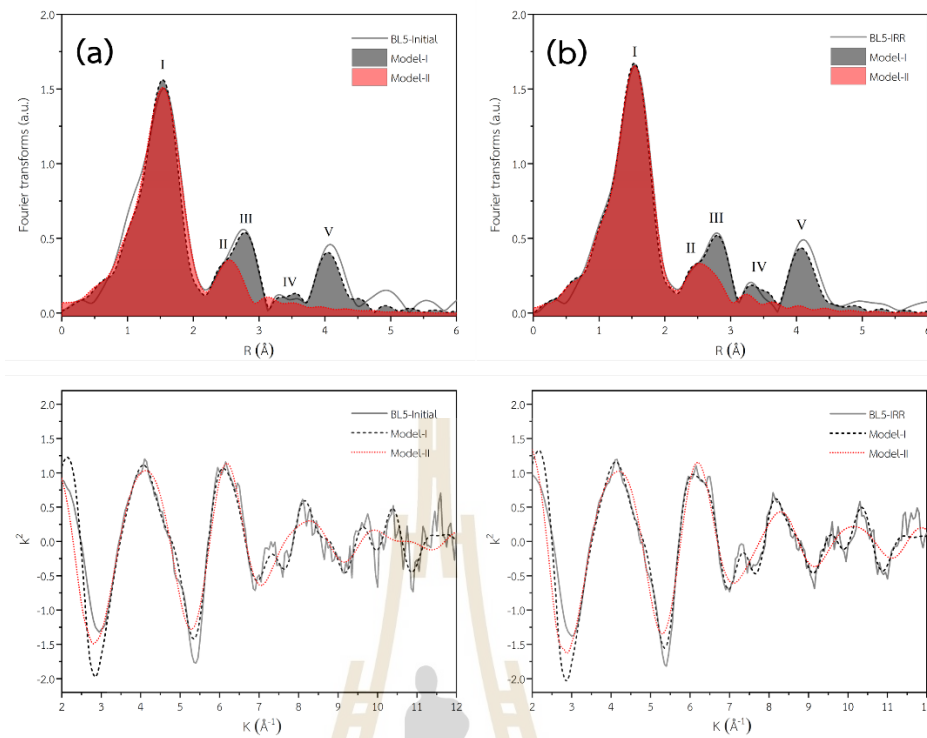


Figure A.5 Models I and II's IFEFFIT calculations are compared to experiment spectra of BL5-Initial (a) and BL5-IRR (b).

Table A.5 Model-I and Model-II were used to fit the first scattering path of neighboring atoms nearest to Fe ions in the BL5 sample.

Model	Path	BL5-Initial					BL5-IRR				
		CN	σ^2 (\AA^2)	R (\AA)	SD		CN	σ^2 (\AA^2)	R (\AA)	SD	
I	Fe-O ₁	6	0.007	2.01	0.01	R-factor	6	0.006	2.00	0.01	R-factor
	Fe-Be ₁	3	0.003	2.69	0.03	0.0291	3	0.003	2.69	0.03	0.0121
	Fe-Si ₁	6	0.007	3.34	0.02	E0 shift	6	0.008	3.34	0.01	E0 shift
	Fe-O ₂	6	0.003	3.70	0.03	-0.5	6	0.003	3.72	0.02	-0.1
	Fe-O ₃	12	0.013	3.95	0.04		12	0.019	3.97	0.04	
	Fe-O ₄	6	0.003	4.43	0.08		6	0.003	4.55	0.04	
	Fe-Si ₂	6	0.003	4.51	0.11		6	0.003	4.56	0.02	
	Fe-Al ₁	2	0.003	4.53	0.37		2	0.003	4.98	0.06	
II	Fe-O ₁	6	0.008	2.00	0.10	R-factor	6	0.006	2.00	0.04	R-factor
	Fe-Al ₁	2	0.012	2.38	0.42	0.0072	2	0.021	2.56	0.12	0.0015
	Fe-Si ₁	3	0.018	2.69	0.35	E0 shift	3	0.010	2.77	0.15	E0 shift
	Fe-O ₂	3	0.003	3.00	0.54	-3.0	3	0.003	3.06	0.03	0.0

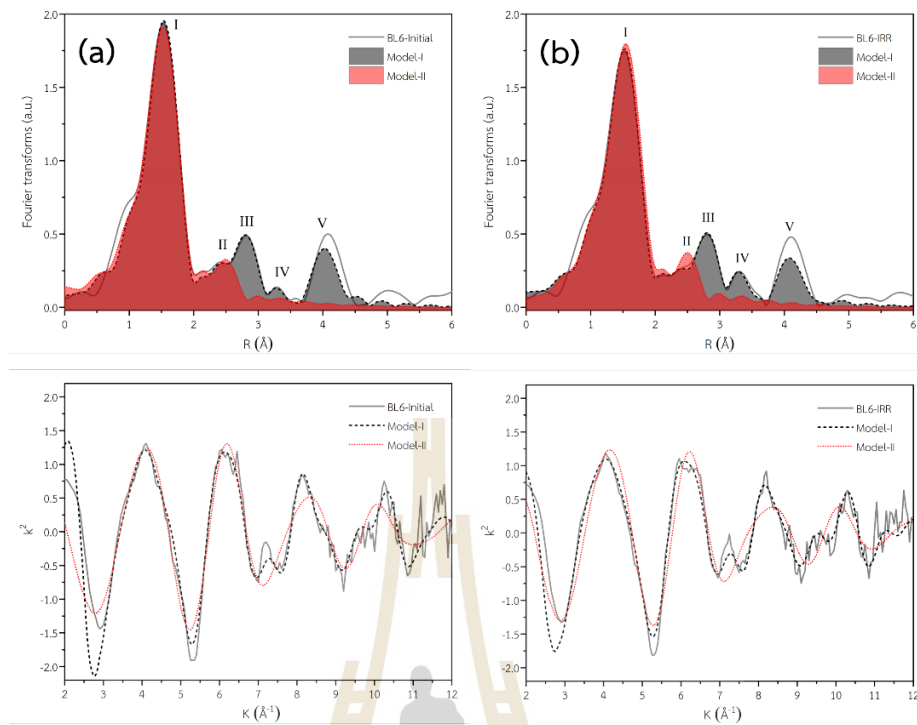


Figure A.6 Models I and II's IFEFFIT calculations are compared to experiment spectra of BL6-Initial (a) and BL6-IRR (b).

Table A.6 Model-I and Model-II were used to fit the first scattering path of neighboring atoms nearest to Fe ions in the BL6 sample.

Model	Path	BL6-Initial					BL6-IRR				
		CN	σ^2 (\AA^2)	R (\AA)	SD	R-factor	CN	σ^2 (\AA^2)	R (\AA)	SD	R-factor
I	Fe-O ₁	6	0.004	2.00	0.01	R-factor	6	0.005	1.99	0.01	R-factor
	Fe-Be ₁	3	0.003	2.69	0.03	0.0106	3	0.003	2.69	0.03	0.0102
	Fe-Si ₁	6	0.007	3.34	0.01	E0 shift	6	0.007	3.34	0.01	E0 shift
	Fe-O ₂	6	0.004	3.70	0.03	-2.2	6	0.003	3.74	0.02	-4.0
	Fe-O ₃	12	0.014	3.91	0.03		12	0.020	3.99	0.04	
	Fe-O ₄	6	0.003	4.50	0.17		6	0.003	4.40	0.04	
	Fe-Si ₂	6	0.003	4.53	0.19		6	0.003	4.49	0.02	
	Fe-Al ₁	2	0.003	4.54	0.37		2	0.003	4.97	0.05	
II	Fe-O ₁	6	0.005	1.97	0.09	R-factor	6	0.005	1.99	0.03	R-factor
	Fe-Al ₁	2	0.008	2.19	0.34	0.0068	2	0.019	2.54	0.12	0.0015
	Fe-Si ₁	3	0.013	2.33	0.2	E0 shift	3	0.011	2.76	0.15	E0 shift
	Fe-O ₂	3	0.003	2.93	0.32	-9.9	3	0.003	3.03	0.33	-4.4

CURRICURUM VITAE

Name Watcharakon Setwong
Date of Birth 20 May 1991
Place of Birth Buriram, Thailand

Education

- 2010 - 2013 : Bachelor of Engineering, school of Geotechnology,
 - Institute of Engineering, Suranaree University of Technology, Thailand
- 2014 - 2017 : Master of Engineering, school of Geotechnology,
 - Institute of Engineering, Suranaree University of Technology, Thailand
- 2018 - present : Doctor of Science, School of Chemistry,
 - Institute of Science, Suranaree University of Technology, Thailand

Publication

- Study of Fe ions in aquamarine and the effect of dichroism as seen using UV-Vis, NIR and X-ray. **Radiation Physics and Chemistry**, 109107., (2020)
- Using fly ash, palm oil fuel ash, and sugarcane bagasse ash as density and compressive strength additives for API class G cement. **Suranaree J. Sci. Technol.** Vol. 24 No., (2017)
- Study of using pozzolanic materials as additives for API class G cement. **SUTIR**, (2016)